Imaging biological water permeability barriers using CARS microscopy

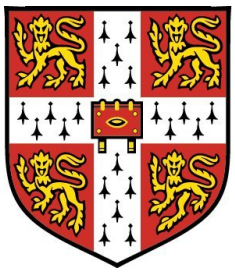

Keval Dipan Patel

Department of Engineering

Homerton College, University of Cambridge

Submitted for

Doctor of Philosophy

September 2018

This dissertation is the result of my own work and includes nothing which is the outcome of work done in collaboration except as specified in the text. This dissertation is not substantially the same as any that I have submitted, or, is being concurrently submitted for a degree or diploma or other qualification at the University of Cambridge or any other University or similar institution except as specified in the text. I further state that no substantial part of my dissertation has already been submitted, or, is being concurrently submitted for any such degree, diploma or other qualification at the University of Cambridge or any other University or similar institution except as specified in the text. This thesis contains 49,765 words and 56 figures.

I would like to dedicate this thesis to my loving parents who have always supported me throughout brightest and darkest times in my life, and have always encouraged my pursuit of my dreams.

Acknowledgements

I would like to thank Dr. Robert Balaban, for his mentorship, his support of my education, his confidence in my abilities, and for the amazing opportunities he provided me during my tenure in his laboratory.

I would also like to thank Dr. Bertrand Lucotte for his friendship, his guidance, and for all the conversations we shared during our time together at NIH.

I am grateful to Dr. Shery Huang for her mentorship and support during a critical period of my PhD, as well as the Biointerface group, especially Magda Gerigk who trained me in cell culture techniques and microfluidic device assembly and Duo Zhang, who provided me invaluable assistance.

I am also thankful to Bernhard Strauss who helped with imaging the microvessel microfluidic devices during my time in the Biointerface group.

I am very grateful to Professor Kim Dora and Xi Ye, who trained me in pressure myography and assisted me with the completion of critical experiments.

I would also like to thank the Dr. Mark Knepper's group (particularly Joe Chou and Lihe Chen) for their assistance in obtaining and characterizing the AQP1 knockout mouse model, and Dr. Zu Xi Yu and Daniela Malide for their help in performing immunohistochemical staining of sample generated from these mice.

Abstract

Alterations in the water permeability of the vasculature are attributed to several disease processes including atherosclerosis, reperfusion injury, diabetes mellitus, aging, chronic inflammation, and cancer. While vascular permeability has been extensively studied throughout the years, many of these studies have been limited by their invasiveness, specificity and spatial resolution. Coherent anti-Stokes Raman scattering (CARS) microscopy, offers a means to visualize the water permeability barrier of biological structures at high resolution within intact systems. In this thesis, water CARS imaging was characterized for determining water permeability in both dynamic and steady state conditions in model hydrogel systems. Computational models of water transport were used to validate the accuracy of water-CARS permeability mapping within these systems. This technique was then applied to the first CARS examination of water permeability in the cerebral artery and blood brain barrier. The vessels of mice deficient in the water channel protein aquaporin 1 (AQP1) were examined to evaluate the role of AQP1 in vascular water permeability.

A layered hydrogel imaging phantom was constructed from poly(ethylene glycol) diacrylate (PEGDA) to validate ability of water-CARS microscopy to determine the relative permeability differences of adjacent material layers. By imaging the dynamic and steady-state H_2O and D_2O exchange across the uniform and layered composite hydrogel structures, it was indeed possible to measure the relative permeability differences between individual material layers and to determine the location of material interfaces from analysis of the water-CARS image profile.

CARS imaging of intact biological samples poses many significant challenges. Microvessel microfluidic systems have the possibility to facilitate microscopy studies of vascular barrier function due to their flexibility of design, relative ease of preparation, and relative simplicity. In this thesis, the fabrication process of a human umbilical vein endothelial cell (HUVEC) microvessel microfluidic was investigated and optimized for future studies of vascular permeability and physiology. Several factors in the device assembly process were identified and optimized to improve the repeatability and reliability of the microvessel microfluidic fabrication protocol.

CARS imaging of the mouse cerebral artery water transport produced higher quality images than what had previously been achieved in the rat mesenteric artery, likely due to their reduced wall thickness. Permeability mapping of these arteries localized the water permeability barrier to the endothelial basolateral membrane, a result consistent with previous measurements performed in the rat mesenteric arteries.

Previous work by the Laboratory of Cardiac Energetics has suggested that the exclusively apical expression of the channel protein aquaporin 1 (AQP1) may account for the increase in observed permeability of the apical endothelial cell membrane. To test this hypothesis, water-CARS imaging of H_2O/D_2O exchange across cerebral arteries of wild type and AQP1 knockout (KO) mice was performed. No significant difference in the location of the water permeability barrier was observed. These findings indicate that AQP1 may not, in fact, be rate limiting for water transport across the apical endothelial membrane, and that it may play some other role in the physiology of the endothelial cell.

Contents

List of Figures

Chapter 1

Introduction

Increases in vascular water permeability has been associated with many disease processes including atherosclerosis, diabetes, acute shock, and aging [11]. Stroke is a debilitating condition that kills almost 130,000 Americans each year, and is the fifth leading cause of death in the United States [12]. An even larger number of people survive the initial period after a stroke but face neurological impairment including paralysis, aphasia, and dementia [12]. Ischemic stroke, occurs when the arterial blood supply that brings oxygen to a region of brain tissue is reduced to the point where the tissue is damaged or dies. In hemorrhagic stroke, bleeding occurs in the brain due to ruptures in a vessel and this can cause swelling and pressure that damages the tissue. Unfortunately, the damage associated with stroke may spread further than the initial vascular insult due to swelling that can occur in the damaged tissue. Several studies have indicated that alterations in the water permeability of the brain microvasculature may play a role in the this swelling [13, 14, 15, 16, 17, 18, 19, 20, 21, 22, 23, 24]. Tissue swelling can cause significant trauma by compressing nearby healthy tissues [25]. There are few interventions currently available to treat cerebral oedema directly. Current interventions include using osmotic agents and diuretics to remove water from the cranial vault, hyperventilation to reduce cerebral perfusion (and reduce brain volume), and partial craniectomy (partial removal of the skull), to allow the brain to expand beyond the confines of the skull temporarily until the swelling subsides.

This work aims to develop techniques to investigate the transport of water through biological structures including the vascular water permeability barrier.

Specifically, this work aims to develop optical imaging techniques to observe the transport of water across biological structures. In chapter 2, the topics of biological barriers and their permeability are explored, as well as experimental means to measure water permeability in biological materials. In chapter 3, the application of H_2O-CARS imaging as a means to measure the relative water permeability coefficients of layers within composite structures is validated. A microfluidic device was developed to perform this evaluation, accounting for the optical limitations of the microscope used and mechanics and permeabilities of the device materials. The microfluidic device was modeled to perform parametric fits between experimentally observed concentration profiles and model predictions. In chapter 4, methods to refine the *in vitro* fabrication of microvessels to study the development and function of the microvascular endothelium are described. In chapter 5, H_2O-CARS imaging was performed on *ex vivo* preparations of live arteries under H_2O/D_2O perfusion to determine the role of the water channel protein AQP1 in determining the location of the vascular water permeability barrier within the arterial wall. Finally, in chapter 6, the findings described in the previous chapters are summarized and directions for future research are described.

Chapter 2

Background

2.1 Biological barriers

Barriers preventing the free transport of substances are an essential characteristic of all biological systems. Without effective barriers life cannot maintain an internal environment, a key property associated with living things. The most fundamental barrier in biology is the plasma membrane, which is necessary to the cell's ability to regulate entry and exit of metabolic compounds, wastes, toxins, and signaling molecules among other things. The cell membrane gave organisms the beakers and flasks necessary to perform the chemistry of life. As organisms evolved over time, cells developed more sophisticated uses for this barrier such as the action potential, cellular respiration, and photosynthesis as shown in Figure 2.1.

As multicellular organisms arose, so did the importance of developing special barriers between different tissues and organs. Barriers became more complex: The skin of animals protects them from infections, water loss, mechanical trauma, changes in temperature, etc. The epithelium of the gut absorbs nutrients from food, fosters a beneficial environment for the gut microbiome while also excluding these organisms from the body, and removes water to form stool. The kidney utilizes a complex and variable permeability barrier system to filter blood and regulate the water balance of animals. In the development of most mammals, the placenta acts as an interface and barrier between the circulations of the mother and fetus (Figure 2.1).

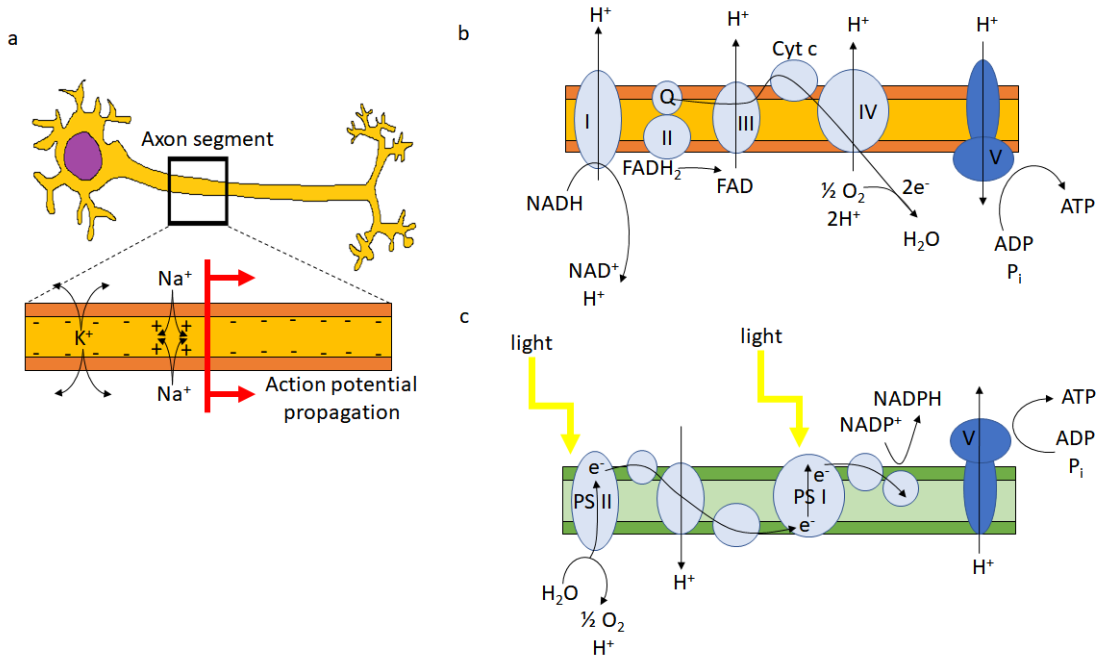

Figure 2.1: Cellular barriers have many important applications to vital cell functions. Cell membranes play a key role in the (a) generation and propagation of action potentials, (b) photosynthesis, and (c) cellular respiration which requires cellular compartmentalization via plasma membranes for the generation of electrical and chemical gradients necessary for the production of ATP.

2.2 The vasculature

The vascular system is composed of blood vessels of varying function and morphology and acts to deliver blood to the many tissues in the body while also separating blood contents from surrounding tissues. The barrier properties of the vasculature are involved in many important physiological and pathophysiological processes. The vasculature is essential to the transport of nutrients, waste products, water, oxygen, and carbon dioxide (as well as many other substances) to and from the tissues of the body. The exchange of the these substances between the blood and surrounding tissues is regulated by the permeability of the blood vessels.

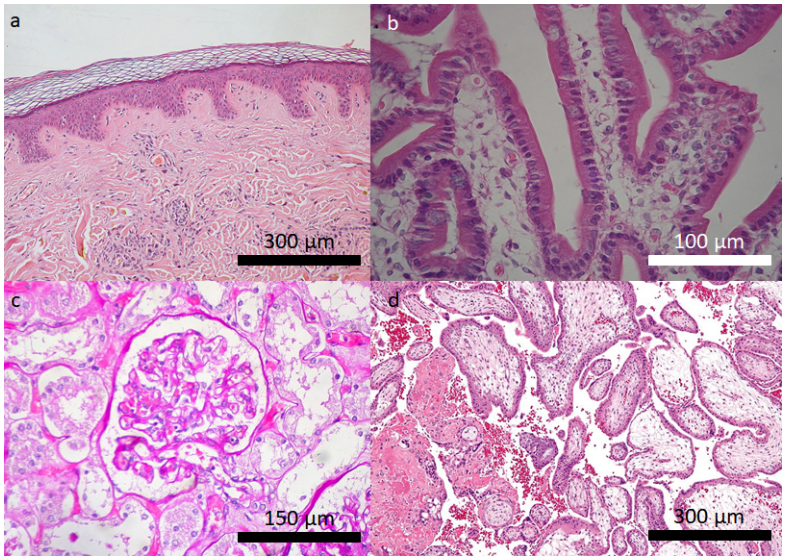

Figure 2.2: Tissue barrier applications [1, 2, 3, 4]. (a) Human epidermis is composed of specialized layers of the cells that act to protect the internal tissues from the external environment. b) Human intestinal epithelium contain epithelial cells capable of absorbing nutrients and water from the gut lumen, while shielding the body from digestive enzymes, bacteria, and variable pH conditions. c) Human renal tubular epithelium differentially excrete and reabsorb wastes and micronutrients from the glomerular filtrate to form urine and maintain water balance. (d) The placenta facilitates the exchange of nutrients and waste products between the maternal circulation and fetal circulation while preventing the blood from both individuals from coming into contact.

2.2.1 Vascular anatomy

The vascular system is a complex fluid transport system that most importantly acts to ensure the oxygenation of the tissues. However the vasculature is also very important in the transport of nutrients, lipids, immune cells, and water as well as in the distribution of signalling molecules such as hormones and the excretion of soluble wastes. The vascular system is a network of blood vessels that distribute oxygenated blood, rich in nutrients, pumped from the heart to the peripheral tissues, and then return the deoxygenated blood containing metabolic wastes back to the heart.

2.2.2 Blood vessel types

Blood vessels are categorized based on the direction of blood flow and their size and function [26, 27]. The arterial system contains vessels (arteries, arterioles) that transport blood away from the heart, while the venous system (veins, venules) contain vessels that return blood flow to the heart. The capillaries lie in between the arterial and venous systems and are the major exchange surface between the blood and the tissues. Arteries are conduits for high pressure blood from the heart to the arterioles. Arterioles lie between the arteries and capillaries and are the major point of hydraulic resistance in the vascular system. The arterioles regulate the amount of blood flow that enters the downstream capillaries and act to significantly lower the blood flow downstream. The capillaries are the site of nutrient, gas, and fluid exchange which is facilitated by the high surface area and thin wall thickness of the capillary network. The venules drain the capillaries to the veins, which return blood back to the heart (Figure 2.3) [28].

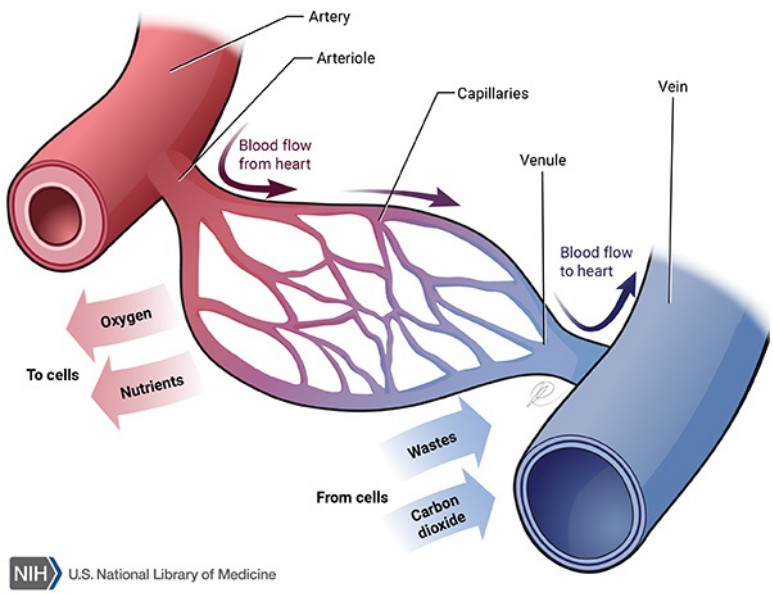

Figure 2.3: Schematic of the vascular system [5]. Arteries distribute blood from the heart to the arterioles. Arterioles act to regulate the flow of blood to the downstream capillary network. The capillaries are then drained by the venules which then drain to the veins. The veins return the blood back to the heart.

2.2.3 Blood vessel structures

Blood vessels are composed of concentric layers of tissue that are each specialized for separate functions [29]. The arteries, arterioles, veins, and venules possess three tissue layers: the tunica intima, the tunica media, and the tunica adventitia. The outermost layer, the tunica adventitia, is composed of connective tissue (primarily collagen I), and is the largest tissue layer in the veins and venules. This layer can contain nerves and the vasa vasorum (small capillaries) that supply larger blood vessels with oxygen and nutrients. The tunica media, or middle layer, contains smooth muscle cells and circularly arranged layers of elastin fibers. Smooth muscle can act to regulate vascular tone (vessel diameter), and this function is particularly important in the arteries and arterioles, whose tunica media is large and rich in vascular smooth cells. The elastin fibers provide elasticity to the blood vessels. The innermost layer, the tunica intima, consists of a single layer of highly specialized cells called the endothelium. The endothelium is in direct contact with the blood and forms the barrier between the blood and the periphery. Endothelial cells have many functions including regulating the transport of large and small molecules, regulating the permeability of the blood vessel during periods of inflammation, and modulating thrombus formation [30]. The endothelial cells are attached to the tunica media via a specialized connective tissue layer called the basement membrane. The basement membrane is composed of polysaccharide intercellular matrix components as well as connective tissue elements including collagen and elastin. Figure 2.4 shows an illustration of these tissues layers within an artery [5]. Capillaries are much simpler structures and consist of a single layer of endothelium surrounded by a very thin layer of connective tissue to facilitate the diffusion and transport of substances across the tissue/vessel interface.

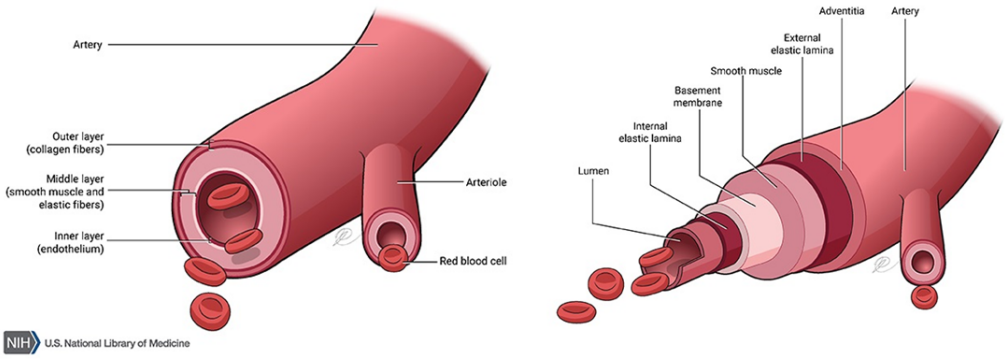

Figure 2.4: Layers of the arterial wall [5]. Arteries are lined by the endothelium (tunica intima), which is in turn surrounded by a layer of smooth muscle cells (tunica media). The artery is bound by a loose collagen layer (tunica adventitia).

2.2.4 Vascular endothelium

The endothelium refers to a cell monolayer that forms the lining for all blood vessels (as well as lymphatic vessels) [30]. Endothelium lines all internal surfaces of the vasculature and is composed of endothelial cells. Endothelial cells are flat and fusiform in shape and align their longitudinal axis along the direction of blood flow and contain nuclei that bulge into the lumen. Endothelial cells are highly specialized, and have varying roles depending on their location in the vascular tree or the organ where they are located. Generally, however, the endothelium is important in many fundamental physiologic processes including modulating the process of blood clotting, inflammation, angiogenesis, vasomotor responses, and the transport of substances across the vascular wall. The endothelium is the principal barrier of the vascular system and is critical to the separation of blood contents in the vessel lumen from the surrounding tissue. The endothelium functions as a partially selective barrier that regulates the permeation of blood cells, chemicals, and fluid (water) out of the blood vessels. Changes in endothelial permeability are involved in many disease processes. Dysfunction of the endothelium in conditions such as diabetes, atherosclerosis, chronic inflammation and cancer can lead to the increase in vascular permeability that can further disease progression [31].

2.2.5 Endothelial permeability

The selective permeability of a blood vessel is dependent upon both the size and chemical composition of the permeant of interest. Typically the blood vessels tolerate a small leak of water and small molecules (under 40 kDa) under physiologic conditions [31]. Large molecules require modulation of the endothelial barrier to permit leaking outside the vessel lumen. In the body, the most permeable vessels are the capillaries and post-capillary venules. Under conditions of inflammation, the endothelium of the post-capillary venules can be modulated to increase vascular permeability [32, 33]. The permeability and selectivity of the vascular barrier can vary in vessels from different organs. For example, the vessels of the central nervous system (CNS) are particularly impermeable to the leak of foreign substances and more tightly regulate the passage of material from the blood to the CNS tissue [34].

Substances can pass through the endothelium via multiple possible pathways. Under physiologic conditions, small molecules capable of passing through the cell membrane (water, gases, ions) can leak across the endothelium via a transcellular pathway. For larger molecules unable to passively cross the cell membrane, transcellular transport can be facilitated via membrane transporters, vesicles or caveolae. Typically, tight junctions and adherens junctions prevent the passage of substances along the paracellular pathway. However, these connections can be opened and closed under certain conditions such as inflammation, allowing increased leak along this pathway (Figure 2.5).

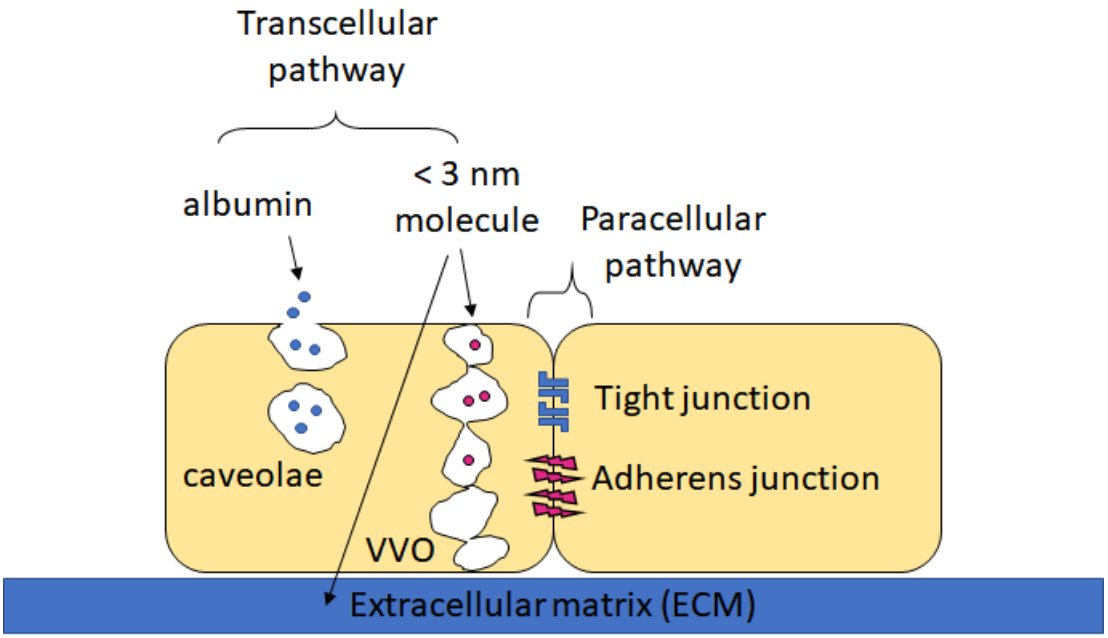

Figure 2.5: Illustration of various transendothelial transport pathways. The transport of substances from within the blood vessel lumen can exit the blood vessel through transcellular pathways or paracellular pathways. The small, membrane permeable molecules can directly pass through the endothelium, while larger molecules can be shuttled across via vesicular vacuolar organelles (VVO) and caveloae. Tight junctions and adherens junctions can be opened to permit the passage of substances via the paracellular pathway.

2.2.6 The blood brain barrier

As previously mentioned, the endothelium of the CNS is particularly impermeable. In the late 19th century Ehrlich demonstrated the presence of a barrier between the systemic circulation and the brain [34]. He injected Evan's blue dye into the vein of rats and discovered that the dye stained every organ of the body excluding the central nervous system [34]. His graduate student, Goldmann, then performed a complementary experiment by injecting the dye into the cerebrospinal fluid (CSF). In this case, the dye stained only the central nervous system but not other tissues. From these two experiments, it could be inferred that there was a barrier between the blood and the brain, but no barrier between

the CSF and the brain.

The selective barrier that separates the central nervous system (CNS) from the blood, the blood brain barrier (BBB), is formed by the endothelial cells of the cerebral circulation [34]. It is believed that the apical tight junctions of the endothelial cells form a permeability barrier preventing the passive transport of substances between the cells [15, 16, 35]. Material leaving the blood vessel therefore must pass through the endothelial cells of the BBB to enter the brain tissue. Endothelial cells of the BBB are equipped with several passive and active transporters that selectively transfer substances between the brain parenchyma and the vessel lumen [34]. The BBB is a formidable barrier to pharmacological interventions in the brain (such as chemotherapy) as it prevents many small molecules from entering the brain tissue, limiting the effectiveness of chemotherapy in the central nervous system.

The structure of the blood brain barrier varies as a function of its location. At the capillary level, the blood brain barrier consists of endothelial cells bounding the lumen of the capillary surrounded by astrocyte foot processes and neurons. It is currently believed that these cells do not physically perform the barrier role, but rather play a critical part in the differentiation and specialization of the BBB endothelium. In larger vessels of the brain, including arteries and veins, the endothelial layers are surrounded by smooth muscle and nerve cells. While the structure is different, the BBB is still functionally present in these vessels as well [34]. Figure 2.6 illustrates the structural differences between the BBB at different locations in the brain circulatory network.

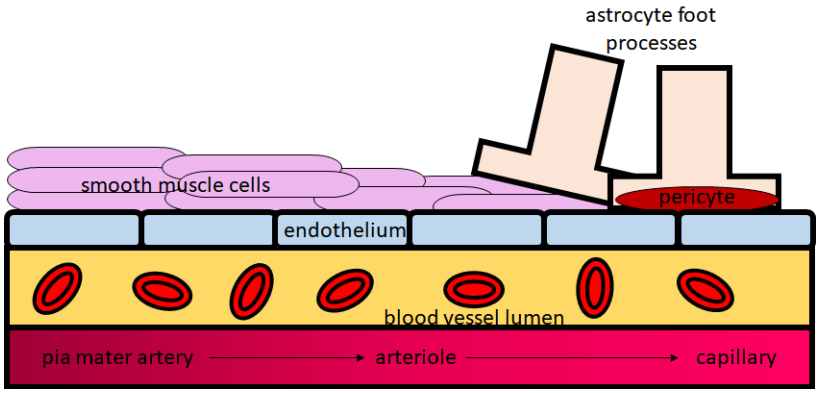

Figure 2.6: The blood brain barrier (BBB) at various positions in the cerebral circulation. At the arterial level, the (BBB) consists of endothelial cells surrounded by smooth muscles. As one moves further down the vascular tree, the smooth muscle diminishes and is replaced by astrocyte foot processes and pericytes.

2.3 Biological water permeability

Water is the solvent that makes life possible. Life most likely originated in water and water is the most abundant substance in living organisms (concentration of 55 M!). All life makes use of water as a medium to perform biochemical reactions, transport nutrients and wastes and to transmit signals within and between cells. The polar nature and the capacity for water to form hydrogen bonds is critical for processes like biological protein folding, and is important to the formation and stability of the phospholipid bilayer structure that is the basis of cell membranes. The importance of water to living systems highlights why cells have developed critical mechanisms to facilitate water transport, uptake, and secretion. The lipid composition of cell membranes may lead one to suspect that the plasmalemma is highly impermeable to water, a polar molecule [36]. This is not, however, observed in physiology. Cells can quickly equilibrate their water content when exposed to environments of different osmolality [36]. Peter Agre's Nobel Prize winning discovery of water specific channels in the membranes of red blood cells provided the molecular basis for this observed permeability. The existence of aquaporins demonstrates the importance of water specific transport in living systems.

2.3.1 Clinical considerations

Water transport is of importance in many areas in clinical medicine. The most obvious application is the role of selective water transport in the renal system to regulate total body water and osmolality. Vascular water permeability also plays an important role in progression of many disease states including inflammation, diabetes mellitus, ischemia/reperfusion injury, multiple sclerosis and epilepsy [37].

Diabetes is a metabolic disorder in which the body fails to regulate the amount of sugar in the blood. The morbidity and mortality in persons with diabetes is mainly attributed to end organ damage resultant from microvascular disease [37]. The prolonged increase in blood glucose levels increases the formation of advanced glycation end products (AGEs) in the vascular tissues. AGEs can increase the crosslinking of ECM proteins like collagen, increasing the stiffness of blood vessels. AGEs can also react with components of the endothelial glycocalyx, increasing vascular permeability [37]. Additionally, AGEs can induce vascular inflammatory signalling pathways by binding to receptors for advanced glycation end products (RAGEs) expressed in the endothelium, which can further increase the permeability of the microvasculature [38].

Reperfusion injury occurs when blood flow is restored to tissues that have been damaged due to lack of blood flow (ischemia). Upon restoration of oxygenated blood, damaged cells increase production of reactive oxygen species (ROS) due to dysfunctional cellular respiration. ROS production can damage endothelial cells leading to the activation of pathways that increase vascular permeability [37]. Reperfusion injury often occurs after the treatment of myocardial infarction (heart attack) by stent placement or coronary bypass, and recovery following cerebral infarction (stroke). In the case of stroke, the resultant increase in cerebral vascular permeability can cause oedema, a potentially dangerous condition.

Oedema, the swelling and retention of fluid in the extracellular space of tissues, occurs due to the modulation of vascular water permeability. When tissue is exposed to trauma, infection, or the systemic allergic response, the water permeability of the vessels increases and water leaves the vascular compartment to enter the extracellular compartment [39]. This increase in vascular permeability

has many clinically important consequences. It allows cells of the immune system to access the site of injury or infection, but it also causes the tissue to swell and retain water. In areas of the body where space is limited, such swelling can result in damage to otherwise unaffected tissue such as in compartment syndrome and cerebral oedema [40, 31]. Cerebral oedema is the accumulation of excess fluid in the extravascular spaces of the brain (intracellular and extracellular). This fluid accumulation causes the brain tissue to swell and expand against surrounding structures such as the cerebrospinal fluid (CSF) compartments (ventricles and cisterna) and healthy brain tissues. Cerebral oedema can be caused by trauma to the brain, ischemic stroke, inflammation due to infection (meningitis and encephalitis) or cancer. In ischemic stroke, oedema can contribute significantly to the morbidity and mortality in addition to the original infarct. During vasogenic cerebral oedema, it is believed that the water permeability of the BBB increases, allowing blood to leave the cerebral capillaries into the extracellular space [34, 17]. The mechanism of this change is not fully understood, and has not been observed directly *in vivo*.

2.3.2 Water transport across cells

Under physiologic conditions, the cell membrane is the greatest barrier to water transport across a cell. Water transport across the cell membrane can occur via the process of diffusion and osmosis. Diffusion is the result of the random motion of particles and is a function of temperature [41, 42].Water diffusion across the cell membrane can either occur through pores in the membrane, or through the lipid membrane itself. In order for water to diffuse through the lipid membrane, it must dissolve (partition) into the membrane [43]. The composition of the lipid membrane can affect water permeability by affecting the partitioning of water within the membrane. Lipid bilayers are fluid and have increased water permeability. Cholesterol reduces lipid bilayer fluidity and therefore decreases membrane water permeability [41]. Osmosis is the net flux of water across a cell membrane due to the differences in concentrations of impermeable solutes. During osmosis, water can either diffuse through lipid membrane, driven by the

difference in chemical potential, or flow through a pore, driven by the hydrostatic pressure gradient within the pore [43].

Water transport across the lipid bilayer (via solubility-diffusion) can support relatively large water fluxes across the cell membrane, and while water transport across the plasma membrane is possible, some cells contain specialized water transport proteins to further increase the membrane permeability to water. Aquaporins are a family of transmembrane proteins that acts as high selectivity water pores [41]. Membranes that have aquaporins (pores) possess higher osmotic permeability than diffusive permeability. In the case of single file transport (which occurs in the aquaporin channels), concerted motion of water due to hydrostatic pressure is more readily achieved than via diffusive transport [43]. Alterations in the expression of aquaporin can lead to large changes in the water permeability of the cell membrane (for example in the renal collecting duct). Aquaporin channels are expressed on the vascular endothelium [11], and it has been hypothesized that these channels may increase the water permeability of the endothelial cells.

Aquaporin 1 (AQP1), the first aquaporin protein discovered, is expressed in the endothelial cell membrane as a tetramer, with each monomer containing a single pore [41]. The AQP1 monomer is 28 kDa and contains 6 transmembrane domains (Figure 2.7). Two loops containing an important sequence of amino acids, Asn-Pro-Ala (NPA), align themselves along the transmembrane domains to form an electrostatic barrier within the pore. The AQP1 pore is 2.8 Å in diameter (a water molecule is 2.75 Å in diameter) at its narrowest point. The NPA motifs are important to the selectivity of the AQP1 protein and, in fact, are conserved in other members of the aquaporin family of proteins. They create a dipole within the water channel preventing the passage of small ions such as protons. Due to the channel narrowness and the ion excluding action of the NPA motifs, aquaporin proteins are highly selective water pores.

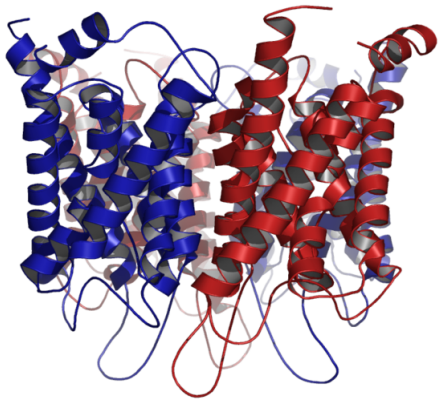

Figure 2.7: Ribbon schematic of the AQP1 protein tetramer (composed of four monomers) [6]. At the center of each monomer is a channel pore. A peptide loop within the pore contains an NPA motif that acts to exclude the transport of small ions across the channel.

2.4 Measuring vascular water permeability

The water permeability of the vasculature has been studied with many different techniques, each with their own advantages and disadvantages. The water permeability of a material sample can be described using different, but related values including: the filtration coefficient (K_f), the hydraulic conductivity (L_p), and the effective diffusion coefficient (D_{H_2O}) [37]. Measuring water transport properties is an inherently invasive process and this can pose a challenge to obtaining accurate measurements from intact biological systems.

2.4.1 Fluid filtration

The fluid filtration coefficient (K_f) determines the net filtration of fluid (J_v) across a vessel wall given the hydrostatic (ΔP) and osmotic ($\Delta\Pi$) driving forces (Equation 2.1). The fluid filtration coefficient accounts for the complex physical factors that determine the fluid resistance of the vessel wall [37]. The hydraulic conductivity (L_p) is simply the filtration coefficient normalized to the surface area

(A) as shown by Equation 2.2.

$$J_v = K_f(\Delta P - \Delta \Pi) \tag{2.1}$$

$$L_p = \frac{K_f}{A} \tag{2.2}$$

The measurement of the fluid filtration coefficient is relatively simple. Osmotically balanced fluid (representative of physiological conditions) is perfused at fixed pressure through either intact tissues [44, 45] or isolated vessels [46, 47, 48]. In the case of intact tissue (such as animal hind limbs), the fluid flux across the aggregate vasculature was determined by the increase in weight of the tissue sample. In the case of isolated vessels, the volume of fluid leak of the artery can be directly measured. The hydraulic conductivity of isolated vessels can additionally be measured by normalizing the filtration coefficient with the vessel surface area.

While the filtration coefficient and hydraulic conductivity provide direct measurement of water transport within tissue samples, these measurements are crude and oversimplify the physical processes that determine vascular permeability. The vascular wall is a complex and multilayered structure and these generalized measurements cannot provide insight into the role of each wall component with mechanical or biological disruption of the vessel wall [48, 46].

2.4.2 Diffusion magnetic resonance imaging

Diffusion MRI can map the effective water diffusion coefficient (D_{H_2O}) of biological tissues using strong magnetic field, magnetic field gradients, and radio waves. Diffusion MRI has significant advantages as it can be performed on living subjects (it is regularly used in hospitals), and because it does not require the introduction of contrast agents. The effective water diffusion coefficient estimated by diffusion MRI accounts for the restricted motion of water due to differences in tissue porosity, tortuosity, and extracellular/intracellular water content. This imaging method is particularly effective at detecting the acute phase of a stroke. After a stroke, injured brain cells internalize extracellular water (cytotoxic oedema), restricting the free motion of water in that region to 20-30% [49]. Diffusion MRI can detect these regions of restricted water transport, and has become an important tool in the management of acute stroke patients [49].

While diffusion MRI is limited by the imaging resolution of ∼1 mm and can be used to map the change in water permeability in large volumes of tissues, the structures of the vascular barrier are too small to be visualized with this technique.

2.4.3 Optical imaging modalities

Optical imaging techniques offer greater resolution (< 1 μm) and economy compared to MRI. At this resolution, it is possible to visualize the cellular components of the vascular barrier. However, unlike MRI, optical imaging requires the addition of contrast to visualize the motion of water. Two optical imaging methods used to image water transport take advantage of the chemical similarity between water (H_2O) and deuterated, or heavy, water (D_2O): Coherent anti-Stokes Raman spectroscopy (CARS) and D_2O sensitive fluorescence imaging. Deuterated water (heavy water) is comprised of water molecules containing two deuterium atoms bound to oxygen. Deuterium is a hydrogen atom that contains a proton and neutron in its nucleus. Heavy water molecules have slightly stronger hydrogen bonds and therefore its melting and boiling temperatures are higher than those of regular water. Furthermore the "neutral" pH of heavy water is 7.43. It is approximated that water and D_2O interact with biological systems similarly (though not always the case) and therefore D_2O can effectively act as a contrast agent for water. The chemical differences between regular and heavy water is a potential disadvantage to using D_2O as a contrast agents.

2.4.3.1 CARS Imaging

CARS is a dye-free imaging method that is capable of imaging biological structures "by displaying the characteristic intrinsic vibrational contrast" of the structure's molecules [50, 51]. CARS imaging makes use of the vibration of molecular bonds and no external markers are necessary to generate an image. In traditional Raman spectroscopy, the characteristic frequency of a molecular bond is oscillated using a single optical wave. Instead of a single wave, CARS employs three beams (making it a third-order nonlinear process): the pump beam at frequency, ω_p, the probe beam at frequency, ω_{pr}, and the Stokes beam at frequency, ω_s. CARS

uses the difference in frequencies between the pump and Stokes beams ($\omega_p - \omega_s$) to drive the oscillations of the molecular bond of interest. When the frequency difference approaches the resonance frequency of the bond, the bond is oscillated efficiently. The bond oscillations represent the oscillations of the electron cloud that comprises the bond. The electron oscillations result in the periodic alternations of the refractive index of the sample material. The oscillating change in the refractive index of the material is probed by the probe beam. Some photons of the probe beam will get excited to a higher frequency ($\omega_{pr} + \omega_p - \omega_s$). This emitted light is called the anti-Stokes emission.

The process of CARS takes place in the following sequence [50]: First, the sample is illuminated with intense light via the pump beam to excite the molecules in the sample to their various virtual states from their ground state. Second, the stimulated molecules are further excited by a lesser energy beam, the Stokes beam, to stimulate the depopulation of the excited virtual state molecules to the vibrationally excited state of the molecule. The vibrationally excited state is very specific to the chemical properties of the molecule. Because the frequency difference ($\omega_p - \omega_s$) can be tuned, the desired population of molecules can be specifically converted into a vibrational state. Third, in order to visualize the desired population of molecules, a probe beam is used to elevate the molecules to a higher virtual state. Finally, the excited molecules will relax to their ground state releasing higher energy photons than the probe beam ($\omega_{pr} + \omega_p - \omega_s$), called the anti-Stokes emission (ω_{CARS}). These steps are illustrated by Figure 2.8.

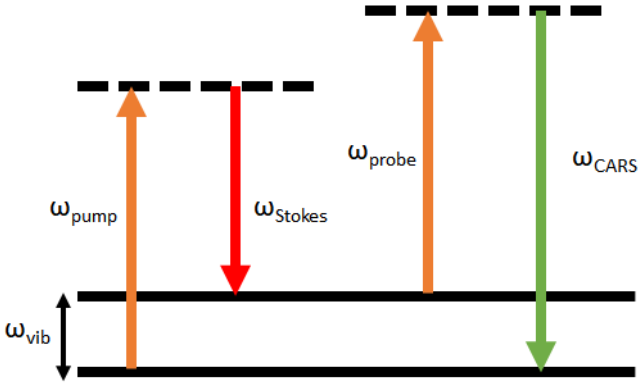

Figure 2.8: CARS energy diagram. Illustration of excitation of sample molecules by the pump, Stokes, and probe beams to generate the anti-Stokes emission.

Different molecules have different characteristic vibrational energy states [50]. Because the D_2O and H_2O Raman signals are distinguishable [52], one can use D_2O as a contrast agent for water. Previous work has shown that the kinetics of water transport within cells [53] across the wall of cultured cysts can be measured by immersing D_2O filled cysts in H_2O [51]. The Laboratory of Cardiac Energetics has collected steady state concentration data by perfusing rat mesenteric arteries with D_2O in a H_2O bath [11]. CARS imaging is elegant as it directly measures the water concentration, which can be used to infer the relative resistance to water transport. Unfortunately, it is difficult to apply in biological environments: the three beams at two different wavelengths required for imaging are differentially scattered due to wavelength dependent scattering (chromatic aberration). This can drastically destroy the point spread function (PSF). This reduces the possible imaging depth and effective imaging resolution. Indirect water imaging methods may perhaps provide a simpler, more robust means to image the movement of water in biological structures.

2.4.3.2 D_2O Sensitive Fluorescent Imaging

Fluorescent imaging of water transport using D_2O sensitive dyes such as ANTS (8-Aminonaphthalene-1,3,6-Trisulfonic Acid) (Figure 2.9) is an alternative way to image D_2O that may make it possible to image deeper into tissues because

the excitation of ANTS only requires a one-photon phenomenon which is less prone to scattering and therefore capable of penetrating deeply into samples. The fluorescent dye ANTS experiences a 4-fold enhancement of fluorescence in the presence of D_2O instead of H_2O [54, 55, 56]. This enhancement is linear with respect to D_2O concentration. ANTS can be used with conventional fluorescence imaging methods such as confocal microscopy as well as two-photon microscopy which can allow greater imaging depths. Linear fluorescence imaging is less costly and less complicated than more sophisticated imaging methods such as CARS. One potential weakness with this imaging system is that ANTS may not distribute evenly between cellular structures, and this may reduce the resolution of the imaging technique [55]. It may be possible to chemically alter the dye to overcome this potential issue. Since the D_2O sensing ability of ANTS is due to fluorescence enhancement, signal attenuation at greater imaging depths may confound D_2O concentration measurements.

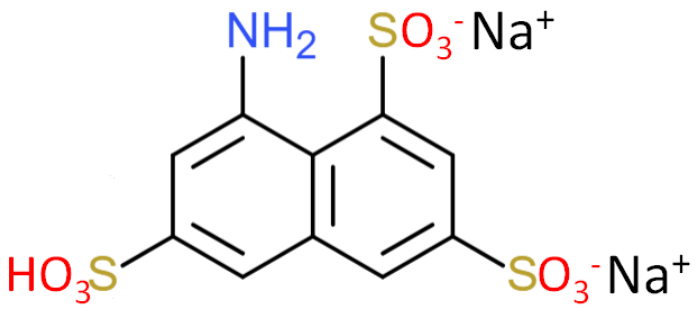

Figure 2.9: 8-Aminonaphthalene-1,3,6-trisulfonic acid (ANTS).

ANTS has been used in previous studies to assess the permeability of cellular membranes, liposomes and endosomes [54, 55, 57, 58]. ANTS has often been used in conjunction with a quenching agent in a way that dilution of the dye/quenching agent mixture results in increased fluorescence. Alternatively, vesicles, cells, or endosomes are loaded with D_2O and ANTS and then rapidly placed in an H_2O environment. During this time, the reduction in fluorescence is measured. While this dynamic measurement method is useful in estimating gross permeabilities

of structures, it is not useful in resolving the physical location of the barrier structure.

Chapter 3

Imaging water transport in hydrogels using CARS microscopy

3.1 Introduction

Until recently, prior water-CARS imaging experiments studying water permeability and transport in biological systems were performed by measuring the transient CARS signal intensity profile as D_2O and H_2O were exchanged across the material of interest [55, 59]. Transient experiments of this type are restricted by the time required for acquisition, resulting in reduced signal to noise ratio. Additionally, temporal experiments are challenging as it is difficult to apply a precise perturbation of the system (input function). For example, measuring the water permeability of cells by observing the diffusion of D_2O out of D_2O loaded cells requires a rapid and precise swapping of the extracellular solution from D_2O to H_2O. This can be challenging as the timescale of the switching of solutions and spatial scale of solution mixing are potentially similar to the timescale of fluid exchange in the cell and the cell size. Imprecision in the input function can lead to discrepancies in the overall measured permeability. Additionally, temporal experiments typically can only provide lumped permeability information for composite structures, because the overall rate of water transport is what is measured. Previous work by the Laboratory of Cardiac Energetics attempted to address this challenge by performing *steady-state* water transport observations across intact perfused rat mesenteric arteries [11]. In this experimental setup, the

water concentration profile was measured across the wall of rat mesenteric arteries to make inferences about the relative permeability of arterial wall structures. These experiments were limited by optical distortions induced by the sample and uncertainty about the resolution of the imaging PSF. Furthermore, it was not feasible to confirm the individual permeabilities of the endothelial apical and basolateral membrane to validate this measurement approach.

In order to validate water-CARS as a method to measure the relative material permeability coefficients of composite structures, a multi-layered hydrogel microfluidic device was fabricated and imaged under H_2O/D_2O perfusion. The effective water transport in the gels were measured using temporal transport studies to confirm the accuracy of the relative permeability experiments. The use of water-CARS to measure the water transport properties of hydrogels may have additional use in biomedical engineering. The diffusion of water is an important parameter in the design of soft contact lenses as they are fabricated from hydrogels [60]. Soft contact lenses, when worn, dry out over time due to evaporation. Water transport away from the corneal surface via diffusion can cause the cornea to desiccate or even adhere to the contact lens itself (potentially damaging the eye) [60]. Water-CARS imaging of water diffusion in these materials could aid in the characterizing of soft contact lens material properties and could potentially lead to better lens design.

3.2 Hydrogel selection

In order to create an imaging phantom to validate steady state water transport imaging, it was necessary to find a material whose water permeability could be reduced measurably from liquid water and whose water content would be high enough to produce sufficient signal for water-CARS. Hydrogels are composed of networks of cross linked hydrophilic polymer chains that are highly absorbent to water. Due to their high water content, hydrogels possess many mechanical properties similar to natural tissue and are often used for many biomedical applications including cell culture, tissue engineering, and drug delivery. The polymer networks in hydrogels can be linked via physical interactions (entanglements, crystallites) or chemically cross-linked (covalent bonds). These interactions are

what prevents the hydrophilic polymer network from dissolving during hydration. Hydrogels were considered a suitable material for this validation experiment because it was considered theoretically possible to tune the water permeability [8] of these materials and because of their high water content (to provide enough signal for water-CARS).

The effective diffusion of water, ions, and small molecules through a hydrogel is reduced by decreasing the mesh size of polymer chains within the hydrogel [8]. This reduces the average pore size of the hydrogel and increases the available space for interaction of water molecules within the hydrogel with the hydrophilic polymer network (primarily through hydrogen bonding). These interactions act to slow the diffusion of water across the hydrogel. Cross-link density can be increased by either increasing the density of polymer within the hydrogel or by increasing the amount of binding sites available at each monomer prior to cross-linking.

Due to their tunable cross-linking density, as well as anti-fouling properties, poly(ethylene glycol) (PEG) based hydrogels have been extensively studied for use in biomedical and tissue engineering applications. While there are many methods of synthesizing PEG hydrogels [61], acrylated and methacrylated PEG monomers are particularly useful because these monomers can be crosslinked via light curing. Photocrosslinkable hydrogels can be easily patterned into virtually any 2-dimensional shape by applying a photomask over the pre-polymer solution. The regions exposed to the light will undergo cross-linking while the protected areas of the solution will not react and can be removed. The patternability of the hydrogel material was an important factor in the material selection when developing the imaging phantom. In the ideal case, hydrogel slabs with differing material properties could be patterned adjacently to ensure sharp, distinct transitions in material properties. This would best replicate what we have previously observed in the artery (water rich regions adjacent to more impermeable lipid membranes). One of the most widely used and characterized photocrosslinkable hydrogel monomers is poly(ethylene glycol) diacrylate (PEGDA). PEGDA consists of a PEG molecule flanked by two reactive acrylate groups (Figure 3.1a). Typically, a photoinitiator compound is added to a solution of PEGDA prior to

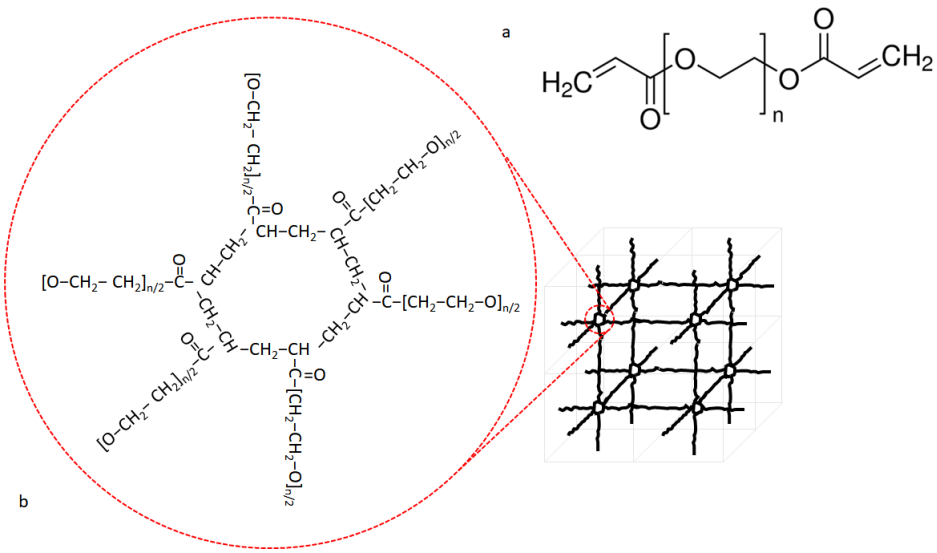

Figure 3.1: PEGDA monomers can be used to form PEG based hydrogels. (a) PEGDA is composed of a PEG molecule with acrylate groups bonded to each end. (b) PEGDA chain ends can come together to form high molecular weight chains like cyclododecane at cross-linking points to facilitate the generation of a 3-D network [7, 8].

curing. When the mixture is exposed to ultraviolet (UV) light, the photoinitiator generates free radicals that open the carbon-carbon double bonds and the reactive monomers can then combine forming large insoluble molecular networks via a chain-growth reaction (Figure 3.2a). Crosslinking points form as high-molecular weight chains that branch facilitating the formation of a 3D network (Figure 3.1b).

3.3 Design and manufacture of hydrogel microfluidic device

A multilayered hydrogel microfluidic device was fabricated as an imaging phantom to validate relative permeability measurements obtained using water-CARS microscopy. Several considerations were taken into account in developing a suitable water-CARS imaging phantom. In order to perform the experiment, the

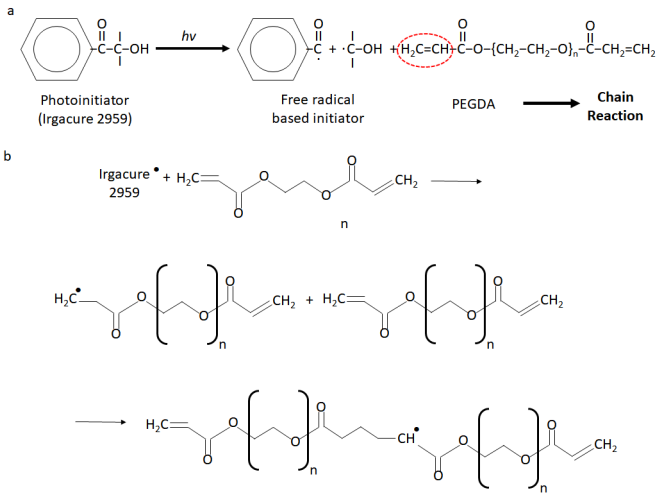

Figure 3.2: Photocrosslinking of PEGDA hydrogels is mediated by a photoinitiator and UV light. (a) Photoinitiator compounds facilitate the formation of free radicals upon exposure to UV light. The free radical opens the carbon-carbon double bonds in the acrylate groups [9] and (b) the reactive monomers combine to form an insoluble network through a chain reaction [10].

device required a means to establish an H_2O/D_2O gradient across the hydrogel barrier. This was achieved with two perfusion channels flanking opposite sides of the diffusion barrier. It was also necessary to pattern hydrogel regions of different water transport properties adjacent to each other between the perfusion channels. The device design was also limited to geometries that could be produced using a photomask.

3.3.1 Device design

The multi-layered hydrogel microfluidic device is supported by an enclosure made from a glass microscope slide, coverglass and 100µm spacer (Figure 3.6). A three-channel device was used for this work. Hydrogel pre-polymer solution was photocrosslinked using a photomask that created three separate channels. The central channel was then sequentially filled with a pre-polymer solution of a differing density and then photo cross-linked once more to form a layered gel slab (3 layers, 2 materials) between two channels. The photomask was designed using L-Edit

software (Tanner L-Edit, Mentor, Wilsonville, OR, USA) and the design was exported to a .gds file and printed by Fineline imaging (Colorado Springs, CO, USA) onto a transparency. Each of the device channels are 1 mm wide, 100 μm thick, and has a straight portion that is 30mm long. The channels are accessed via inlet and outlet ports in the glass slides. PDMS manifolds are bonded to the glass slides to provide a compliant attachment point for tubing.

3.3.2 Fabrication of device enclosure

First, inlet and outlet ports were drilled into the 25×75×1 mm glass slides (Fisher, Pittsburgh, PA, USA) using a 1.1 mm diamond tipped drill bit (CRL, Los Angeles, CA, USA). The glass slides were then cleaned with isopropanol to remove dust and blow-dried with filtered air. Next, tubing manifold blocks were made from polydimethylsiloxane (PDMS)(Sylgard 184, Corning, Midland, MI, USA). A 10:1 ratio of base to curing agent was mixed and degassed via a vacuum dessicator to remove most of the bubbles introduced during the mixing process. The mixture was then poured into 10 cm plastic petri dish to form a layer approximately 2-3 mm deep. The dishes were placed on a level surface and cured overnight. Rectangular slabs were cut from the PDMS layer to form the tubing manifold blocks. Dust and debris were removed from the PDMS blocks using adhesive tape (3M scotch tape, Maplewood, MN, USA). The PDMS manifolds were affixed to the glass slides via plasma bonding. The surfaces to be bonded were placed "face up" in an open plastic petri and then transferred to a plasma cleaner (Harrick Plasma, Ithaca, NY, USA) at power setting: high for 2 min under vacuum. The plasma bonding process creates free radicals on the surface of the PDMS blocks and glass. The device components were then removed from the plasma cleaner and the treated surfaces were carefully brought into contact. The free radicals on each surface react to form Si-O-Si bonds generating a very strong seal between the PDMS and glass surfaces.

Once the manifold blocks were attached to the glass slides, the glass slides and coverglasses were ready for silanization (dicussed in the subsequent section). The device coverglass and slide were cleaned with isopropanol, dried with nitrogen, and exposed to oxygen plasma for 30 seconds. The devices were then removed

from the plasma cleaner and immediately placed into a solution containing 1 mL of 3-(trimethoxysilyl)propyl methacrylate (Sigma, St. Louis, Missouri, United States), 200 mL of anhydrous ethanol, and 6 mL of 10% (v/v) aqueous acetic acid solution for 3 min. The glass components were then removed, rinsed with ethanol and dried in an oven at 80 ℃. A 100 μm thick adhesive tape spacer was attached to the opposite surface of the slide (PPT-36G/GRN172, J.V. Converting Company, Fairless Hills, PA, USA) to form a spacer. A rectangular piece was then cut from the tape spacer using a scapel to form a rectangular ring enclosure around the inlet and outlet ports. A 0.75 mm biopsy punch (Acuderm Inc., Ft. Lauderdale, FL, USA) was then used to create holes in the PDMS manifold blocks that were continuous with the holes drilled into the glass slides.

3.3.3 Cross-linking gel to glass surfaces

When PEGDA pre-polymer solution is cured against a glass surface, the resulting hydrogel adheres to the glass via physical interactions. When the gel is subsequently immersed in water, the gel may absorb additional water and swell slightly, causing the gel to shear against the glass surface and detach. In the microfluidic design described in this chapter, a tight seal between the hydrogel and surfaces of the glass slide and coverglass was necessary to prevent leaking of water between the channels. This was achieved through the process of silanization.

Acrylamide hydrogels, used for gel electrophoresis may shrink and swell unevenly due to the pH gradients developed during isoelectric focusing. To prevent this, the gels are attached to glass plates using acrylate silanes, which constrains the gel from deforming along the plane of the glass surface. Silanization involves coating the glass surface with alkoxysilane molecules. The alkoxysilanes can be formulated to contain functional groups that allow them to react with specific molecules of interest. For the PEGDA micrfluidic device, the alkoxysilane, 3-(trimethoxysilyl)propyl methacrylate (TMSPMA), which possesses a methacrylate group that can covalently bond PEGDA monomers/polymers upon initiation via free radicals (Figure 3.3), was used to chemically bond the PEGDA hydrogel to glass surfaces. Prior to PEGDA photocrosslinking, the glass surfaces of the device were coated with TMSPMA via a reaction between the hydroxyl groups on

the glass surface and the methoxysilyl groups in the silane that from a covalent -Si-O-Si- bond.

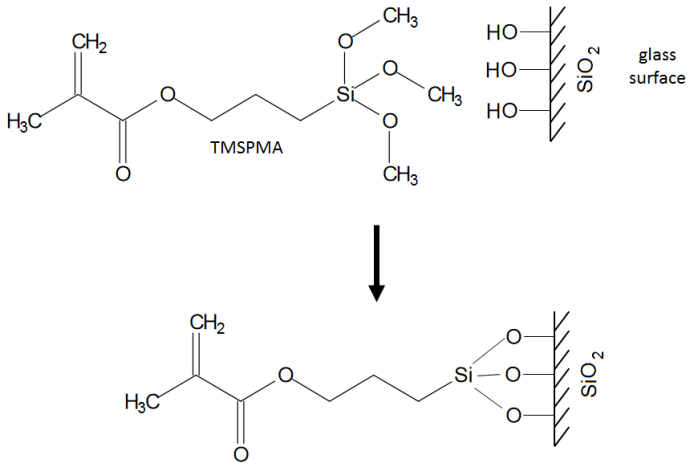

Figure 3.3: 3-(trimethoxysilyl)propyl methacrylate (TMSPMA) was used to silanize the glass surfaces of the PEGDA microfluidic. The alkoxysilane acted to covalently link the PEGDA hydrogel to the glass surfaces to ensure a tight seal and to prevent shearing of the gel/glass interface after gel immersion in water. The methacrylate group on the end of the silane molecule crosslinked to PEGDA hydrogel during photo-polymerization.

3.3.4 Sequential cross-linking method for patterning of hybrid gel

The device was constructed using a novel sequential photocrosslinking method to deposit adjacent hydrogel slabs of differing material permeabilities (Figure 3.4). Hydrogel pre-polymer solutions of varying PEGDA content were prepared and fluorescent beads were added to aid with image registration. It is important to note that O_2 inhibits the photocrosslinking of PEGDA by quenching the photoinitator generated free radical and terminating the chain-growth reaction early (Figure 3.2b). Oxygen inhibition is particularly a problem in locations where the PEGDA pre-polymer is in contact with the air or gas permeable surfaces. To avoid this problem, the microfluidic was designed to be fabricated in a way

that excluded air from the areas to be crosslinked. A thin layer of low density pre-polymer solution (10%) was placed in the space between the glass slide and a coverglass which was formed by a 100 µm thick tape spacer. Note that the tape spacer was gas permeable and therefore a sufficient distance between the channels and the spacer edge was required to ensure complete cross-linking of the hydrogel around the channels.

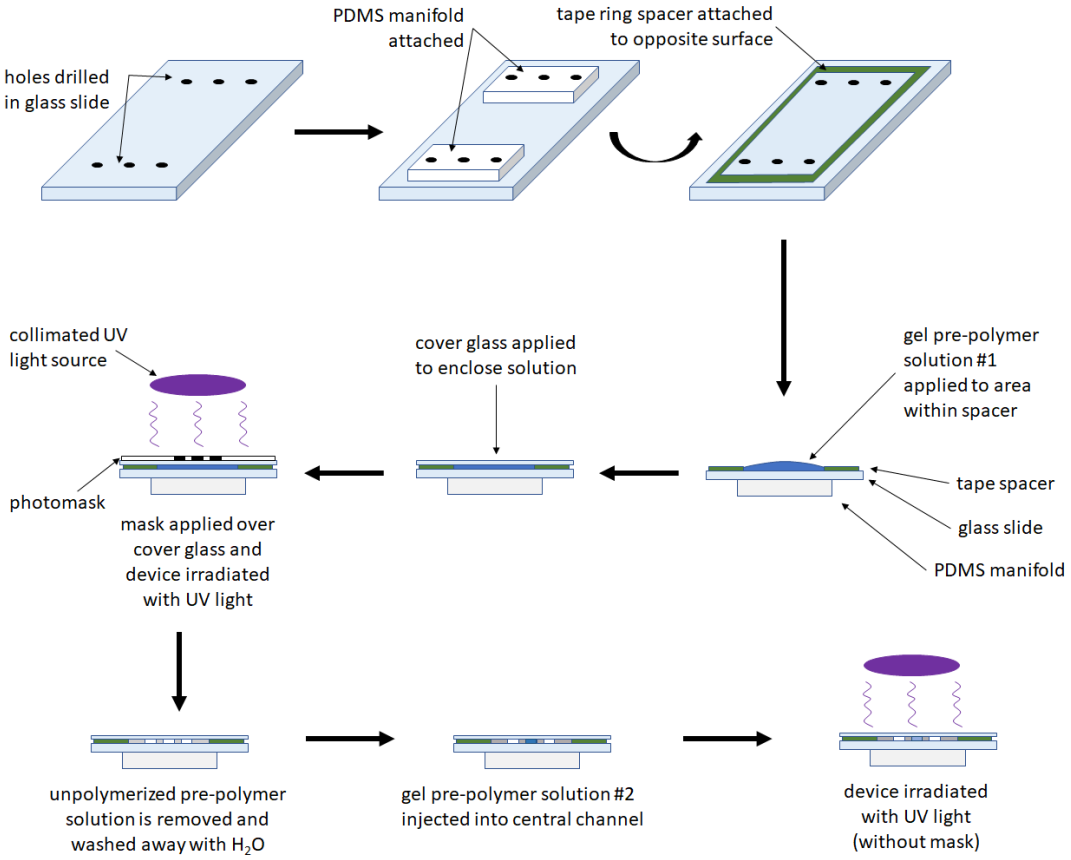

Figure 3.4: Fabrication of PEGDA hydrogel microfluidic. Inlet and outlet holes were drilled into the glass slides and the slides were subsequently washed. PDMS manifolds were then plasma bonded to the glass slides and the slides were silanized. A tape spacer was then attached to the glass slides and pre-polymer solution #1 was applied within the ring spacer. A coverglass was placed over the droplet, and a photomask was applied on top of the coverglass. The device was photocrosslinked with UV light and uncrosslinked pre-polymer solution was washed away with deionized water. Pre-polymer solution #2 was then injected into the central channel and the device was again irradiated with UV light to crosslink the added pre-polymer solution.

A photomask was placed on top of the coverglass (Figure 3.5). The device was then exposed to UV light to form a slab of low density hydrogel with 3

channels. The uncrosslinked low density pre-polymer solution was removed from the channels and the channels were rinsed with water. High density pre-polymer solution (50%) was inserted into the center channel and the device was again exposed to UV light to form a high density hydrogel slab situated between two low density gel layers. Together, these three gel layers were flanked by the perfusion channels within the device.

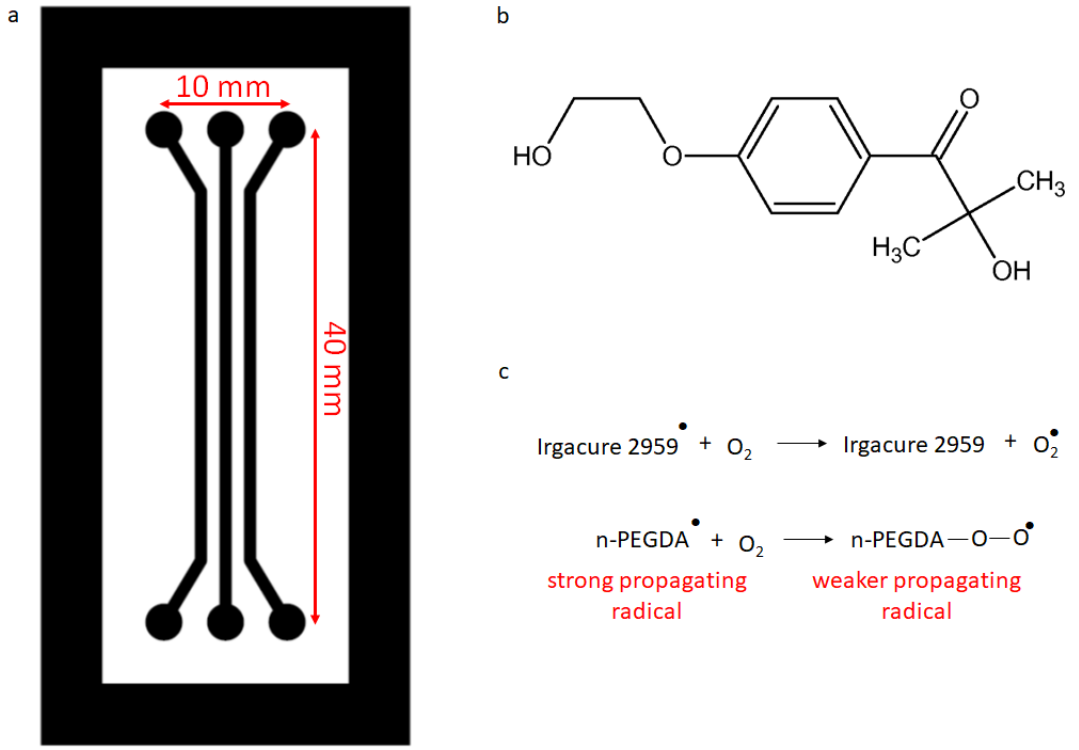

Figure 3.5: (a) UV photomask used for hydrogel microfluidic device fabrication. Dark regions indicate where ink was printed, whereas white regions indicate where the mask was transparent. The mask was printed on a polycarbonate transparency using UV opaque ink and was placed on top of the device coverglass prior to UV exposure. A thin layer of water was used to adhere and optically couple the mask to the coverglass prior to cross-linking. (b) The water soluble photoinitiator, Irgacure 2959 was for PEGDA polymerization. (c) Oxygen, which is highly electronegative, quenches the free radicals generated by the photoinitator compound, inhibiting the polymerization of the hydrogel network. Oxygen can also act to weaken the reactivity of the propagating PEGDA radicals further hindering polymerization.

3.3.5 Gel cross-linking materials and methods

The layered microfluidic devices were fabricated using the UV-crosslinkable hydrogel, poly(ethylene glycol) diacrylate (PEGDA, Sigma, St. Louis, MO, United States). Stock solutions of PEGDA-575 (average molecular number 575) of 0.1

g/mL ("10%") and 0.5 g/mL ("50%") were prepared prior to device fabrication in sterile, filtered water. Additionally, a 0.1 g/mL stock solution of the photoinitiator Irgacure 2959 (Sigma, St. Louis, Missouri, United States) was prepared in ethanol. Pre-polymer gel solutions were then prepared from the stock solutions by adding 1% (v/v) photoinitiator solution to the desired volume of aqueous PEDGA stock solutions. The pre-polymer gel solutions were kept from light and immediately used for gel fabrication after their preparation to reduce the amount of cross-linking prior to UV light exposure. In some experiments, 4 μm diameter polystyrene spheres (FluoSpheres F8859, Invitrogen, Carlsbad, CA, USA) were added to the gel prepolymer solutions to aid image registration. The spheres were labelled with a yellow-green fluorescent marker with an excitation peak at 505 nm and emission at 515 nm for visualization purposes.

The 10% gel pre-polymer solution was manually pipetted into the rectangular space delineated by the rectangular ring spacer. A 24x40 mm No.1 coverglass (Fisher, Pittsburgh, PA, USA) was carefully placed on top of the pre-polymer solution droplet to ensure that no air was trapped between the coverglass and glass slide. At this point, the solution layer was sandwiched between the glass slide and the coverglass, and contained laterally by the adhesive tape spacer. The device was now carefully placed (coverglass side up) under a mask aligner (OAI Model 200, OAI, San Jose, CA, USA) for crosslinking. Prior to irradiation, a photomask containing the device design was placed on top of the coverglass ink side up. The photomask prevented the crosslinking of gel in the location of the device's channels. The device was then exposed to UV light (365 nm, 20 mW/cm^2) for 90 s. After the crosslinking step, the excess pre-polymer solution was removed by vacuum and then washed with water via the inlet and outlet ports on the manifolds. For a three-channel device, the middle channel of the device would be filled with a higher density pre-polymer gel solution (50%), and the device would be exposed to long-wavelength UV light (365 nm, 10 mW/cm^2) for 90 s once more. This additional step would create a heterogenous gel slab consisting of three layers with two different density gels. The crosslinking step also served to crosslink the PEGDA gels to the silanized glass slide and coverslip, ensuring a tight seal between the hydrogel slab material and the glass surfaces. After crosslinking, the microfluidic device channels were filled with filtered water and were stored at 4

℃ in a petri dish with droplets of water covering the inlet and outlet ports on the PDMS manifolds. This step ensured that the gels were fully hydrated and prevented the gels from drying out before their use the following day. Figure 3.4 outlines the hydrogel crosslinking procedure.Prior to perfusion experiments, the devices were connected to tubing via PDMS manifolds attached to the device that accessed the fluid channels through holes drilled into the glass slide. During perfusion experiments, the device would be either perfused with H_2O in both fluid channels, or H_2O in one channel and D_2O in the other. Figure 3.6 illustrates the complete, fabricated device connected to tubing.

Figure 3.6: Multi-layered hydrogel microfluidic. The device consists of a low density layer laterally bounded by a green tape spacer and vertically bounded by a coverglass and glass slide. The low density gel material bounds three channels which are accessed through ports drilled into the glass slide. The central channel is filled with high density gel while the two side channels are kept open for perfusion with water. The high density gel is more translucent than the low density hydrogel. The D_2O inlet is perfused with D_2O or H_2O depending on whether a "H_2O" or "D_2O" was being acquired. The ROI box illustrates the region where the tiled images were acquired. Perfusion fluid entered the device via tubing inserted into PDMS manifolds attached to the glass slide and through holes drilled into the glass slide.

The width of the channels and interchannel spaces were limited by the resolution of UV photo mask, UV light source collimation, and the photocrosslinking reaction. It was found that even with a photomask present, partial cross-linking could occur in masked areas if the exposure time was set too long or if the channel and interchannel widths were too narrow. This issue limited the size of the interchannel spaces to at least 1 mm. Crosslinking outside of the uncovered areas may be due to scattering of the UV light source as it illuminated the sample. Although it was not possible with the UV light source used for this thesis, smaller features have been patterned in PEGDA hydrogels using photocrosslinking [62] and these techniques could be used in future experiments to produce hybrid devices of smaller scale.

3.4 Measuring transient water transport in PEGDA hydrogel plugs

While the diffusion of dyes and large molecules (dextrans, proteins, etc.) have been widely studied in PEGDA hydrogels [63, 7], it was not clear if it was possible to modulate water transport within the PEGDA hydrogels by adjusting the pre-polymer solution density alone. Transient diffusion experiments were used to estimate the relative transport properties of PEGDA hydrogels of different pre-polymer densities.

3.4.1 Transient water transport in PEGDA gel plug

By increasing the pre-polymer concentration, the hydrogel pore size will decrease, and equilibrium water content (when immersed in water) will decrease. Both of these changes will act to relatively increase the interactions between the water and hydrogel polymer network, and possibly slow the transport of water. When designing the hydrogel imaging phantom, it was uncertain whether adjusting the pre-polymer concentration would be sufficient to tune the water transport properties significantly enough to be detected. To determine the water transport properties of PEGDA gels while varying gel density, gel plugs were produced from pre-polymer solutions containing varying concentrations of PEGDA-575 (10%,

20%, 30%, and 50%). Pre-polymer solution was injected into cylindrical PDMS molds and covered with coverglass to isolate the solution droplet from the air. The plugs were photocrosslinked to completion and the unbonded coverglass was removed. The plug was placed into a custom built perfusion chamber sealed with silicone glue. Initially, the immersion chamber was filled with H_2O and perfused at a rate of 100 μL/min. An H_2O-CARS ("H_2O") image was acquired at the center of the gel at a depth of 50 μm as a baseline reference. Using a 5 mL syringe, the perfusion chamber fluid was switched from H_2O to D_2O manually at time t = 0, and then perfused with D_2O at 100 μL/min. Figure 3.7 illustrates the experimental apparatus used.

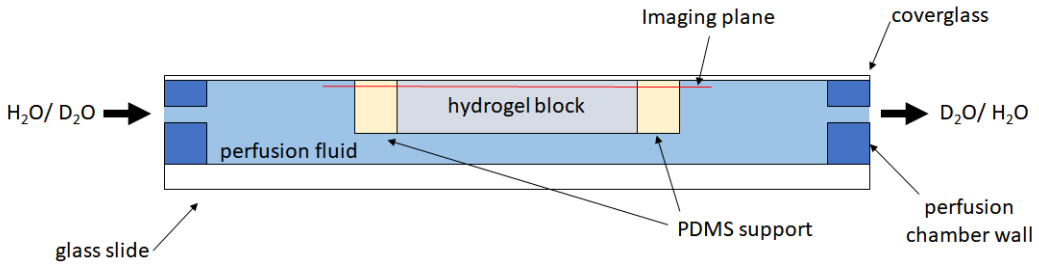

Figure 3.7: Schematic of the apparatus used to observe water transport within PEGDA hydrogel plugs. The hydrogel cyclinder lies within a PDMS support that is a attached to a coverglass. The coverglass is glued to walls of the polycarbonate perfusion chamber. The perfusion fluid was switched from H_2O to D_2O and the H_2O-CARS signal within the gel was recorded over time. The PDMS support and coverglass are in direct contact with the hydrogel plug and act to minimize water exchange at these surfaces.

H_2O-CARS time series images were acquired after the D_2O switch to observe the signal decay over time as the H_2O and D_2O exchanged within the gel, as shown by Figure 3.8. Unfortunately when performing these experiments, the 10% PEGDA plug samples were accidentally destroyed. Given time constraints, repeat experiments were not performed for this formulation of gel. The relationship between CARS signal intensity and H_2O molar concentration is described in Appendix A.2.

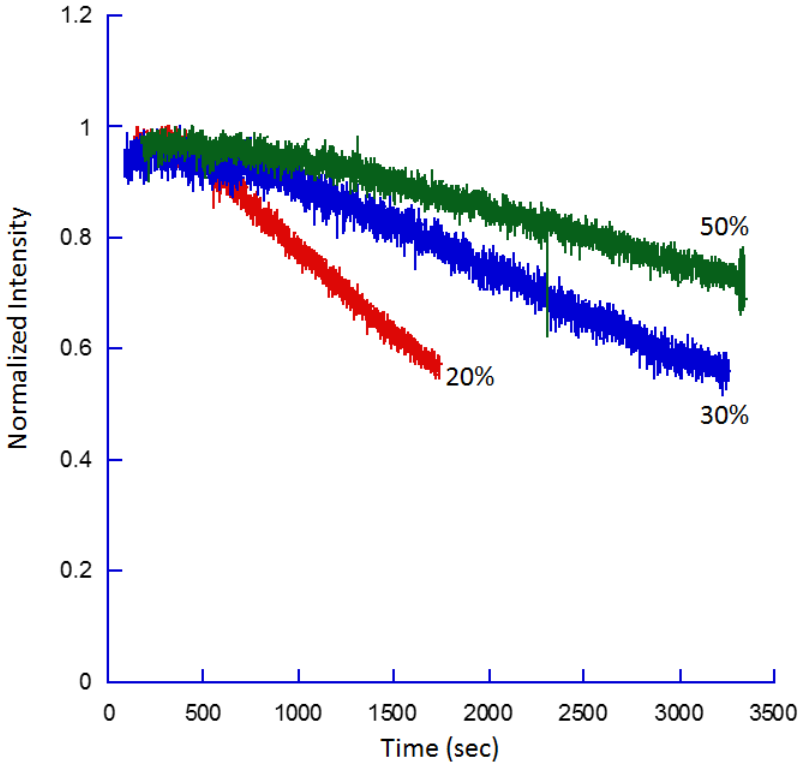

Figure 3.8: Normalized H_2O-CARS signal intensity after H_2O/D_2O exchange within the gel. Profiles from plugs containing 20%, 30%, 50% PEGDA in the pre-polymer solution are shown. The average intensity of the imaging window was recorded over time after the switching of the immersion medium from H_2O to D_2O. Signal decay (and therefore water transport) slows as pre-polymer concentration increases. Time t = 0 occurs at the time of solution switching.

3.4.2 Materials and methods for measurement of PEGDA hydrogel water diffusion coefficients

Variable crosslink-density hydrogel plugs were fabricated from PEGDA. Stock solutions of 0.1 g/mL ("10%"), 0.2 g/mL ("20%"), 0.3 g/mL ("30%") and 0.5 g/mL ("50%") were prepared prior to device fabrication in sterile, filtered water. Additionally, a 0.1 g/mL stock solution of the photoinitiator Irgacure 2959 (Sigma, St. Louis, Missouri, United States) was prepared in ethanol. Pre-polymer gel solutions were then prepared from the stock solutions by adding 1% (v/v) pho-

toinitiator solution to the desired volume of aqueous PEDGA stock solutions. The pre-polymer gel solutions were kept from light and immediately used for gel fabrication after their preparation to reduce the amount of cross-linking prior to UV light exposure.

Plug molds were fabricated by punching 4 mm diameter holes into 2mm thick PDMS spacers that were then subsquently plasma-bonded to a 25x25 mm No.1 coverglass (Fisher, Pittsburgh, PA, USA). Gel pre-polymer solutions were manually pipetted into the plug molds. A 25x25 mm No.1 coverglass (Fisher, Pittsburgh, PA, USA) was carefully placed on top of the pre-polymer solution droplet to ensure that no air is trapped between the coverglass and glass slide. At this point, the solution layer was now sandwiched between the coverglasses, and contained laterally by the PDMS spacer. The cast plugs were placed under a mask aligner (OAI Model 200, OAI, San Jose, CA, USA) for crosslinking. The device was then exposed to UV light (365 nm, 20 mW/cm^2) for 200 s. After gel crosslinking, the plugs weakly adhered to both coverglasses. The non-PDMS-bonded coverglass was carefully removed. The PEGDA plugs attached to the plug casts were then placed in 6-well plates and immersed in H_2O to ensure full hydration of the gels (gel swelling was relatively minimal).

For diffusion measurment, the cast-plug assemblies were glued to a custom built perfusion chamber using silicone glue (3145 RTV, Dow Corning, Midland, MI, USA) as shown in Figure 3.7. The perfusion chamber consisted of a polycarbonate chamber 4 mm deep with inlet and outlet ports attached to opposite ends. The bottom of the chamber was sealed with a glass microscope slide (Fisher, Pittsburgh, PA, USA) using silicone glue.

The chamber was filled with H_2O and the inlet line was attached to a syringe containing H_2O. The microscope objective was brought in proximity to the sample (placed coverglass side up) and optically coupled with H_2O. The objective was moved to the center of the gel plug and imaging was performed at a depth of 50 μm below the coverglass. Initially, the chamber was perfused with H_2O at 100 μL/min via a syringe pump. An "H_2O" reference time series was then captured and the perfusion buffer was switched to D_2O-PSS. The switch was performed by manually flushing the chamber and inlet line with 5 mL D_2O using a syringe and then maintaining D_2O perfusion at 100 μL/min using the syringe pump. Time t =

0 was set to be at the onset of the manual D_2O flush during each experiment after which the "D_2O" time series was acquired. Images were acquired at 5 frames/s using a line-scan rate of 8 kHz, a *xy* pixel size of 690 nm and a field of view of 354 μm (*xy*) (Frame size: 512x512 pixels). The loss of signal was recorded over time during D_2O perfusion. The average intensity of each frame was used to plot signal intensity profiles and water concentration measurement profiles.

3.4.3 Estimation of effective water diffusion coefficient of PEGDA hydrogels

A computation model of the transient water transport experiment was constructed to estimate the effective diffusion coefficient of water within the hydrogel plugs. COMSOL was used to construct a finite element model of the hydrogel plug diffusion experiment, and a MATLAB script was written to fit the COMSOL model with the experimental results.

3.4.3.1 COMSOL model of plug experiment

In the transient water transport experiments, PEGDA hydrogel plugs were immersed in a fluid bath that initially was composed of H_2O and then switched to D_2O rapidly. The plug was bounded at one end by a coverglass, and the curved surface of the plug was bounded by a water impermeable PDMS support. This left only one end of the gel exposed directly to the fluid bath. It was assumed that convection/diffusion along the potential space between the gel and PDMS support was negligible.

COMSOL Multiphysics (version 5.3a) was used to simulate the hydrogel plug water transport studies. The transport of concentrated species module was used to simulate the exchange of H_2O and D_2O within the hydrogel plug after the bath fluid was switched to D_2O at time $t = 0$. The plug geometry was created using the COMSOL geometry builder, which facilitated parametric studies of the model. The hydrogel plug was modeled as a cylinder of length t and diameter d. A no flux boundary condition was applied on all outer surfaces (glass adherent or PDMS bounded face) except at the single exposed end. It was assumed that at the moment of bath fluid switching, the continuous D_2O inflow would fix the

D_2O mole fraction in the bath and at the edge at ~100%. In the hydrogel plug COMSOL model, a concentration boundary condition was placed on the exposed plug face to fix the D_2O mole fraction to 1. Pressure and gravity effects were assumed to be negligible, so the water transport and exchange within the plug was solely attributed to diffusion using Fick's law (Equation 3.1).

$$\vec{N_i} = -D_i \nabla c_i \tag{3.1}$$

For species i, $\vec{N_i}$ is the molar flux ($mol \cdot m^{-2} \cdot s^{-1}$), D_i is the diffusion coefficient ($m^2 \cdot s^{-1}$), and c_i is the concentration ($mol \cdot m^{-3}$). As PEGDA hydrogels are porous media, the diffusion of water within the gel is slowed by interaction between the water in the gel and the polymer matrix. At the molecular level, interactions such as hydrogen bonding between water molecules and the hydrophilic polymer can slow the rate of diffusion of water. At a larger scale, the space the polymer network occupies, the size of the pores, and the tortuosity of the polymer network all can act to artificially increase the "path length" a water molecule has to travel to flow along its concentration gradient, also effectively slowing the transport of water within the gel. The effect of these aggregate phenomena on water transport can be described via an *effective* diffusion coefficient [64]. In the transient hydrogel water transport experiments, it is the effective diffusion coefficient that is modulated when the pre-polymer solution density is varied.

The ratio (K) of the effective diffusion coefficient (D_{eff}) to the self-diffusion coefficient (D_{self}) of each species was used to relate the diffusion coefficients of both H_2O and D_2O within the hydrogels to their bulk self-diffusion coefficients (Equation 3.2). There is an approximately 18.6% discrepancy between the self-diffusion coefficients of H_2O and D_2O [65]. This difference is explained by the larger mass of the D_2O molecule and the stronger deuterium-deuterium intermolecular interactions. Despite the differences in the intermolecular interactions, the diffusion coefficients for H_2O and D_2O within various H_2O/D_2O mixtures are approximately equivalent to their bulk self diffusion coefficients [66]. It was assumed that the slowing of diffusion for both isotopes of water within the gel would be similar, and therefore the ratio between the species' diffusion coefficient in the gel and the species' self-diffusion coefficient, K, would be equivalent. This assumption was supported by the fact that the diffusion of H_2O and D_2O differs

within AQP1 channel proteins by the same proportion as their bulk diffusion coefficients (∼18%) [65].

$$D_{eff} = KD_{self} \tag{3.2}$$

The density of the water isotope mixture (ρ_{mix}) was determined using the isotope densities (ρ_{H_2O} and ρ_{D_2O}) and the mass fractions (w_{H_2O} and w_{D_2O}) (Equation 3.3) [67]. The parameters used to construct the COMSOL simulation of the hydrogel plug experiments are listed in Table 3.1. The diffusion coefficients of the water isotopes at 25 ℃ were used in the computation model to reflect the temperature of gel (and room) during the experiment [66].

$$\rho_{mix} = \frac{1}{\frac{w_{H_2O}}{\rho_{H_2O}} + \frac{w_{D_2O}}{\rho_{D_2O}}} \tag{3.3}$$

Parameter	Value
Plug diameter (d_{plug})	4 mm
Plug thickness (t_{plug})	2 mm
H_2O self diffusion coefficient (D_{H_2O})	2.30×10^{-5} $cm^2 \cdot s^{-1}$
D_2O self diffusion coefficient (D_{D_2O})	1.84×10^{-5} $cm^2 \cdot s^{-1}$
H_2O molar mass (M_{H_2O})	18 $g \cdot mol^{-1}$
D_2O molar mass (M_{D_2O})	20 $g \cdot mol^{-1}$
H_2O density (ρ_{H_2O})	1 $kg \cdot L^{-1}$
D_2O density (ρ_{D_2O})	1.11 $kg \cdot L^{-1}$
Effective diffusion coefficient scaling factor (K)	Varied for fitting purposes
Imaging depth (t_{image})	50 μm
Temperature (T)	25 ℃

Table 3.1: Model parameter values used to generate the plots in Figures 3.9 and 3.10. Note that the parameter value of the effective diffusion coefficient scaling factor (K) was varied in Figure 3.10.

COMSOL was used to solve the mole fraction of both water isotopes at all points in the gel for times $0 \leq t \leq 60$ min after bath fluid switching. The mole fraction at the region of imaging (center of the gel at a depth of 50 μm) was plotted with respect to time after the bath fluid switching. Figure 3.9 illustrates

the COMSOL model geometry and the mole fraction plot of H_2O within the simulated hydrogel plug at a given time.

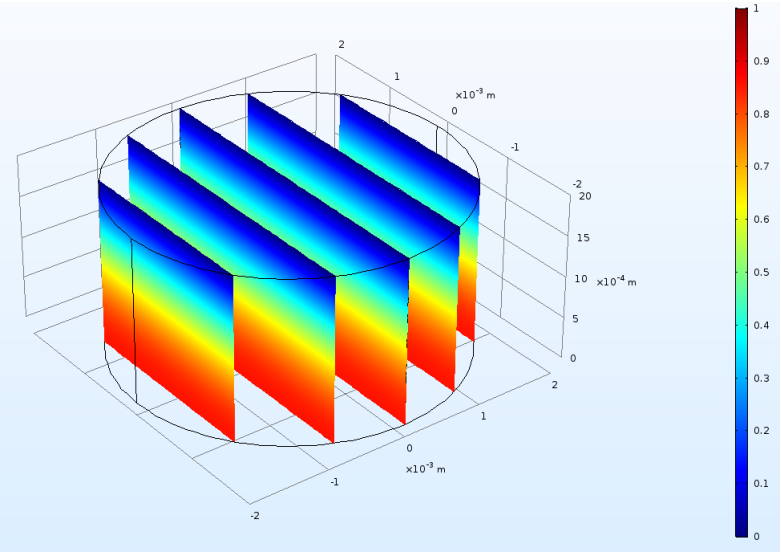

Figure 3.9: COMSOL simulation of water exchange across the hydrogel plug. This colour map illustrates the mole fraction of H_2O at $t = 5$ min with $K = 1$ through a series of slices through the gel plug. The coverglass side of the plug is located at the bottom and the exposed side is located at the top. As time advances, the remaining H_2O within the plug diffuses out of the plug. CARS imaging of the plug was performed 50 μm deep into the plug on the coverglass side (bottom surface on the plot).

A similar plot was generated from COMSOL for several timepoints between the start of D_2O perfusion and one hour later. The mole fraction of H_2O at the experimental imaging position was then plotted vs time. Figure 3.10 shows the mole fraction vs time plot of H_2O within the simulated hydrogel plug at specific point within the plug for various values of the parameter K. As K decreases, the speed of water exchange across the plug is reduced and H_2O persists for a longer period of time within the plug.

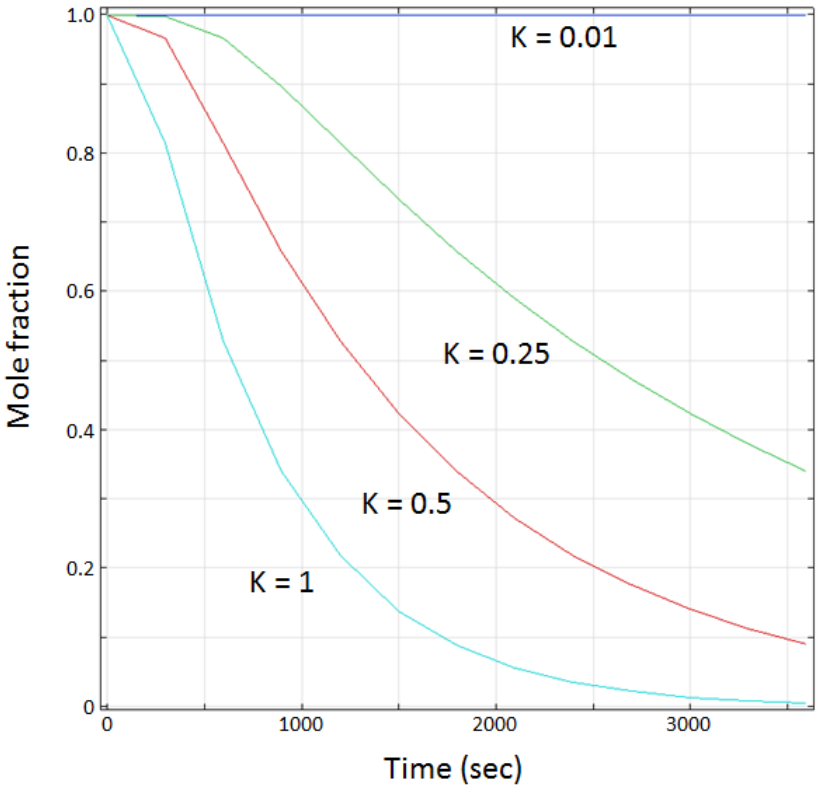

Figure 3.10: Timecourse of H_2O mole fraction within plug at the experimental imaging region for simulated hydrogels with varying values of K. As K is reduced, the rate of decay in the mole fraction of H_2O (and therefore CARS signal) at the experimental imaging point is reduced, indicating the slowing of water transport within the gel (decrease in the effective diffusion coefficient).

The COMSOL simulation of the transient water transport diffusion experiment was fitted to the experimental data to determine the effective diffusion coefficients for each gel. MATLAB Livelink with COMSOL was used to perform the fitting operation. The MATLAB function lsqnonlin was used to perform a non-linear least squares residuals optimization using the default trust region reflective algorithm. The parameter K was varied by the fitting algorithm and plots similar to Figure 3.10 were generated by COMSOL for each iteration, the plot profile was then compared to the experimental data. The residuals between these two data sets were minimized to determine the appropriate value for K for each

gel composition. The experimental profiles were smoothed by a Gaussian filter with a 100-element (20 sec) sliding window. Figure 3.11 displays the resulting fits. The value of K was 0.33 for 20% PEGDA, 0.17 for 30% PEGDA, and 0.12 for 50% PEGDA. Based on this data, the effective diffusion coefficient for H_2O within the plugs is 7.59×10^{-6} $cm^2{\cdot}s^{-1}$ for 20% PEGDA, 3.91×10^{-6} $cm^2{\cdot}s^{-1}$ for 30% PEGDA, and 2.76×10^{-6} $cm^2{\cdot}s^{-1}$ for 50% PEGDA. The experiment demonstrates that by increasing the pre-polymer concentration of PEGDA, it is indeed possible to measurably decrease the rate of water transport in the gel. The diffusion coefficient of the PEGDA gels is decreased roughly 3-fold between the 20% and 50% gels. Based on this data, the 10% and 50% pre-polymer PEGDA solutions were selected for fabrication of the multi-layered PEGDA microfluidic imaging phantom.

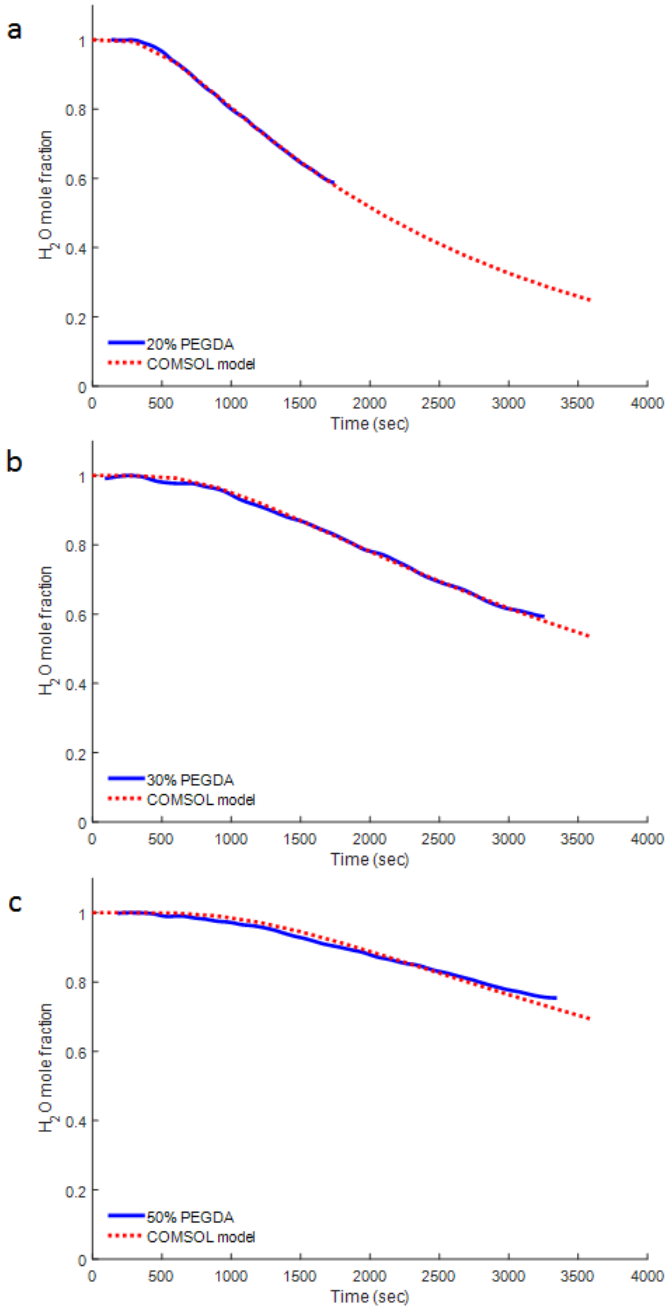

Figure 3.11: Parametric fitting of COMSOL model to experimental data for transient diffusion experiments in PEGDA hydrogels. The experimental collected water concentration profiles were compared to the COMSOL model as the effective diffusion scaling factor was varied to minimize the residuals between the two profiles. The value of K was determined to be (a) 0.33 for 20% PEGDA, (b) 0.17 for 30% PEGDA, and (c) 0.12 for 50% PEGDA.

3.5 Measuring steady-state water transport in PEGDA hydrogel microfluidic

A multi-layered PEGDA hydrogel imaging phantom was designed and fabricated for the purpose of assessing whether CARS microscopy could be used to measure the relative permeabilities of composite structures. The device consists of two channels on either side of a composite slab of PEGDA hydrogel containing layers of gels with two different formulations (10%, 50%). A water concentration gradient was established across the hybrid layer by perfusing one channel with H_2O and the other with D_2O. The H_2O concentration profile was then measured across the hydrogel layer. The shape of the profile was then used to estimate the relative permeabilities of the low and high density gel layers. Although the water effective diffusion coefficient of 10% was not verified experimentally (due to accidental destruction of the sample and time constraints), this formulation was selected in an attempt to ensure a large contrast between the transport properties of the low and high density gel layers.

3.5.1 Steady-state water transport in PEGDA microfluidic

Water transport across the multi-layered hydrogel imaging phantom was observed using a CARS microscope tuned to the 3205 cm^{-1}O-H stretch resonance. At this wavenumber, D_2O acts as a negative contrast to H_2O. The microfluidic was perfused with H_2O in one channel and D_2O in the other channel and tiled water images were recorded across the interchannel hydrogel slab. Water transport across the hydrogel slab was observed by imaging the transport of D_2O contrast as it diffused across the gel layers from the D_2O perfused channel to the H_2O perfused channel. The perfusion channels were considered infinite pools of O-D and O-H bonds, as they were continuously replaced by fresh solutions, allowing for the recording of H_2O concentration profiles at steady state. In this configuration, it is theoretically possible to estimate the relative permeability of the gel layers from the profile data. Prior to imaging D_2O transport, an "H_2O" reference image was acquired by perfusing both channels with H_2O. The perfusion solution of

one channel was then switched to D_2O until the concentration of H_2O within the interchannel hydrogel slab reached equilibrium and a "D_2O" image was acquired.

3.5.2 Image acquistion

In order to generate a water concentration gradient across the hydrogel slab between the fluid flow channels of the hydrogel microfluidic devices, the inlet ports of the microfluidic devices were connected to ∼1 m lengths of polyethylene tubing (OD: 1.09 mm, ID:0.38 mm, SCI, Lake Havasu City, AZ, USA) were inserted into the inlet ports of the microfluidic device, while 10 cm lengths were inserted into the outlet ports. A 20 mL glass bottle was used to collect the waste fluid exiting the outlet tubing. The inlet tubing was attached to 10 mL Hamilton syringes (Hamilton Co., Franklin, MA, USA). One syringe pump (Baby Bee, BASi, West Lafayette, IN, USA)) was used to perfuse both channels at 100 µL/min. One channel was perfused with distilled H_2O, while the opposite channel was perfused either with D_2O (99.9 atom%, Sigma, St. Louis, MO, USA) or distilled H_2O.

Tiled image stacks (30% overlap) were acquired to capture the H_2O concentration profile across the hydrogel slab. The images were captured 1 mm downstream of the outside corner of the perfusion channels on the inlet side (3.12), at a depth of 30 µm. This location was selected to ensure relatively pure concentrations of H_2O and D_2O in the perfusion channels. A shallow imaging depth was used to minimize the effect of shadows created by the flourescent beads in the H_2O-CARS channel. Tiled image stacks were collected for both the "H_2O" and "D_2O" perfusion experiments. The bead signal was detected at 512-528 nm. Images were acquired at 10 frames/min using a line-scan rate of 8 kHz, a xy pixel size of 690 nm, a z pixel size of 1 µm and a field of view of 354 µm (xy) and 20 µm (z) (Frame size: 512x512 pixels).

3.5.3 Image registration and processing

The imaging field of view was limited by the 25x objective used for CARS imaging. To acquire profiles across the entire hydrogel barrier, image tiling was performed. As the hydrogels themselves are relatively featureless, registering the images posed a challenge. Fluorescent beads were added into the pre-polymer

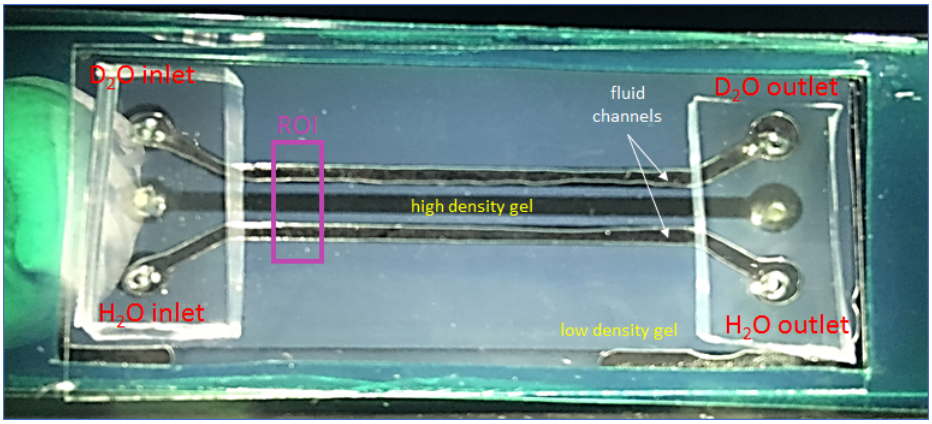

Figure 3.12: Multi-layered hydrogel microfluidic. The device consists of a low density layer laterally bounded by a green tape spacer and vertically bounded by a coverglass and glass slide. The low density gel material bounds three channels which are accessed through ports drilled into the glass slide. The central channel is filled with high density gel while the two side channels are kept open for perfusion with water. Note that in this image, air surrounded by a thin layer of water occupies the fluid channels. The high density gel is more translucent than the low density hydrogel. The D_2O inlet is perfused with D_2O or H_2O depending on whether a "H_2O" or "D_2O" was being acquired. The ROI box illustrates the region where the tiled images were acquired.

solutions prior to gel cross-linking to add feducial markers within the gel that could be used for image registration. The registration tools used for this work were developed in MATLAB by Dr. Bertrand Lucotte at NHLBI [11]. The image analysis procedure is described briefly here: "H_2O" and "D_2O" image stacks were sequentially acquired and collected during the H_2O/D_2O perfusion experiments. First the "H_2O" and "D_2O" image stacks were registered separately (using the beads fluorescence channel) using a phase correlation registration algorithm. The registered "H_2O" and "D_2O" image tiles were then registered together. A Tukey window was used to register the beads by isolating the beads signal from the signal from the rest of the image. Normalized images were computed to measure I_{CARS} and water mole fraction profiles across the microfluidic device. . Figure 3.13 shows the stitched H_2O-CARS and bead fluorescence images for both H_2O and D_2O perfusion conditions. Note that bead fluorescence overlaps with

the CARS channel in both cases.

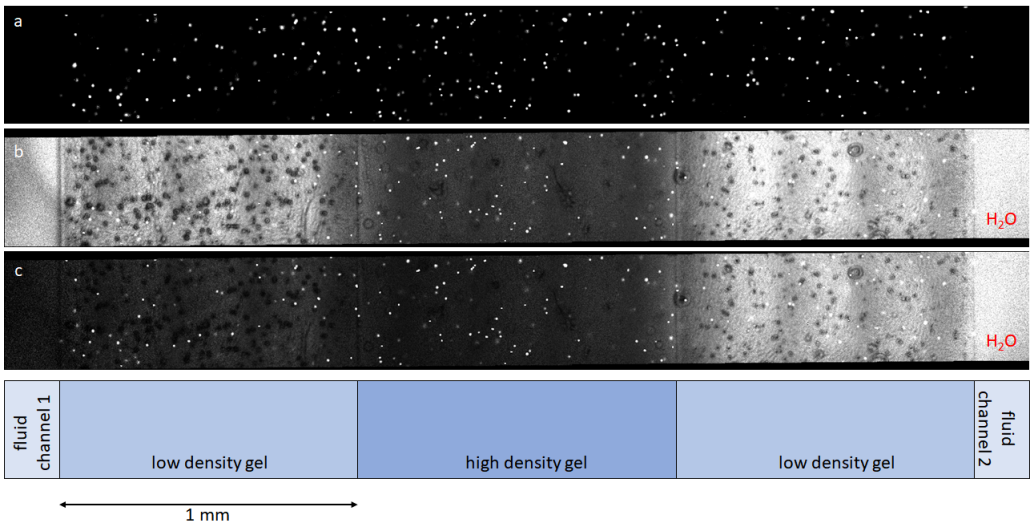

Figure 3.13: Stitched image tiles from hydrogel microfluidic imaging phantom perfusion study. (a) Fluorescence images of labeled polystyrene spheres embedded within the hydrogel layers of the device. The fluorescence spheres were used as feducial markers to register the image tiles and the "H_2O" and "D_2O" images. (b) H_2O-CARS image of the microfluidic device when both fluid channels were perfused with H_2O ("H_2O" image). This reference image was acquired to determine the optical artifacts produced by the sample. Note that there is marked signal attenuation in the central, high density gel layer. Also note that image tiling appears to introduce a repeating artifact due to a "vignetting" effect in each viewing window. (c) H_2O-CARS image of the microfluidic device when the left channel was perfused with D_2O and the right channel was perfused with H_2O ("D_2O" image). D_2O perfusion attenuates signal within hydrogel material in proximity to the left fluid flow channel.

The "H_2O" reference image defines the optical artifacts generated by the imaging phantom. The normalized CARS signal, I_{CARS}, and water concentration profiles were determined by dividing the "D_2O" image by the "H_2O" image (Figure 3.14a) and applying the CARS mole fraction calibration shown in Figure A.2. As shown in Figure 3.13, the H_2O-CARS signal intensity was reduced in the central, high density hydrogel layer compared to the low density hydrogel layer. This

is likely due to both the excitation light attenuation by the gel material, as well as the reduced water content within the gel. Additionally, the signal attenuation produced by the high density gel appears to spread into the adjacent low density gel regions to a small degree. This is likely due to the diffusion of the high density pre-polymer solution prior to its photo-polymerization during device fabrication. Note that even in the normalized I_{CARS} and H_2O mole fraction images (Figure 3.14a and b), bead signal is still present (possibly due to small shifts or deformations that occurred between the "H_2O" and "D_2O" image acquisitions). To remove the bead signal from the H_2O-CARS images, a mask was created from the bead fluorescence channel when performing H_2O mole fraction profile analysis (Figure 3.14c).

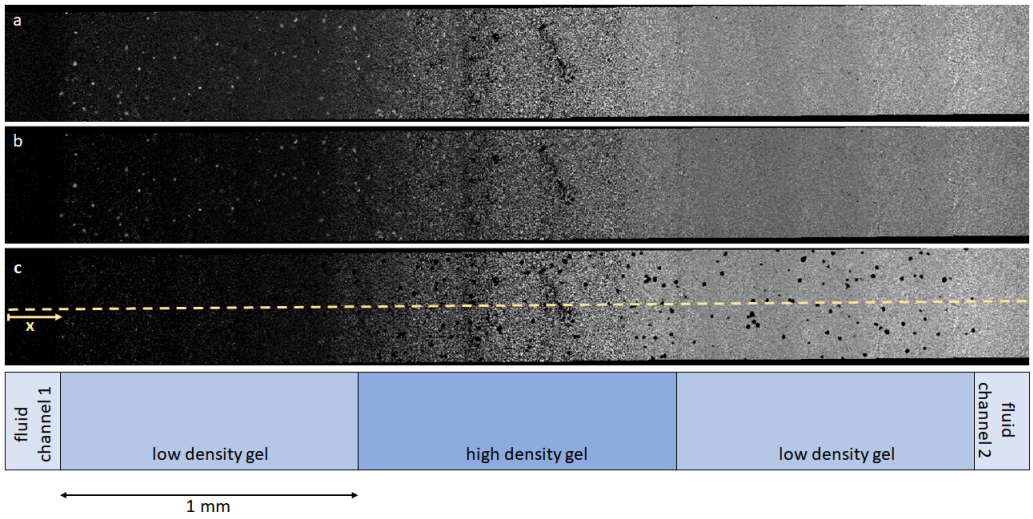

Figure 3.14: Normalized H_2O-CARS images of the hydrogel. The "D_2O" image was divided by the "H_2O" image to remove optical artifacts generated by the sample. Although mostly effective, image normalization failed to completely remove some bead fluorescence signal, as well as some of the shadows produced by the imaging window "vignetting." (a) I_{CARS} image of the perfused imaging phantom. (b) H_2O mole fraction image of the perfused microfluidic. (c) H_2O mole fraction image of the perfused microfluidic with pixels removed by mask generated from the bead fluorescence image. The dashed yellow line indicates that path along which line profiles were calculated.

Line profiles were collected at the middle slice of the I_{CARS}, and mole fraction image stacks (Figure 3.15). The line profiles were averaged over one hundred consecutive, co-planar horizontal lines. The "holes" produced by the elimination of some pixels by the use of the mask, and NaNs generated by division by zero were excluded from the line profile analysis. Due to low signal within the high density gel, the normalized image profiles within this region contain more noise than the regions of the profile within the lower density gel. The mole fraction profile of H_2O possesses distinct changes in slope consistent with the location of gel layer interfaces.

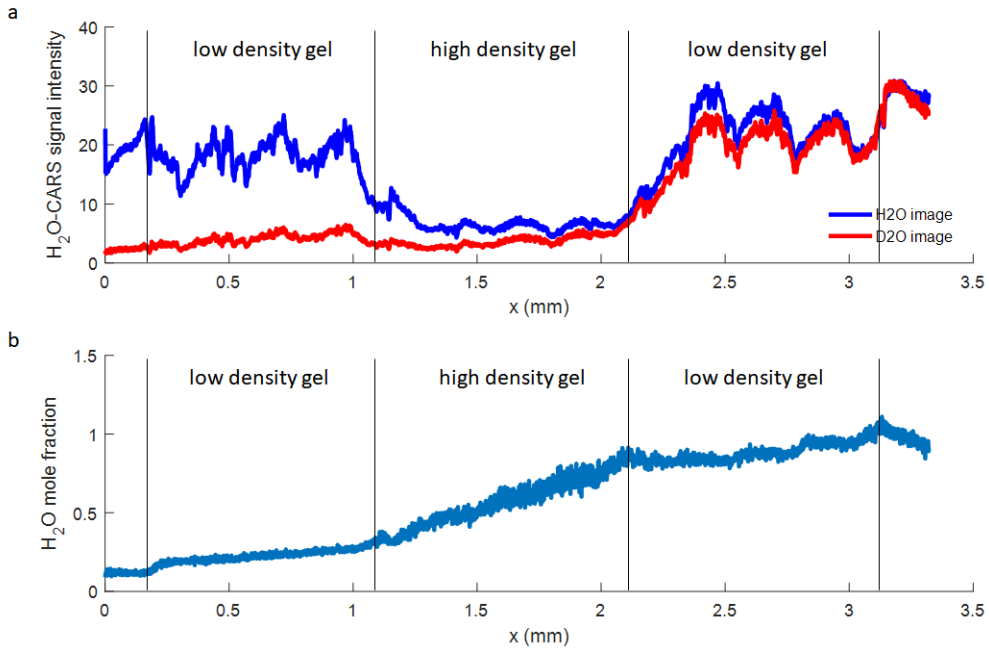

Figure 3.15: Line profiles of the raw H_2O-CARS images and H_2O mole fraction image of the perfused microfluidic (both with fluorescent bead mask applied). (a) Raw signal intensity profiles of the "H_2O" (blue) and "D_2O" (red) image. Note the prominent effect of window "vignetting" in both raw image profiles. (b) Line profile of the H_2O mole fraction image. Normalization acts to remove only some of the "vignetting" effect. The profile component within the high density gel layer, where raw signal intensity is low, increases the amount of noise within the normalized profile.

3.5.4 Estimation of effective water diffusion coefficient of adjacent hydrogel layers

It was hypothesized that by comparing the mole fraction profile of H_2O across the multi-layered hydrogel barrier to the spatial location of the hydrogel layers, the relative permeabilities of the layers could be estimated. The microfluidic imaging phantom was designed to test this hypothesis by creating a system of "resistors" in series via sequential layers of hydrogel materials of differing permeabilities between a source and sink of H_2O analogous to an electrical circuit. The fluid channels of H_2O and D_2O act to continuously supply and remove H_2O and D_2O, respectively, from the ends of the hydrogel barrier and maintain the local H_2O concentration. The total flux, Q_{tot}, across the hydrogel barrier can be determined by Fick's law using Equation 3.4.

$$Q_{tot} = \frac{D_{tot}A}{L}\Delta C_{tot} \tag{3.4}$$

D_{tot} is the overall effective diffusion coefficient of the hydrogel barrier, A is the cross-sectional area of the barrier, L is the gel barrier width, and ΔC_{tot} is the concentration difference of H_2O across the gel barrier. Equation 3.4 can be represented in the form of Ohm's law as shown by Equation 3.6. Figure 3.16 illustrates the application of Ohm's law to the transport of water across the hydrogel.

$$R_{tot} = \frac{L}{D_{tot}A} \tag{3.5}$$

$$Q_{tot} = \frac{\Delta C_{tot}}{R_{tot}} \tag{3.6}$$

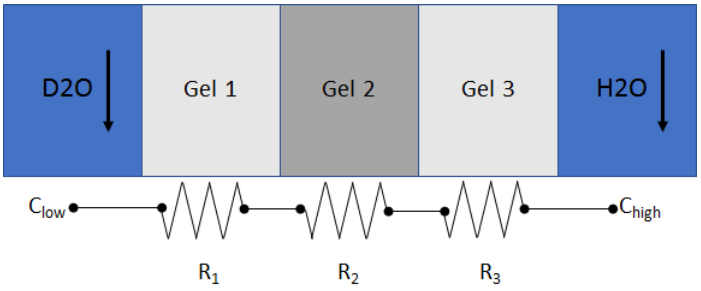

Figure 3.16: Schematic illustrating the application of Ohms law to the transport of water isotopes across the hydrogel microfluidic device. Gel 1 and Gel 3 are the lower density hydrogel material, while Gel 2 represents the high density gel material. The drop in H_2O mole fraction across each gel layer is similar to the drop voltage across each resistor for a set of resistors in series.

At steady-state, the drop in H_2O concentration from the H_2O perfused side of the hydrogel barrier to the D_2O perfused side is a function of the total "resistance" of the gel barrier and the overall concentration gradient across the barrier. As the gel layers are in series, the total "resistance" of the gel barrier is determined by the sum of the individual gel layer "resistances" as shown by Equation 3.8 and the flux through each gel layer is equivalent (Equation 3.9).

$$R_i = \frac{L_i}{A_i D_i} \tag{3.7}$$

$$R_{tot} = \frac{L}{A}\left(\frac{1}{D_1} + \frac{1}{D_2} + \frac{1}{D_3}\right) = R_1 + R_2 + R_3 \tag{3.8}$$

$$Q_{tot} = Q_1 = Q_2 = Q_3 \tag{3.9}$$

Where D_1, D_2, and D_3 are the effective diffusion coefficients and Q_1, Q_2, and Q_3 are the fluxes for gel layers 1, 2, and 3, respectively. Note that the values of L and A are the same for all three gel layers. By combining Equation 3.9 and 3.6, one can then determine the concentration drop across an individual gel layer (Equation 3.10). As shown by Equation 3.12, the ratio of concentration drop across two gel layers is the inverse of the ratios of their effective water diffusion coefficients. The same relationship applies to the slope of the concentration profile

within each gel region, and therefore the mole fraction profile.

$$Q_{tot} = \frac{\Delta C_{tot}}{R_{tot}} = \frac{\Delta C_1}{R_1} \tag{3.10}$$

$$\Delta C_{tot}\left(\frac{R_1}{R_1 + R_2 + R_3}\right) = \Delta C_{tot}\left(\frac{\frac{1}{D_1}}{\frac{1}{D_1} + \frac{1}{D_2} + \frac{1}{D_3}}\right) = \Delta C_1 \tag{3.11}$$

$$\frac{\Delta C_2}{\Delta C_1} = \frac{\frac{1}{D_2}}{\frac{1}{D_1}} = \frac{D_1}{D_2} \tag{3.12}$$

A COMSOL model of water transport across the multi-layered hydrogel region between the perfusion channels in the hydrogel microfluidic was constructed to confirm the series resistor design the microfluidic. COMSOL Multiphysics (version 5.3a) was used to simulate the multi-layered microfluidic steady-state water transport experiment. The transport of concentrated species module was used to simulate the exchange of H_2O and D_2O across the composite hydrogel layer when the device channels are perfused with H_2O and D_2O on opposite sides. The device geometry was created using the COMSOL geometry builder, which facilitated parametric studies of the model (Figure 3.17). Note that the device geometry only includes the hydrogel components of the devices and the fluid channels.

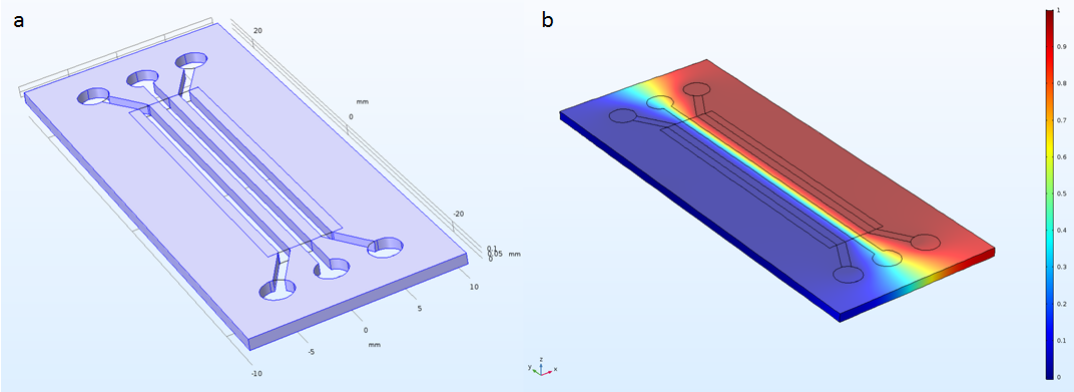

Figure 3.17: Geometry of multi-layered hydrogel microfluidic COMSOL model. Note that the aspect ratio for the z-axis is 10:1 to ease visualization. (a) Volume rendering of the low density gel component of the microfluidic device containing three individual perfusable channels. The central channel is filled with a higher density gel material, while the side channels are perfused with either H_2O or D_2O. (b) Mole fraction plot of the model device at equilibrium (steady-state) when the left channel is perfused with D_2O and the right channel is perfused with H_2O. The colour map shows the transition in the H_2O/D_2O mixture composition as one traverses from one fluid channel to the other across the layered hydrogel barrier. For this plot, $K_{low} = 0.33$ and $K_{high} = 0.12$.

A no flux boundary condition was applied on all outer surfaces (glass adherent or tape spacer bound) excluding the inlet and outlets of the microfluidic channels. Transport of H_2O and D_2O were restricted to within the fluid channels and device hydrogel components. Reflecting the experimental conditions, the channel inlet flows were set to 100 µL/min for both the H_2O and D_2O channels and the outlets were set to 0 Pa gauge pressure. The COMSOL laminar flow module was used to solve for the steady-state fluid flow within the channels, and then the transport of concentration species module was used to solve the steady-state convective diffusion equation for both H_2O and D_2O across the hydrogel components of the device. Pressure and gravity effects were assumed to be negligible, so the water transport and exchange within the hydrogel components of the device was solely attributed to diffusion using Fick's law (Equation 3.1). In the fluid channels, both convective and diffusive transport mechanisms were included in

the model. As in the plug experiments, it was assumed that the diffusion of H_2O and D_2O were retarded by the same factor when diffusing through the hydrogel layers, and the diffusion coefficients within the high and low density gel layers were determined using Equation 3.2. The water isotope mixture density was determined using Equation 3.3. The parameters used to construct the COMSOL simulation of water transport within the multi-layered microfluidic are listed in Table 3.2. The diffusion coefficients of the water isotopes at 25℃ were used in the computation model to reflect the temperature of gel (and room) during the experiment [66]. A cutline was drawn across the experimental imaging location

Parameter	Value
Device thickness (t_{device})	100 μm
H_2O self diffusion coefficient (D_{H_2O})	2.30×10^{-5} $cm^2 \cdot s^{-1}$
D_2O self diffusion coefficient (D_{D_2O})	1.84×10^{-5} $cm^2 \cdot s^{-1}$
H_2O molar mass (M_{H_2O})	18 $g \cdot mol^{-1}$
D_2O molar mass (M_{D_2O})	20 $g \cdot mol^{-1}$
H_2O density (ρ_{H_2O})	1 $kg \cdot L^{-1}$
D_2O density (ρ_{D_2O})	1.11 $kg \cdot L^{-1}$
Scaling factor for low density gel (K_{low})	varied for fitting purposes
Scaling factor for high density gel (K_{high})	varied for fitting purposes
Temperature (T)	25 ℃

Table 3.2: Model parameter values used to generate the plots in Figures 3.17 and 3.18. Note that the parameter value of the effective diffusion coefficient scaling factors, K_{low} and K_{high}, was varied in Figure 3.18.

as shown by Figure 3.12 at a depth of 30 μm to plot the model H_2O mole fraction profile for comparison to the experimental data as shown by Figure 3.18. Parametric studies varying the value of K_{low} and K_{high} demonstrated that the shape of the model H_2O mole fraction profile was solely dependent on the ratio (r_K) of the parameters K_{low} and K_{high} (Equation 3.13).

$$r_K = \frac{K_{high}}{K_{low}} \tag{3.13}$$

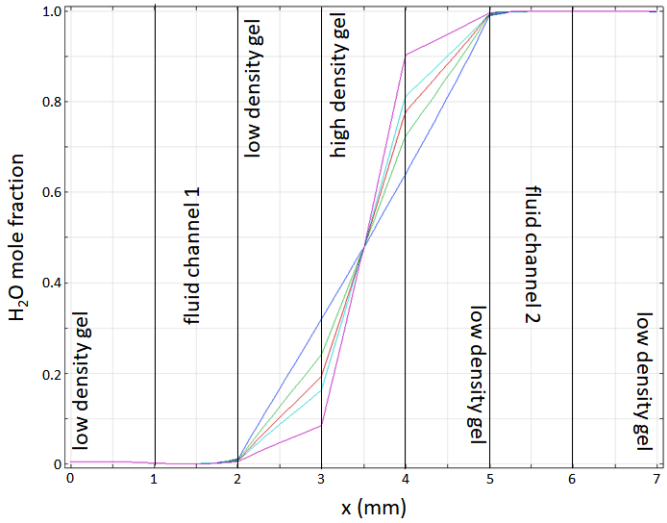

Figure 3.18: COMSOL model H_2O mole fraction profiles for varying values of r_K (0.1, 0.25, 0.33, 0.5, 1). As r_K decreases, the slope of the profile within the high density gel layers become steeper. The proportion of the mole fraction "rise" within the high density gel layer is inversely related to the ratio of the relative diffusion coefficient scaling factors. The COMSOL model confirms that diffusion of water isotopes across the microfluidic devices can be modeled as a set of resistors in series using Ohm's law. In this example, K_{low} was set to 0.33 and K_{high} was varied. However, this behaviour was replicated when other combinations of K_{low} and K_{high} were used.

As shown by Figure 3.18, the ratio between the slope of the mole fraction profile within the high density gel layer and low density layer is the inverse of the ratio of the diffusion coefficients, as would be predicted by Ohm's law for a set of resistors in series. This simplification implies that the ratio between the diffusion coefficients of the gel layers within the composite barrier can simply be determined from the inverse of the ratio of slopes of the mole fraction profile across each gel region.

To estimate the relative transport properties of the high and low density gel layers within the PEGDA imaging phantom, the experimentally obtained mole fraction profile was fit over the three gel layer domains using MATLAB, as shown by Figure 3.19. Three line segments were defined by their endpoints at the

material interfaces, and their values were fit to minimize the residual of the line segment and the experimentally obtained mole fraction profile. The location of the interfaces were included as fit parameters. The fitting was limited to points located within the hydrogel region. The MATLAB function lsqnonlin was used to perform the nonlinear fit between the experimental data and the model mole fraction profile using the default trust region reflective algorithm. The slopes of the three regions were determined to be: s_1= 0.11 mm^{-1} (gel region 1, low density), s_2= 0.50 mm^{-1} (gel region 2, high density), s_3= 0.18 mm^{-1} (gel region 3, low density). $\frac{s_2}{s_1} = 4.5$, while $\frac{s_2}{s_3} = 2.8$. There is a discrepancy between s_1 and s_3 indicating some error in the relative diffusion coefficient measurements, as these gel layers are made from the same material. This discrepancy may be partially explained by the effect of "vignetting" that features more prominently in gel layer 3. It is therefore likely that the comparison between gel layers 1 and 2 is more accurate than a comparison between gel layers 2 and 3.

Vignetting is the apparent reduction of the image brightness at the image periphery when compared to the central area of the image. When capturing tiled images of the hydrogel microfluidic under different perfusion conditions, vignetting was apparent in each tile. Registration and normalization of the images did not completely remove the vignetting effect, particularly in the "H_2O" perfusion side of the device, where the greatest amount of signal is generated. In scanning microscopy, the objective lens, laser, or detector can all contribute to vignetting. The microscope used to acquire the tiled images operates by beam scanning. The laser beam path is deflected by the scanning apparatus prior to passing through the microscope objective and to the sample. This deflection can introduce off-axis aberrations into the excitation beam as it reaches the sample via the objective lens. As CARS imaging is particularly dependent on the combining of multiple beams at two wavelengths, these aberrations could potentially impact signal generation at the PSF as well as image quality. The effect would likely be most apparent within the brightest regions of the image (the "H_2O" perfusion side). A possible way to remove vignetting during image acquisition is via sample scanning. Instead of deflecting the beam path, the sample can be moved while the beam remains stationary. This solution is potentially practically

cumbersome and may not be feasible mechanically without adding great complexity to the microscope apparatus. A simpler solution, which was not available at the time of this experiment, is to use a reduced magnification objective lens so that fewer tiles, with less beam deflection in each tile, would be required to image across the microfluidic device. Unfortunately, only one CARS compatible objective lens was available at the time of this experiment (25x).

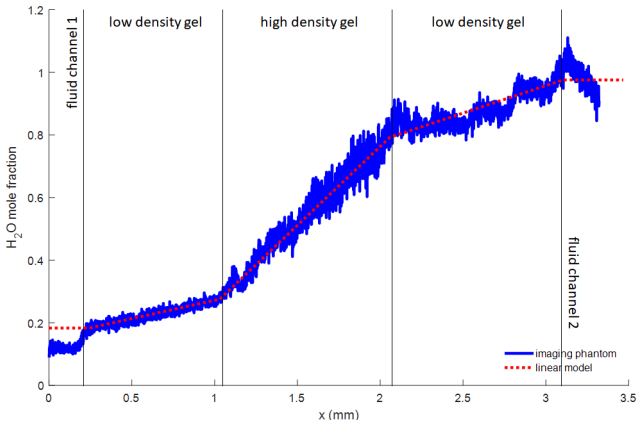

Figure 3.19: The experimentally obtained H_2O mole fraction profile was fitted to a linear model to obtain the profile slopes within each gel layer. The slopes of the three regions were determined to be: 0.11 mm^{-1}, 0.50 mm^{-1}, 0.18 mm^{-1}. The slopes indicate that the central gel layer retards water transport 3-4 fold compared to the lower density gel formulation. Note that there is a discrepancy between the slopes of the two low density gel regions. This may be partly due to the influence of the window "vignetting" which is more prominent in the right layer. Due to time limitations, this experiment was only performed with one sample.

The linear fit predicts that the low density gel has roughly 3-fold greater effective diffusion coefficient than the high density layer, which is consistent with the measurements gathered from the transient plug diffusion experiments. This result indicates it is indeed possible to estimate the relative transport properties of the layers within a composite structure using H_2O-CARS microscopy. While this method has been attempted by the Laboratory of Cardiac Energetics in some biological settings, it has not been previously applied to the field of hydrogels,

nor could relative permeability information be determined. This experiment also demonstrated that it was possible to spatially identify the locations of permeability changes at sub-millimeter resolutions. While in this particular experiment the gel layers could not be fabricated to smaller dimensions due to the limitations of the manufacturing equipment available, this measurement technique could readily be applied to smaller structures. CARS microscopy may provide a useful water transport measurement tool in the design and validation of water permeable hydrogel structures, such as contact lenses, drug delivery systems, and microfluidics.

Chapter 4

Microvessel microfluidic to study endothelial barrier function

4.1 Introduction

The microvascular endothelium is the major interface between the blood and tissue [68, 69]. This barrier is semipermeable and restricts the entry of blood cells and plasma into the surrounding tissue while regulating the transport of oxygen, metabolites, and waste products between the blood and tissue. Importantly, the microvascular endothelium has a different functional role compared to the arterial or venous endothelium. While arteries and veins are conduits of blood (fluid) flow at high and low pressure, respectively, the microvascular endothelium facilitates fluid exchange between the blood and surrounding tissues. Plasma fluid, nutrients, and, sometimes cells, are free to enter the surrounding tissues and then either leave the tissue by re-entering the circulation at the post capillary venules or draining via the lymphatic system. The endothelial barrier of the microcirculation is therefore more permeable than that of the larger conduit vessels and more specialized for water/nutrient transport [37]. Additionally, the microvasculature differs in specialization depending on the body location and tissue type. The microvasculature of the kidney glomerulus is fenestrated to facilitate renal filtration. In the gut and skeletal muscle, the microvasculature is specialized to express an abundance of membrane transport proteins and vesicles to mediate the transfer of metabolites and waste products. The microvasculature of the central

nervous system (CNS) is, perhaps, the most specialized in the body. The blood-brain barrier (BBB) tightly regulates the environment of the CNS and is more restrictive to compounds and drugs than in other areas of the body. Clinically, the BBB presents a significant challenge to pharmacologic therapy of CNS disease such as brain tumours. A greater understanding of the composition and function of the microvasculature may inform the development of more effective delivery of the therapeutics to target tissues. Changes in the permeability and transport properties of the microvascular endothelium are important in several disease processes [11, 69, 37] including diabetes, atherosclerosis, cancer, and aging.

Visualizing the microvascular water permeability barrier is inherently very challenging. The size and fragile structure of microvessels makes dissection and cannulation unfeasible. The high permeability and surface area of the microvasculature makes steady state perfusion difficult. Initial experiments by the Laboratory of Cardiac Energetics perfusing whole rat skeletal muscle (via the femoral artery *in vivo*) with D_2O demonstrated rapid equilibration of the surrounding extravascular space, making it near impossible to observe a water concentration gradient across capillary walls. Because it is virtually impossible to perfuse the extravascular space in an *in vivo* preparation, and because of the highly branched geometry of microvasculature, a water concentration gradient is very difficult to establish across the microvascular walls at specific regions for observation. Due to physical limitations, it is very difficult to cannulate and perfuse microvessels, therefore larger arteries are used. Unfortunately, between the level of a "perfusable" vessel and the level of the microvessels, the vasculature branches many times, and the perfused D_2O is diluted. A cannulated vessel *ex vivo* preparation can provide an opportunity to study the transport properties of smaller vessels ($\sim$100 μm), but these vessels are still relatively large compared to the much smaller and more numerous capillaries and venules that account for the vast majority of the exchange surface area between the blood and the tissues. These larger vessels are specialized to regulate the delivery of blood to downstream capillary beds rather than to perform chemical exchange. In the CNS, the vascular permeability of all vessels in the subarachnoid space is highly restricted, so the BBB effectively exists in all vessels of the CNS [34]. However, the anatomic composition of the BBB varies with vessel size. At the level of the

arteries and arterioles, the BBB consists primarily of the arterial endothelium and basement membrane, while at the level of the microvasculature, the BBB is composed of endothelium, basement membrane, and support cells including pericytes and astrocytes. CARS imaging of the cannulated, perfused microvessel is also challenging due to optical considerations [11]. Imaging across the arterial barrier requires optimization between sufficient imaging resolution and optical aberration introduced by the sample itself. Because z-resolution of an upright microscope is relatively poor compared to the xy-resolution, imaging across the arterial wall at the top of the artery is not feasible. At the horizontal midplane of the artery, where the artery wall is vertical, and where the theoretical spatial resolution across the artery is best, the CARS image is degraded considerably due to optical distortion of the PSF. The optical distortion is a function of both the cylindrical geometry and the distance that light passes through tissue of the artery wall, especially the dense smooth muscle and connective tissue layers.

In vitro models of perfusable blood vessels using microfluidic systems provide an opportunity to better observe the microvascular permeability barrier. Microfluidic systems have many potential advantages compared to traditional culture systems, *ex vivo*, and *in vivo* models due to the degree of control these systems offer in regulating the physical and chemical environment exposed to the cells. Depending on the design of the microfluidic system, the transport of nutrients, chemical factors, and fluids can be precisely controlled both temporally and spatially within physiological accurate length and timescales [70]. Depending on the cell types cultured within the device, different microvascular models can be produced and investigated. Additionally, microfluidic systems typically have high sample reproducibility and are cost effective (low reagent use, small size) and are well suited for high-throughput applications (i.e. drug screening).

With microfluidic systems, it is possible to culture cells and organoids in precisely controlled environments. In such systems, the concentration and distribution of nutrients, metabolites, and gases can be tightly controlled. The physical characteristics of the culture environment can be fine tuned for both biological and experimental purposes. Monolayers of endothelial cells can be cultured within the channels of a microfluidic device. Through my collaboration with the Biointerface group under the supervision of Dr. Shery Huang, I fabricated and

refined a "microvessel-on-a-chip" system to study the microvascular permeability barrier composition and function. The microvessel microfluidic permits much greater optical access to the transverse plane of the endothelial tubes cultured within the channel allowing greater potential imaging resolution of the endothelial barrier due to the lack of surrounding connective tissue and smooth muscle. Additionally, the cultured microvessels can be perfused for permeability studies without the need for manual cannulation. Two microvascular models were fabricated using two different cell types: HUVEC and hCMEC/D3. HUVEC vessels were used as a model of the systemic microvasculature while the hCMEC/D3 vessels were grown to model the BBB *in vitro*.

Using microfluidics as a means to model the physiology and function of microvessels *in vivo* poses many challenges. Microfluidic devices typically possess straight channels with rectangular cross sections which differ greatly from more rounded and tortuous microvasculature. This difference in the physical environment may possibly influence cellular gene expression and behavior [71]. Additionally, it is known that the endothelium interacts both physically and chemically with the connective tissue and smooth muscle surrounding it within *in vivo* vasculature [34]. These interactions may also play a role in vascular barrier formation, endothelial specialization, and endothelial function. As the endothelial tubes within the microvessel microfluidic are cultured in isolation from other cell types, these vessels may differ from those *in vivo*.

Cellular polarization is an important feature of many cellular barriers. Within the *in vivo* vasculature, endothelial cells express some surface proteins preferentially on either the apical or basolateral membrane to facilitate the transport of substances, immune system function, or cell adhesion. As part of my work in characterizing the "microvessel-on-a-chip" system developed by the Biointerface group, I investigated whether the endothelial cells within the microvessel environment exhibited polarization similar to what is observed *in vivo*.

4.2 Microfluidic based microvessel culture systems

In vitro fabrication and culturing of microvessels has been a longstanding challenge of the tissue engineering field. Microfluidics provide several advantages in

the fabrication of vascular culture models as one can control flow, structural geometry, chemical gradients, as well as provide co-culture environments [72]. Several strategies have been developed using microfluidics to culture microvessels for a variety of applications and experiments [71]. Microfluidic microvascular models typically involve culturing endothelial cells in monolayers on structures with 2D planar geometry by seeding the device channels with cells suspended in culture medium. Due to the typical scale of the flow channels within microfluidics, laminar flow can be easily imposed on the cultured cell monolayers to mimic the flow environment *in vivo*.

The simplest microfluidic microvascular systems consist of a single channel within which a monolayer of cells is cultured [73]. Typically in these devices, the walls of the device channel must be treated or coated in some way to promote the binding and differentiation of endothelium. Coatings such as collagen I, collagen IV, gelatin, fibronectin, as well as others have been used to promote cellular adhesion [74]. Collagen IV, in particular, has been used in microvascular culture models as it is a key component of the vascular basement membrane. Cell seeding of these devices is performed after channel coating.

More complex microvessel microfluidic systems can incorporate hydrogels containing extracellular matrix (ECM) components. In ECM-containing microvascular microfluidic devices, endothelial cells can be either cultured within the hydrogel bulk or can be cultured in a monolayer onto the sidewall of a hydrogel slab that lies between two fluid flow channels [71]. When the endothelium is cultured within the hydrogel bulk, it must be mixed into a pre-polymer solution and injected into the device along with the ECM. Studies of angiogenesis, and microvascular network formation have been performed in such systems [74]. In devices in which an endothelial monolayer is grown adjacent to a hydrogel slab, the hydrogel slab itself may be used to culture an additional cell type (such as astrocytes). This type of device is particularly useful in studying cell migrations and vessel interaction. Typically, the uncrosslinked solution of ECM component and migrating cells is injected into a space bounded by narrowly spaced pillars to prevent the hydrogel pre-polymer solution from leaking into the adjacent fluid flow channels. Following this procedure, the microvessel channel is coated with cellular adhesion factors. The microvessel is then seeded via the same process as a single channel device.

However, in this case, the endothelial cells cultured onto hydrogel compound can form more complex interactions with the ECM. The ECM more closely resembles the extravascular environment *in vivo*, and these interactions may inform the differentiation of the cultured endothelial cells [74, 75, 76, 77]. The Biointerface group uses such devices to study the extravasation of gliobastoma cells.

4.2.1 PDMS-based microfluidic devices

Microfluidic devices used for biomedical applications are commonly constructed from polydimethylsiloxane (PDMS). PDMS is a silicon-based organic polymer (silicone) that possesses many mechanical and chemical properties that make it suitable for microfluidic device fabrication. Cross-linked PDMS is biocompatible and is non-toxic to cultured cells [78]. PDMS is optically transparent and has low autofluorescence [79], making the polymer suitable for applications requiring fluorescence imaging. Mechanically, PDMS is elastic and flexible, and this facilitates the sealing of imprinted channels to glass surfaces, an otherwise challenging process for structures with small features [80]. PDMS can be molded around finely detailed features with great fidelity and the surface of PDMS can be treated with oxygen plasma to form free radicals that rapidly and tightly bond to glass, forming a tight seal [80]. PDMS is gas-permeable and facilitates the transport of oxygen. Unfortunately, this property can also facilitate the evaporation of water out of the device, possibly causing changes in the osmolarity of solutions within the device [81]. PDMS can also retain organic (non-polar) solvents which can leach out of the material over time into the solutions within the device, a potential source of contamination [81].

In this work, a simple, single-channel PDMS device was used to characterize the growth and development of cultured microvessels *in vitro*. The device consisted of an "S-shaped" channel (120 or 240 μm wide, 100 μm tall) with an inlet and outlet for allowing the channel to be perfused as shown in Figure 4.1. The curved shaped of the channel was used to replicate channel geometry of several device designs used by the Biointerface group. The open surface of the channel was sealed by a PDMS coated glass coverslip. This was done to ensure that the

cells seeded within the channel were exposed to the same chemical and physical environment at all channel surfaces.

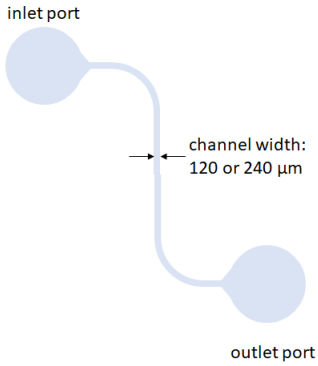

Figure 4.1: Microvessel microfluidic design used in this work

4.2.1.1 PDMS channel surface modification

Endothelial cells express adhesion proteins on their outer membranes to facilitate their attachment to surfaces. *In vivo*, these proteins mediate either cell-cell attachments or cell-matrix attachments. Cell adhesion is an important process in the polarization and specialization of endothelial and epithelial cells [82]. Previous experiments by Christina Bertulli and Magda Gerigk at the Biointerface group have shown that HUVEC cells do not successfully attach and grow within the PDMS channel without pre-treatment of the channels with collagen IV. Collagen IV is an important component of the vascular basement membrane *in vivo*, and it provides an attachment point for endothelial cells lining the vessel lumen [76]. To coat the PDMS microfluidic channels with collagen IV, the channel surfaces were first made hydrophilic (by the generation of surface silanol groups) by exposure to plasma during the assembly process [83]. Surface hydrophilicity was essential during the coating process to ensure proper wetting of the channel surfaces. Within 2 minutes after plasma exposure and device assembly, the channels were coated with poly-D-lysine (PDL) to ensure the channels were still hydrophilic during PDL coating. The PDL facilitates the attachment of collagen IV to the PDMS surfaces. Following PDL coating, the channels were dried and coated with collagen IV.

4.2.2 Endothelial cell models

Commercially available primary cells and cell lines were used in the work described in this thesis. Cell lines are economic, immortal, and better adapted to culture system environments. Due to their indefinite proliferation, cell lines can be maintained *in vivo* for very long periods of time and through many cell divisions. However, cells from cell lines have lost some attributes of the original cells they were derived from, making them less representative of the *in vivo* state. Cell lines are made immortal by techniques that either involve mutating the cellular genome or introducing oncogenes that alter cell cycle checkpoint regulation. These alterations result in higher error rates in genetic replication and cellular adaptations to the nonphysiological culture environment, resulting in deviations of cell physiology from the *in vivo* state. Primary cells are directly isolated from tissue, and therefore more closely resemble cells *in vivo*, but they have limited lifespans. These cells are genetically and phenotypically more similar to cells in the *in vivo* state, and are more functionally representative of the tissues from which they are derived. While primary cells are preferred for investigating more biologically relevant questions, cell lines can be useful when troubleshooting experimental parameters or microfluidic device design.

4.2.2.1 Primary human umbilical vein endothelial cells (HUVECs)

HUVECs are primary cells isolated from the endothelium from neonatal umbilical veins. They are usually harvested from umbilical cord samples donated after delivery of a human neonate. HUVECs have been studied extensively and are commonly used as an *in vitro* model to study the function and biology of endothelial cells [72]. In this work, pooled HUVECs were used to improve the repeatability of experiments. The HUVECs were isolated from 10 individual donors which helps to reduce batch-to-batch variability observed in single donor cell isolates due to differences in genetics, external factors, etc. Pooled HUVECs from Lonza were used for the work described in this thesis and were maintained using EBM-2 medium (also from Lonza).

4.2.2.2 hCMEC/D3

Although HUVECs are an established model for endothelium in cell culture systems, they are not an ideal physiologic model of the brain microvasculature. The umbilical vein (*in vivo*) does not possess endothelium with the same specialization or "tightness" as is found in the vessels of the CNS. CNS endothelial cells are a key component of the BBB and express additional permeability regulating proteins and transporters to more efficiently exclude foreign substances from the CNS parenchyma. To more closely model the CNS *in vitro*, the immortalized brain microvascular hCMEC/D3 (CMECs) cell line was used. This cell line was derived from human temporal lobe microvessels isolated from tissue surgically excised for the control of epilepsy and subsequently immortalized following isolation [84]. In this work, CMECs were cultured in the microvessel microfluidic system to assess the growth and vessel formation of this new cell type within this device for studies of BBB microvascular permeability and function. The Biointerface group additionally intends to study the invasion and spread of gliobastoma through CMEC microvessels within this microfluidic system. CMEC microvessels readily formed within the microvessel device utilizing a similar protocol as had been previously developed for HUVECs (Figure 4.2). CMECs were cultured on flasks coated with calf-skin collagen and required a specialized culture medium, EGM2-MV (Lonza).

4.3 Microvessel microfluidic materials and methods

4.3.1 Microvessel microfluidic device fabrication

The microfluidic devices used in this work were designed using AutoCAD software (AUTODESK, Mill Valley, California, US) and is represented in Figure 4.1. The design consists of a single channel of 100 μm in depth, and 120 (narrow) or 240 (wide) μm in width, with a long, straight central section. The fabrication, assembly, and seeding procedures for both device designs were identical. Soft lithography was used to produce the microfluidic channels from PDMS. A photomask was

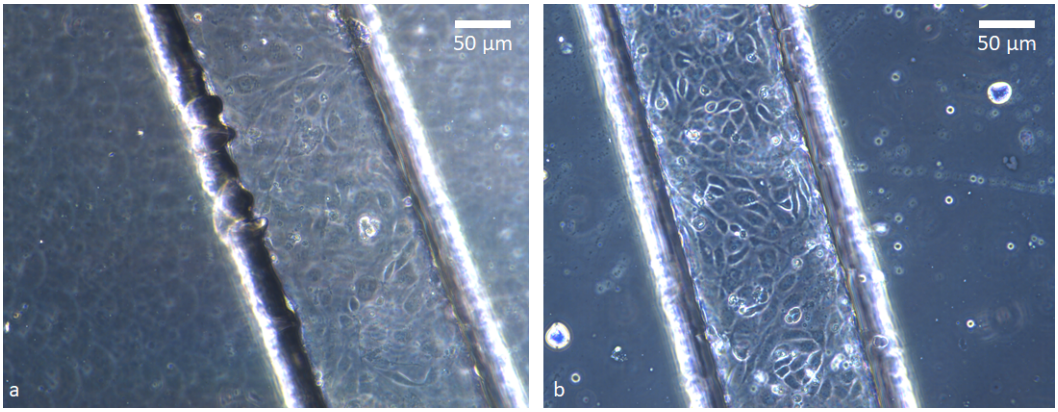

Figure 4.2: CMEC microvessels were successfully grown within the microvessel microfluidic. CMECs (a) possess a more elongated morphology with long extensions compared to HUVECs (b). Both microvessels are composed of a confluent tubular monolayer of cells. HUVEC cells tend to take on more polygonal shapes with fewer long projections. The significance of this morphological difference is unclear.

produced from the AutoCAD device designs by Micro Lithography Services Ltd. SU-8 photo resist was applied to a 6" silicon wafer (University Wafer, Boston, MA, USA) by spin-coating to form a 100 µm layer. The photomask was then applied over the photoresist and exposed to long wavelength UV light. UV exposed regions of the photoresist layer crosslink and remain attached to the silicon wafer while the uncrosslinked material is removed by a developing solvent forming the device pattern master.

4.3.1.1 PDMS casting and bonding of devices

A 10:1 ratio of PDMS base to curing agent (Sylgard 184, Sigma Aldrich, St. Louis, MO, USA) was mixed and degassed in a vacuum desiccator. The mixture was then poured over the patterned silicon wafer master in a 10 cm plastic petri dish. The dish was then placed in the vacuum desiccator to remove air bubbles and transferred to an oven to be baked for 3 hr at 70 ℃ to allow the polymer to cure. The cured PDMS devices were individually cut from the PDMS layer, carefully peeled from the master, and 0.75 mm inlet and outlet holes were punched in

PDMS blocks using a biospy puncher. The PDMS blocks containing 3D impressions of the channel design formed the "upper" part of the device. The bottom wall of the device channels were created using PDMS coated 22 mm diameter round glass coverslips (#1, Academy Science Limited, Beckenham, UK) using a coating protocol previously used for microfluidic studies of neuron growth [85]. In brief, coverslips were placed on top of droplets of unpolymerized PDMS in a 10 cm plastic petri dish. The coverslips were pressed against the droplets to leave a very thin layer of PDMS between the coverslips and the petri dish. The coverslips were cured for 3 hr at 70 ℃. The coverslips coated with a cured PDMS layer were carefully peeled away from the petri dish using tweezers. Additionally, inlet and outlet wells were made from 2 mm blocks of PDMS prepared in 3 cm petri dishes using the same curing procedure as detailed above. A biopsy punch was used to introduce 2 mm diameter holes in the blocks to serve as the wells. The PDMS "uppers", coverslip "bottoms", and wells were cleaned of debris using scotch tape and then soaked in ethanol overnight. The ethanol soak was performed to remove uncured monomer and curing agent from the PDMS casting process as these compounds were hypothesized to be potentially toxic to cells. The ethanol soak was also performed to sterlize the PDMS components prior to cell seeding. The device components were then dried at 80 ℃ for 1 hr. The devices were plasma bonded using a plasma cleaner (Harrick Plasma, Ithaca, NY, USA) at a power setting of high for 3 min under vacuum. The uppers were first bonded to the wells on the non-patterned surface such that the wells enclosed the inlet and outlet ports of the device. The PDMS coated surface of the bottoms was bonded to the patterned surface of the uppers to create a sealed channel entirely bounded by PDMS. The plasma cleaning of the device left the internal surfaces of the device channel hydrophilic, a necessary property for subsequent device coating. In some experiments, the PDMS inlet and outlet wells were bonded with a silicone glue (3145 RTV, Dow Corning, Midland, MI, USA) instead of plasma bonding to test the effects of the glue exposure on the growth of cells within the devices. Figure 4.3 illustrates the PDMS device assembly process.

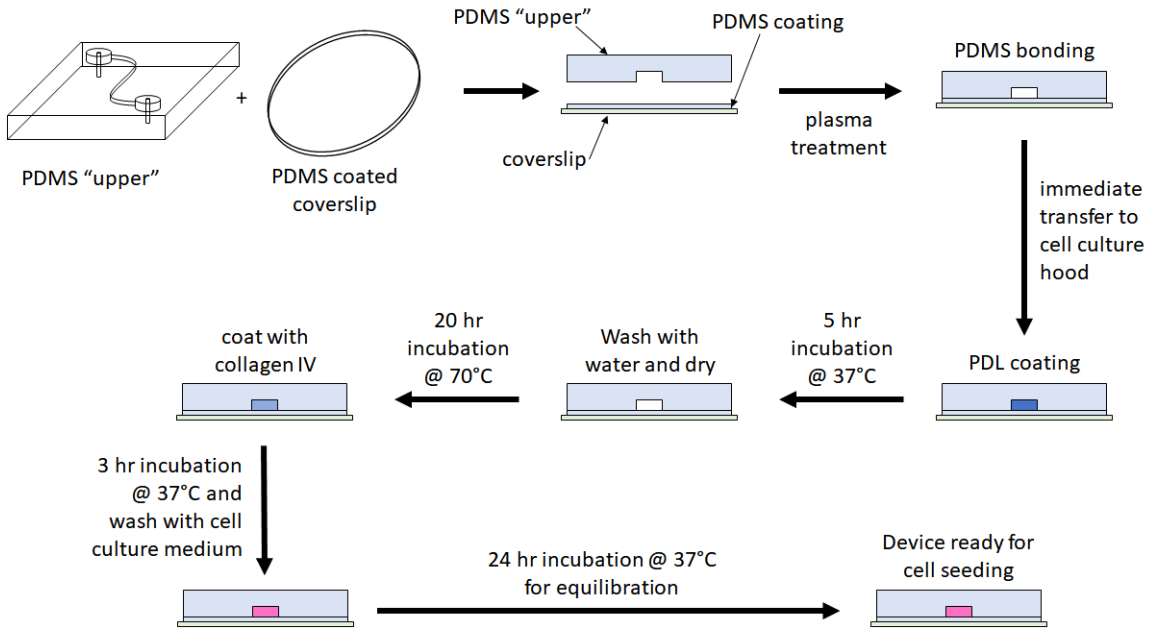

Figure 4.3: Assembly of PDMS microfluidic for culture of microvessels. PDMS "uppers" and PDMS coated coverslips ("bottoms") were plasma treated and bonded together. The devices were subsequently poly-D-lysine (PDL) coated while the channel walls are still hydrophilic. After washing and drying steps, the channels were coated with collagen IV. Finally, the device channels were washed with cell culture medium and equilibrated within a cell culture incubator.

4.3.1.2 Coating of device channels

Immediately after plasma treatment, the bonded devices were transferred to sterile 6-well plates (Thermo Fisher Scientific, Waltham, MA, USA), and brought to a cell culture hood for device coating under sterile conditions. The plasma treatment ensured no biological contaminants were present in the device channels. A solution of poly-D-lysine (PDL, 1 mg/mL, Sigma Aldrich, St. Louis, MO, USA) was pipetted into the device to fill the channel completely and fill the inlet and outlet wells. Typically, four devices are prepared in one batch. The remaining two wells of the 6-well plate were filled with 1 mL of sterile filtered water each to prevent the PDL droplets from drying out. The plate was then transferred to the cell culture incubator for 5 hrs. The PDL coating improves cell adhesion

and adhesion of collagen to the walls of the device. After incubation, the device channels were washed several times with sterile filtered water using a pipette to remove unbound/excess PDL. After washing, all water was aspirated from the devices using a pipette and the water in the empty wells was also removed. The devices were then placed to dry in an oven at 50 ℃ for 20 hrs to restore the hydrophobicity of the device wall surfaces. Next, the device channels were coated with collagen IV (1 mg/mL, Sigma Aldrich, St. Louis, MO, USA). The collagen IV solution was pipetted to fill the entire channel and inlet and outlet wells. 1 mL of sterile filtered water was placed into the two empty plate wells and the devices transferred to the cell culture incubator for 3 hrs. The device channels were then washed several times with cell culture medium (EGM-2 for HUVEC, EGM-2MV for hCMEC/D3) to remove the excess collagen IV. The inlet and outlet wells of the devices were topped up with cell culture medium and the devices were transferred to the incubator for equilibration overnight. The devices were then ready for cell seeding. Figure 4.3 illustrates the device channel coating process.

4.3.2 Cell lines and cell culture

Primary human umbilical vein endothelial cells (HUVEC) (Lonza, Basel, Swizterland) were cultured in endothelial cell growth medium (EGM-2, Lonza, Basel, Switzerland). Cells were used at passage 4-6. The HUVECs were expanded and maintained in T-75 flasks and were kept in a humidified incubator with 5% CO_2 at 37 ℃. At each passage, some cells were frozen for long term storage. The HUVECs were trypsinized, washed, spun down and placed in a freezing mixture of 10% dimethyl sulfoxide (DMSO, Sigma Aldrich, St. Louis, MO, USA) in fetal bovine serum (FBS, Sigma Aldrich, St. Louis, MO, USA). Approximately, 10^6 cells were suspended in 800 µL of the freezing mixture. An additional 200 µL of cooled freezing mixture was combined with the cell suspension to produce a total volume of 1 mL per cryo-tube. Cell cryo-tubes were placed in a Mr. Frosty freezing container (Thermo Fisher Scientific, Waltham, MA, USA) at -80 ℃ overnight and transferred to liquid nitrogen for long term storage.

Immortalized human blood brain barrier cells (hCMEC/D3) (EMD Millipore, Burlington, MA, USA) were cultured in microvascular endothelium cell growth

medium (EGM-2MV, Lonza, Basel, Switzerland). Cells were used at passage 4-6. The hCMEC/D3 cells were expanded and maintained in T-75 flasks that were coated with calf skin collagen and were kept in a humidified incubator with 5% CO_2 at 37 ℃. The flasks were coated with a 2 mL solution containing 100 µL collagen (Sigma Aldrich, St. Louis, MO, USA) and 1.9 mL HBSS (Thermo Fisher Scientific, Waltham, MA, USA) for 1 hr in a humidified incubator kept at 37 ℃. The freezing and storage protocal for the hCMEC/D3 cells was exactly the same as the protocol used for the HUVEC cells. For both cell types, cells from confluent T-75 flasks were used for microfluidic device seeding.

4.3.3 Seeding microvessel microfluidic with cells

Simple single-channel microfluidic devices were used for the experiments described in this chapter. Confluent HUVECs from T-75 flasks were suspended in EBM-2 medium at an approximate concentration of 3×10^6 cells/µL and gently pipetted into the channel via the inlet port. The pipette tip was inserted into the inlet port and the 10 µL of cell suspension were pipetted into the channel. Seeding concentration was visually confirmed with a dissection microscope (Zeiss, Oberkochen, Germany) and 20 µL of culture medium was placed on the inlet and outlet port wells to prevent drying out of the cells in the device. The seeded devices were placed upside down in the cell culture incubator for 1 hr to allow the seeded cells to adhere to the upper channel wall. The medium in the wells was then carefully removed and seeding was repeated (using the same procedure). The inlet and outlet wells were filled again with fresh cell culture medium and the devices were placed in the cell culture incubator for 1 hr to ensure cell adherence to the bottom wall of the channels. 20 µL of fresh medium was then passed through the device channel using a pipetter 3 times to wash the channel of cells and debris that did not adhere to the walls of the device channel. The inlet and outlet wells were topped up with fresh medium and the devices were placed in the cell culture incubator for 12 hrs to allow the cells to form a confluent layer within the device. It is critical that the flow rates used during seeding are very low to ensure uniform seeding density along the length of the channel. One way to control the seeding flow rate is to rotate the pipetter screw to slowly depress the plunger

rather than pushing directly on the pipetter plunger. The seeding prodecure for hCMEC/D3 cells is identical to HUVEC procedure, except that EBM-2MV cell culture medium was used. Figure 4.4 illustrates the process of seeding cells into the device.

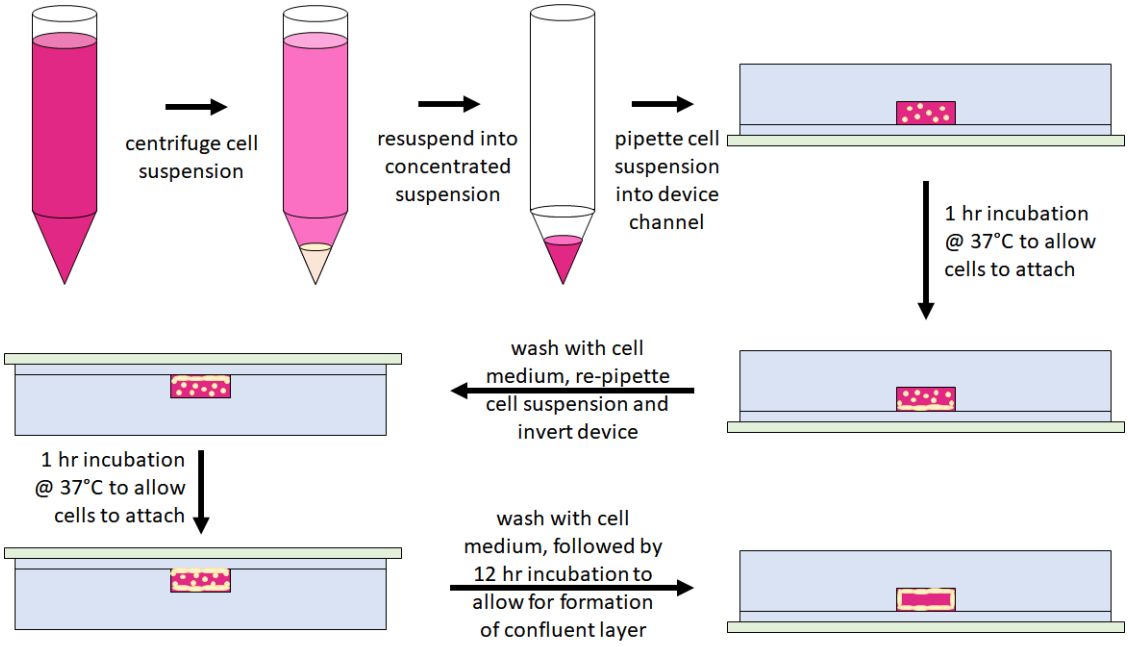

Figure 4.4: Seeding of microvessel microfluidic device channels with cells. Cells resuspended from the culture flask are centrifuged to concentrated them into a suspension suitable for seeding. Devices were seeded two times so that the upper and lower walls of the device channel would be coated with cells. After the intial attachment period, the cells continued to grow and divide within the channel forming a confluent layer along all walls of the channel. The channels are 100 µm deep and either 120 µm or 240 µm wide.

4.4 Improving microvessel fabrication repeatability

The Biointerface group has extensively used HUVECs within their microvessel microfluidic system to study the migration and spread of cancer. Although all

members of the group performing experiments with this system have been trained according to the same fabrication protocol, there has been great variability in the quality and morphology of the microvessels grown within the channels of the device. As part of my collaboration with the Biointerface group, I investigated potential sources of variability in the microvessel microfluidic fabrication protocol so that they could be addressed in future work conducted by the group. The process of fabricating the microfluidic device and growing cells within the device channels requires many steps, many of which could play an important role in the formation of healthy microvessels. After surveying members of the lab, it was apparent that individuals had modified the microfluidic assembly protocol either for convenience or for unique experimental requirements. Particularly, the most obvious differences between individuals fabricating the microfluidic devices were: 1) the duration of the ethanol soak of the PDMS device components after soft lithography, 2) the use of silicone glue to fasten inlet and outlet tubing for culture-under-flow experiments, and 3) the technique and concentration used for cell seeding. I performed a set of experiments to better understand the ultimate role of these fabrication steps on vessel performance.

4.4.1 PDMS leaching

PDMS is a widely used material for the fabrication of microfluidic devices due to its many beneficial properties. PDMS is easy to mold, gas permeable, flexible, optically transparent and can be readily bonded to glass. While PDMS structures of various designs have been successfully and extensively used for cell culture applications, the effects of PDMS exposure on cell function are not as well characterized [86]. PDMS structures are fabricated by chemically crosslinking dimethylsiloxane oligomers. The PDMS crosslinking reaction is time and temperature dependent and never goes to completion. As much as 5% of the PDMS bulk material may remain uncrosslinked after curing [86]. The crosslinked PDMS bulk is porous and hydrophobic. The smaller hydrophobic oligomer molecules reside in the pores of the crosslinked material and can then leach out into the solutions within microfluidic channels over time. One way to reduce the amount of uncrosslinked oligomers in the PDMS bulk material is to wash the crosslinked

PDMS in an organic solvent (such as ethanol) to accelerate the leaching process [86, 87].

The effect of oligomer exposure on cell function is not well characterized, but studies have shown that primary neuron survival in PDMS devices can be significantly enhanced after removal of uncrosslinked oligomers from the PDMS bulk material via solvent washes [87]. Additionally, due to the hydrophobicity of the molecules, it has been shown that uncrosslinked oligomers can incorporate into cellular membranes [86], but the effect of this incorporation on cell viability is not well understood. In order to minimize the unknown, but potentially harmful effects of uncrosslinked reactants on cells cultured within PDMS microfluidic channels, the Biointerface group incorporates an ethanol soak step for PDMS device components prior to device assembly. However, the efficacy of this wash step had not previously been evaluated. I assessed the efficacy of the PDMS oligomer removal by fabricating PDMS microfluidic single channel devices that had either been sterilized in ethanol for 30 minutes or 24 hours. All other fabrication steps in the preparation of the devices were identical. Cell seeding of the channel devices was performed with HUVECs between passages 4-6 (cells from the same flask were used for both device groups), at a concentration of 3×10^7 cells/μL. Cells were cultured for 48 hours within the devices, and device medium was replaced every 24 hours. As shown in Figure 4.5, there are clear differences in the cellular morphology within microvessel appearance. Microvessels cultured in the devices that were ethanol sterilized for 30 min exhibited greater cell debris and cell death. The cultured HUVECs had rounder cell morphology and increased light scattering at cell boundaries. Devices that were sterilized in ethanol overnight exhibited microvessels with far less cellular debris and flatter endothelial cells, a morphology pattern more similar to healthy HUVECs cultured in polystyrene flasks. These results indicate that uncrosslinked oligomer removal from the PDMS components of the microfluidic device may improve cell viability and vessel morphology. It is important to note that hydrophobic solvents used for PDMS removal can also enter the pores in the PDMS bulk after washing, and must be removed. Ethanol was removed from the devices by drying the devices for 1 hour in an oven at 80 ℃.

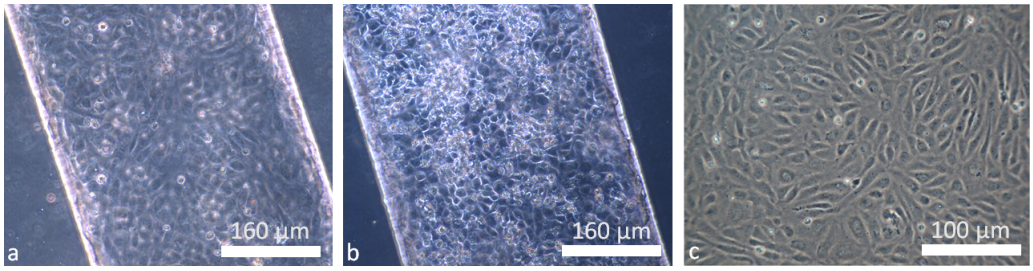

Figure 4.5: Comparison of HUVEC morphology in microvessel microfluidic devices soaked in ethanol for 30 minutes or 24 hours for uncrosslinked PDMS oligomer removal. (a) Microvessels cultured in devices washed for 24 hours exhibit healthy, confluent, flat HUVECs consistent with what is observed in HUVECs grown in polystyrene flasks. (b) Microvessels cultured in devices sterilized for 30 minutes exhibit greater cell death and cellular debris, HUVECs with more spherical morphology, and greater light scattering at intercellular boundaries. Ethanol removal of PDMS oligomers appears to improve cell viability and vessel formation in the microvessel microfluidic system. (c) Healthy HUVECs grown in a polystyrene flask.

4.4.2 Silicone adhesive for sealing tubing for device perfusion

Silicone sealant has been used by the Biointerface group (and other Cambridge research groups) to seal PDMS microfluidics to tubing and other accessories for the perfusion of culture medium. While this adhesive has been considered non-cytotoxic, our group observed variability in the morphology and quality of cells cultured in microfluidic devices that utilize this adhesive, possibly due to contamination of the cell culture medium. Silicone sealants typically consist of an inorganic siloxane polymer and appropriate filler, crosslinker, catalyst, adhesion promoter, pigment and plasticizer [88]. It is theoretically possible that any of these components that are not incorporated into the cured, crosslinked silicone polymer can leach into the culture medium. The silicone glue used for this application (Dow Corning 732, Dow Corning, United States), utilizes acetoxy chemistry to perform curing. This adhesive system is composed of a hydroxyl-terminated silicone polymer, an alkyltriacetoxysilane cross-linker, and a tin catalyst. These

components react with ambient humidity (water) to vulcanize the silicone rubber [89]. It is important to take into consideration that full curing can take several days, and that the curing reaction releases acetic acid as shown in Figure 4.6. If the silicone sealant is used to seal inlet/outlet tubing connections within the microvessel microfluidic device, and the elastomer is not completely cured, it is theoretically possible that acetic acid released from the curing reaction may contaminate the cell culture medium and negatively affect microvessel formation.

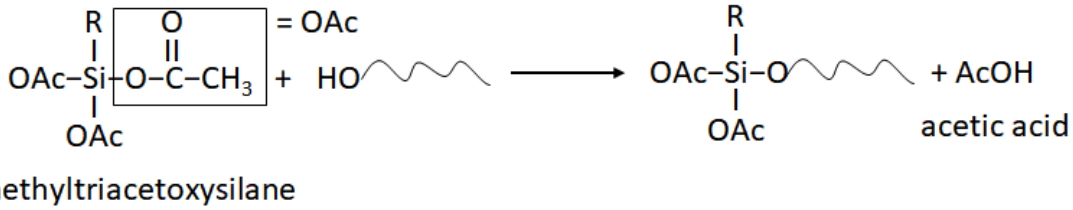

Figure 4.6: Acetoxy crosslinking mechanism for silicone adhesives. Hydroxyl-terminated silicone polymers react with alkyl-triacetoxysilane crosslinkers via a tin catalyst in a water dependent reaction releasing acetic acid.

To assess whether the use of silicone glue to affix tubing and other accessories to the microvessel microfluidic inlets and outlets could negatively impact cell culture within the devices, I fabricated two sets of single channel PDMS devices. For one set of the devices, the PDMS wells used to hold cell culture medium at the inlet and outlet were attached to the devices via plasma bonding. For the other set, the wells were attached to the devices using silicone glue. The glue was allowed to cure for 24 hours (as recommended by the manufacturer) prior to device coating and cell seeding. All other steps in the fabrication of the devices were identical. Cell seeding of the channel devices was performed with HUVECs between passages 4-6 (cells from the same flask were used for both device groups), at a concentration of 3×10^7 cells/μL. Cells were cultured for 48 hours within the devices, and device medium was replaced every 24 hours. As shown in Figure 4.7, there was no apparent difference between vessels cultured in devices that contained silicone adhesive and those that were adhesive free. Cell morphology was similar between both device groups and consistent with the

morphology of healthy HUVECs grown in polystyrene culture flasks. Although the silicone glue releases acetic acid during the curing reaction, the recommended curing time of 24 hours appears to eliminate the risk of acid contamination of the devices. As long as adequate time is allowed for the curing reaction to reach completion, silicone adhesive appears to be an acceptable bonding method for PDMS device components used for HUVEC culture.

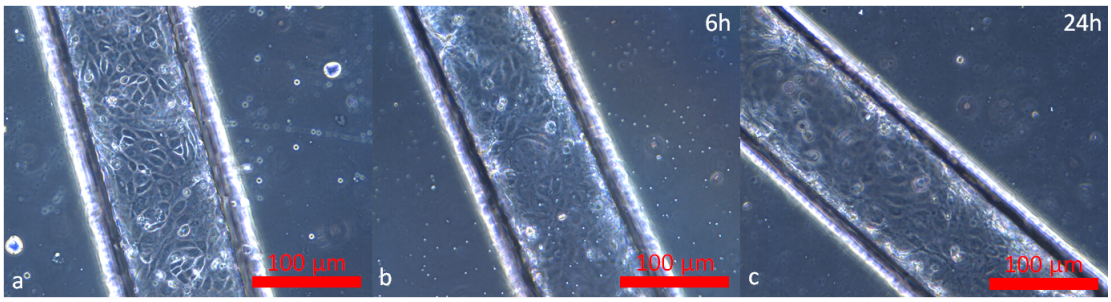

Figure 4.7: Comparison of HUVEC morphology in microvessel microfluidic devices fabricated with and without silicone adhesive. Microvessels cultured in devices with plasma bonded wells (a), have similar cellular morphology to microvessels in devices with silicone adhesive bonded wells at 6 hours post seeding (b), and 24 hours post seeding (c). Silicone adhesive, when cured properly, appears to be an acceptable sealant for PDMS microfluidics without a noticeable impact on cell viability and vessel formation in the microvessel microfluidic system.

4.4.3 Cell seeding technique

The most difficult fabrication step when culturing vessels within the microvessel microfluidic device is the seeding of the microfluidic device with suspended cells. The seeding protocol used by the Biointerface group can be summarized as follows: Cells from a confluent culture flask are suspended, and then the cell count is determined by hemocytometer. The cells are then spun down into a pellet and resuspended at the desired concentration (3×10^6 cells/mL) in cell culture medium. The cells are then manually pipetted into the channels via the inlet port. To avoid excessive shear within the device (which can damage the suspended cells), the cells are pipetted by inserting the pipette tip into the inlet port and rotating

the plunger to slowly release the cell suspension into the channel. Once the cells are placed into the channel, the devices are placed into the incubator for 1 hr and inverted to allow the seeded cells to adhere to the upper wall of the channel. Seeding is then repeated but the devices are returned to their upright position to allow cells to adhere to the lower wall of the channel. After a 1 hr incubation, the channels are washed with cell culture medium to remove unattached cells/debris. The devices are returned to the incubator to allow the cells remaining in the channel to reach confluency and form a microvessel.

Several factors in the seeding process have been previously identified to affect the quality of the generated microvessels. It is important to ensure that the cells re-suspended from the pellet are sufficiently mixed to minimize clumping, which cells are prone to do at high suspension counts. Clumped cells poorly adhere to the walls of the device channels and can obstruct the channel. These obstructions can cause a "filter" effect in which cell-free medium can flow past the obstruction while cells pile up proximally to the obstruction. The channel and inlet/outlet port shape is also very important. The original design of the inlet/outlet ports of the microvessel microfluidic device was intended to facilitate access to the microchannels via pipettes and tubing and to allow cell medium to enter the channel under laminar flow. This design, however, was not optimized for the flow of suspended cells. The large diameter of the inlet/outlet port is connected to the much narrower microchannel via a rapidly narrowing wedge shaped channel (Figure 4.1) and at this location, seeded cells often become trapped. It is recommended that in future iterations of device design that the transition from port to channel take into consideration the deposition and trapping of cells to improve seeding repeatability and reliability. Additionally, uneven deposition of cells can occur at the curved regions as cells are "pulled down" when the fluid stream follows a curve in the channel. Ensuring slow flow rates during seeding can help reduce this effect.

During seeding, cells are suspended at very high counts. At this concentration, there is not sufficient medium to support the cells for more than a few hours. It is important that after the seeding process is complete, additional medium is supplied to the cells growing within the channel. Several medium delivery methods are used to supply cells with the nutrients and growth factors necessary for

survival within the microfluidic channels. The channel can be perfused with cell culture medium via gravity driven or pump driven flow to continuously supply the channel with fresh medium. Cell medium nutrients and growth factors can alternatively be delivered into the channel via diffusion. In this case, the device is immersed in a larger volume of cell medium. As nutrients and factors are consumed by the growing cells, they are replaced via diffusion from the surrounding volume of "fresh" medium. Placing culture medium wells at the inlet and outlet is a compromise between total medium immersion and driven flow systems (Figure 4.8). The wells act to store a large volume of medium relative to the volume of medium in the channel. When the wells are filled to different heights (which can be controlled by the volume of medium applied to the wells) medium can flow within the channel driven by gravity. The well design utilizes less fluid medium than the immersion technique and is more resistant to contamination. Although gravity driven flow is possible in devices with medium wells, the rate of flow is less precise than what can be achieved by pump driven flow, and the fluid levels in the wells eventually reach equilibrium.

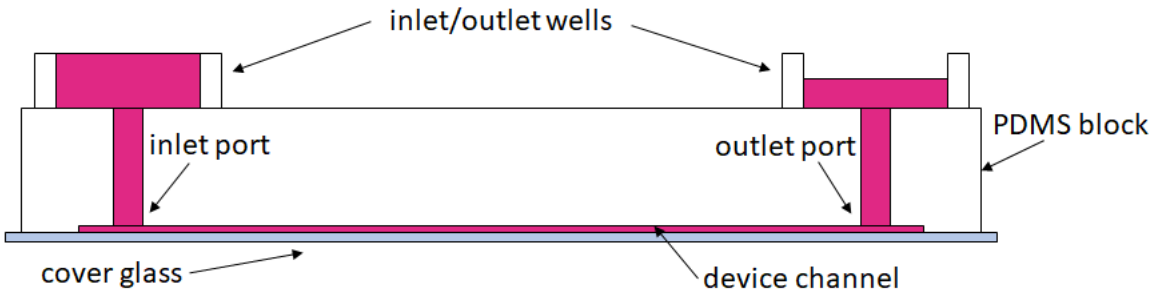

Figure 4.8: Culture medium wells at inlet and outlet of device. The wells serve to hold a relatively large volume of culture medium relative to the volume of the device channel. Nutrients and growth factors can diffuse along the channel from the well to the cells growing in the device. Creating a differential in the fluid levels within the two wells can be used to drive slow, laminar flow along the channel.

However, the means by which cell medium is supplied to the cells within the channels plays an important role in the seeding process. After cells are introduced

to the channel, they settle onto the lower surface of the channel and form physical attachments to the channel wall. The cells express adhesion molecules such as laminins and integrins that bind the collagen coated surface of the channel. Additionally, the cells can secrete ECM components into the surrounding space to further strengthen their attachment to the channel surfaces. During this time cells also form intercellular attachments such as tight junctions as the cell layer becomes confluent to form a contiguous endothelial tube (Figure 4.9). It takes several hours for the microvessels to achieve maximal structural integrity. Prior to this time, weakly attached cells and cells still in suspension can be swept out of the channel by fluid flow within the channel. This is important to note for devices prepared using pump perfusion and well medium delivery methods, as these medium supply methods may wash away or dilute the cells initially seeded within the channel, reducing the effective seeding concentration. In the medium immersion technique, there is virtually no gradient in fluid height between the inlet and outlet, so dilution is not as large a problem.

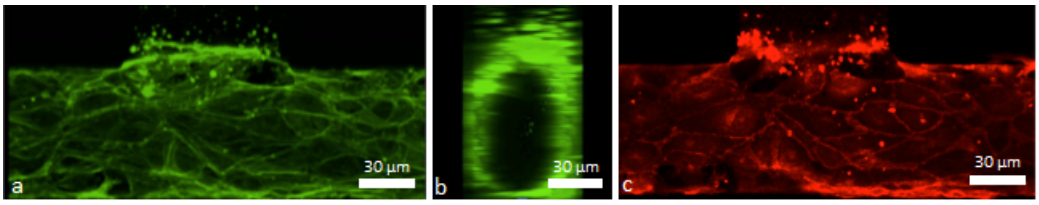

Figure 4.9: Confocal images of HUVEC microvessels cultured within the microfluidic device. (a) HUVEC cytoskeleton can be visualized by phalloidin staining of cytoskeletal F-actin. (b) Reconstructed cross-sectional image of the microvessel lumen. (c) Intercellular junctions between HUVECs in the microvessel can be visualized by VE-cadherin staining. Images provided by Magda Gerigk (Biointerface group).

The most critical factor in the formation of confluent, morphologically typical microvessels within the microfluidic device is the effective seeding density within the channel. The seeding concentration is highly important to the culturing of cells and tissues within microfluidic devices [90]. Sufficient densities of cells are required to ensure that the channel surfaces are completely covered with endothelial cells in order to promote the formation of intercellular junctions

and to rapidly form a confluent cell layer. The Biointerface group currently uses a hemocytometer to prepare a suspension of cells at the appropriate concentration (3×10^6 cells/mL) for seeding in an attempt to improve seeding consistency. Unfortunately the cell count of the seeding suspension may differ significantly from the effective seeding density within the channels due to the considerations described above. I suggest a simpler, alternate protocol for the consistent seeding of cells into the device channels.

To ensure adequate seeding, it is more important to be able to estimate the concentration of cells within the channel, and this can be performed qualitatively. A sufficiently high concentration cell suspension for seeding can be made by estimating the number of cells within a confluent flask. A confluent T-75 flask of HUVECs contains approximately 3×10^6 cells [91], which can be re-suspended in 1 mL of medium. Preparing the cell suspension this way eliminates the need to use the hemocytometer to measure the cell count. After seeding the device channel, the effective seeding concentration can be visually confirmed. As shown in Figure 4.10, an insufficient seeding concentration produces incomplete microvessels with elongated HUVECs that generally align with the channel. Ensuring a high seeding concentration ensures vessel confluence and typical cell morphology.

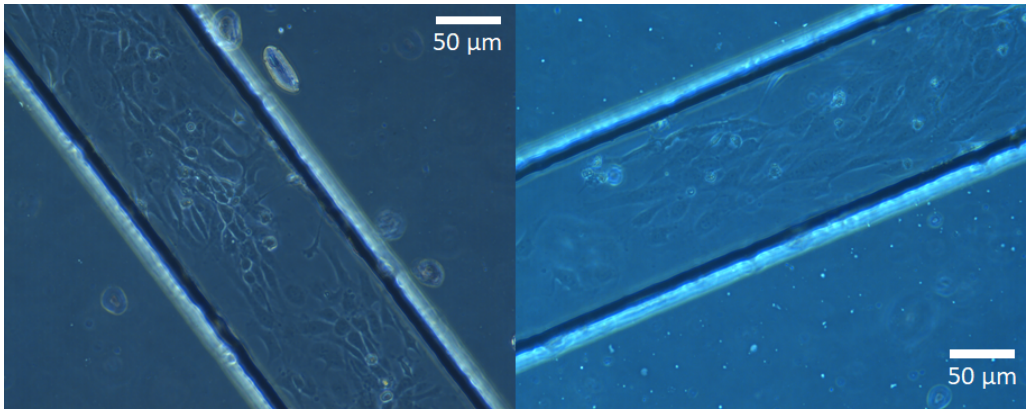

Figure 4.10: Devices seeding at 50% seeding density contain HUVECs with elongated morphology and outwardly extending processes. The cells generally appear to align along the channel.

4.5 Polarization of endothelium within the microvessel microfluidic

Cells that comprise biological interfaces, such as epithelium and endothelium, exhibit an important property known as polarity. Cell polarity refers to the asymmetric differences in shape, structure, and function of cells which enables them to carry out specialized functions [92]. In the vascular endothelium, polarization is critical to the development of a functional barrier, as this process informs the distribution of intracellular junctions and transport proteins. Endothelial cells (and epithelial cells) exhibit apical-basal polarization of their membrane. The apical membrane faces the lumen of the blood vessel, while the basolateral membrane contains the lateral membrane, where intercellular junctions are present, along with the basal membrane which forms attachments to the vascular basement membrane.

In vivo, the vascular endothelium bounds the vessel lumen and forms the interface between the blood and surrounding tissues. The apical membrane contains many membrane bound transport proteins and immunoregulatory proteins to regulate the passage of substances and cells to and from the blood. The lateral membrane contains intercellular junctions that give the endothelium mechanical strength and prevent the paracellular passage of blood contents into the surrounding tissue. The basal membrane expresses adhesion proteins, including laminins and integrins, which anchor the cells to the vascular wall.

Endothelial polarization arises via the differential localization of membrane proteins to different regions of the plasma membrane. This occurs via vesicle transport of membrane bound proteins to specific regions of the cell membrane. In many cases, cells require orientation cues from their external environment to guide the direction of polarization. Adherens junctions mechanically connect the actin cytoskeletons of adjacent cells and are the main load bearing coupling between the cells the endothelium. In endothelial cells, VE-cadherin, an adherens junction protein, plays an important role in the apical-basal polarization of endothelial cells and vascular lumen formation [93]. The microvessels cultured within the microvessel microfluidic system developed by the Biointerface group

contain endothelial cells mechanically joined by adherens junctions as shown by immunohistochemical staining of the VE-cadherin (Figure 4.9).

I sought to assess whether the endothelial tubes cultured within the microvessel microfluidic exhibit a polarization phenotype similar to what is observed *in vivo*. In particular, I attempted to determine whether the HUVEC derived microvessels express lumenal markers of polarization indicative of a vascular endothelial phenotype. Prior work from the Laboratory of Cardiac Energetics has demonstrated that AQP1 is preferentially expressed on the apical endothelium. It was hypothesized that this differential expression may explain the spatial location of the arterial water permeability barrier (although later findings described in this thesis indicate this may not be the case). Nevertheless, the apical distribution of AQP1 in the vascular endothelium is conserved across many species *in vivo*. Immunohistochemical labelling of HUVEC derived microvessels was performed to evaluate cellular polarization. As shown in Figure 4.11, HUVECs within the microfluidic devices exhibited weak staining for the apical marker podocalyxin (PODXL) distributed around the cytoplasm, possibly within vesicles. This contrasts with the reported strong apical expression of PODXL cultured in HUVEC derived vessels cultured in collagen hydrogels in a model of angiogenesis [93]. Additionally, mouse arterial endothelium exhibited strong apical labeling when stained using an equivalent staining protocol.

PODXL is a sialomucin protein that is expressed on the apical surface of vascular endothelium [94]. It is believed to act as an anti-adhesion factor on the lumenal surface of blood vessels. PODXL is an important indicator for endothelial specialization and vascular lumen formation and is believed to play a role in the localization of polarization complexes at the lumenal end of the endothelial cell [93]. The relatively poor expression of PODXL in the HUVECs cultured within the microfluidic may indicate poorer specialization from cells cultured within the microchannels. It is also possible, however that the poor staining resulted from an insufficient culture period. The expression of PODXL in the HUVEC culture can take up to seven days or more [93, 95]. The microvessels grown within the PDMS microvessel microfluidic were only cultured for 48 hours prior to PODXL staining and imaging. It is possible that a longer incubation time

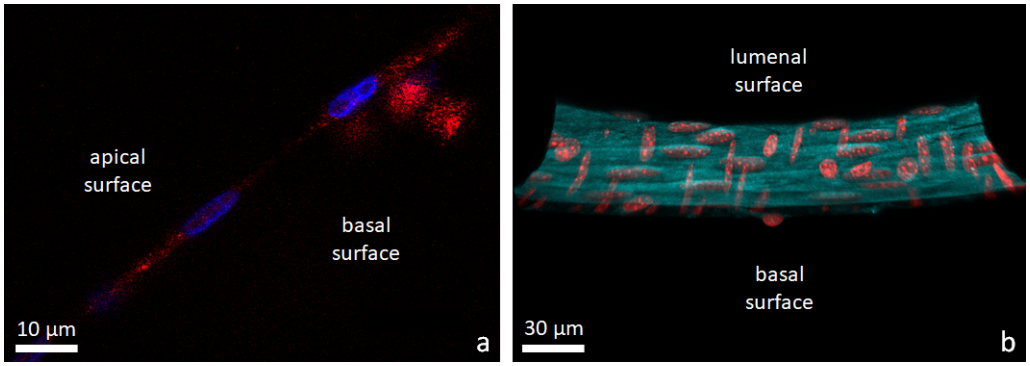

Figure 4.11: HUVEC derived microvessels from the microfluidic device show weak nonspecific staining of apical glycoprotein PODXL. (a) HUVECs cultured inside the microvessel microfluidic labelled poorly for PODXL (red) without preferential distribution toward the apical membrane of the cell. Endothelial nuclei (blue) were labelled with Hoechst. (b) Reconstructed image of a mouse cerebral artery with perspective from the vessel lumen. Mouse cerebral arteries exhibit apical expression of PODXL (cyan) as compared to the endothelial nuclei (red) labelled with Hoechst.

could improve the expression of PODXL within the micovessels. Under the current culture system used by the Biointerface group, the microvessel microfluidics do not typically support healthy vessels for much longer than 2-3 days. Further device and culture protocol optimization may be required to improve the polarization of the cultured endothelium. Additionally, it is important to note that the device used to culture HUVEC microvessels did not incorporate an ECM derived hydrogel matrix. The ECM can provide biochemical information to cultured cells that can affect cell differentiation [71]. In future development of the microvessel system, screening for apical PODXL could be used as a means to evaluate vascular specialization of the HUVECs within the device and vessels grown in devices incorporating ECM hydrogels.

Staining for AQP1 on the microvessel endothelium was attempted, but was negative (Figure 4.12). This finding, however, may be due to the reduction in epitope binding after fixation. The Laboratory of Cardiac Energetics has found that antigen retrieval was necessary to label AQP1 in tissues recovered *in vivo* using a hot/boiling citrate buffer incubation step. Unfortunately it was not practically

feasible to perform this process in the microfluidic devices.

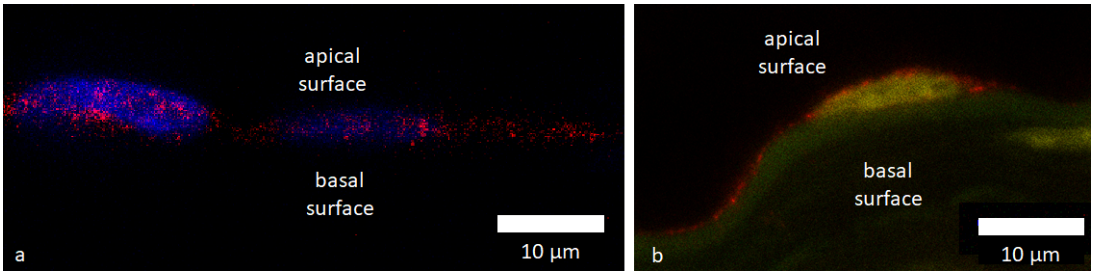

Figure 4.12: Immunohistochemical staining of the microfluidic microvessels for AQP1 was negative. (a) AQP1 labeling (red) of HUVECs within the microfluidic device was negative. Nuclei (blue) were stained with Hoechst. Antigen retrieval was not feasible for these samples. (b) AQP1 (red) staining of rat mesenteric arteries exhibit labeling at the endothelial apical membrane. Antigen retrieval was required to recover AQP1 epitopes prior to staining. Nuclei (yellow) were stained with SiR-DNA.

Chapter 5

The role of AQP1 in the location of the arterial hydroseal

5.1 Introduction

The arterial wall is a composite structure whose permeability (and impermeability) to the components of the blood is vital to the efficient delivery of oxygen and nutrients to the tissues. It is important in several disease processes including diabetes, atherosclerosis, and inflammation. Earlier studies of the arterial permeability have used destructive techniques to measure the permeability of the vascular wall when various components of the arterial wall were disrupted to assess the permeability of the remaining structure. Previous studies by the Laboratory of Cardiac Energetics have revealed that the arterial water permeability barrier is located at the basolateral surface of the endothelial cell and that the endothelial apical membrane is highly permeable to water [11]. It was also observed that the water channel protein, aquaporin 1 (AQP1), was preferentially expressed on the apical membrane of arterial endothelial cells [11]. It was hypothesized that apical distribution of AQP1 may account for the relatively increased water permeability observed at the endothelial apical membrane when compared to the endothelial basolateral membrane. This expression pattern may explain why inhibition of AQP1 does not affect arterial water permeability [96] at physiological pressures because it indicates that AQP1 is not involved in the rate-limiting barrier (hydroseal) for water transport (which is located at the basolateral membrane).

AQP1 is a member of a family of aquaporin proteins that act as water pores and are located in the membranes of renal tubular cells, red blood cells, vascular endothelium, as well as cells of the gastrointestinal tract and sweat glands. In cells that do not express aquaporins, water enters and exits the cell via osmosis through the lipid component of the cell membrane. While this mechanism allows cells to dissipate water concentration gradients between the cell interior and exterior, it does not account for the high water permeability of cell membranes of the renal tubular epithelium or red blood cells. AQP1 acts to selectively allow water molecules to pass across the plasma membrane along its concentration gradient (osmosis) with less resistance than via diffusion across the lipid cell membrane.

It was hypothesized that the basolateral location of the hydroseal protects the endothelial cells from mechanical forces caused by changes in arterial pressure. This can be analogized by considering the arterial hydroseal as a "pool liner" (Figure 5.1). A typical swimming pool is constructed from concrete, a porous, but mechanically strong material and is lined with a polymer liner that alone would be unable to support the weight of the water within the pool. The liner acts to distribute hydraulic pressure against the concrete. The arterial wall can be considered in a similar manner. The high tensile strength and porous tunica media (smooth muscle) provides support to the impermeable, but fragile tunica intima (endothelium). The basolateral location of the hydroseal allows the hydraulic pressure within the artery to be transferred directly to the tunica media without compressing the endothelial cell. Interestingly, it has been reported that AQP1 has a protective role in hypertension-augmented atherosclerosis in mice [97], an observation that potentially supports this hypothesis.

The water permeability barrier was mapped in intact arteries collected from AQP1 null mice. A total AQP1 knockout mouse model [98] developed by Dr. Alan S. Verkman's group was used to investigate the role of AQP1 in the arterial water permeability barrier. Although AQP1 is expressed by several important cell types, total knockout models for AQP1 are, remarkably, non-lethal [98]. These mice exhibit very few phenotypic differences from wild type mice other than a profound urinary concentrating defect due to impaired renal water absorption at the proximal convoluted tubule. This condition is well tolerated by the mice as long as they are provided sufficient water and their bedding is adequately changed

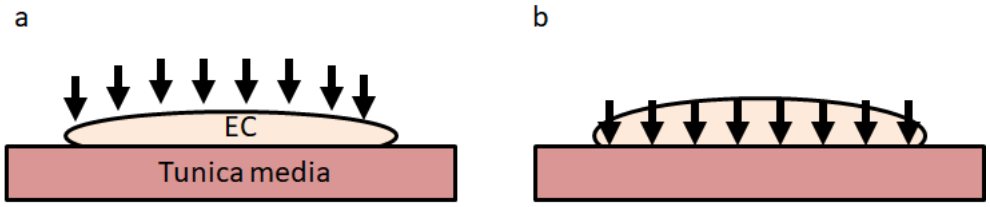

Figure 5.1: Hypothesis for basolateral location of the arterial hydroseal. (a) If the water permeability barrier was located at the apical surface, hydraulic pressure from within the artery lumen would act to compress the endothelial cells. (b) If the water permeability barrier was located at the basolateral surface, hydraulic pressure would bypass the endothelial cell and instead act directly on the mechanically robust tunica media.

to ensure hygienic conditions within the cage. CD1 mice were used as wild type control because the AQP1 null mice were generated from a CD1 background.

In this chapter, I will present experiments I conducted to evaluate the role of AQP1 in determining the water permeability of the endothelial cell membrane, and its impact on the overall arterial water permeability. Water-CARS imaging of water transport across the arterial wall was performed to observe the position of the arterial hydroseal in AQP1 knockout mice compared to wild type mice.

5.2 H_2O/D_2O transport during perfusion studies

5.2.1 Driving forces for water transport

The H_2O/D_2O perfusion experiments described in this thesis were performed to observe the steady-state transport of water across the arterial wall. The concentration profile of H_2O across the arterial wall was measured to make inferences on the relative water permeability of the various artery components. To understand the relationship between the steady state water concentration profile and the transport properties of the arterial components, it is important to understand the mechanisms of water transport relevant in this experiment: diffusion (osmosis) and convection (filtration). Diffusion of H_2O and D_2O across the arterial wall is driven by the concentration gradients of the respective species, while

convection of the H_2O/D_2O mixture is driven by the transmural pressure gradient. Because the superfusion (H_2O-PSS) and perfusion (D_2O-PSS) solutions are continuously replaced, the fluid compartments on either side of the artery wall can be considered pure. The transport driving forces during D_2O perfusion can be compared by considering the contribution to the Gibbs free energy of the convective (ΔG_f) component and the diffusional (ΔG_d) component as shown by Equations 5.1 and 5.2 [43]:

$$\Delta G_f = \overline{V}\Delta P, \tag{5.1}$$

$$\Delta G_d = RT \ln\left(\frac{x_1}{x_2}\right), \tag{5.2}$$

where $\overline{V}$ is the partial molar volume of H_2O (18 $cm^3 \cdot mol^{-1}$), ΔP is the transmural pressure gradient (70 mmHg), R is the universal gas constant, T is the temperature (298 K), x_1 is the O-H bond mole fraction in the lumen, and x_2 is the O-H bond mole fraction outside the artery. Under the experimental conditions, ΔG_f = 0.17 J/mol. The natural abundance of deuterium in water is 0.015% [99], so x_2 = 0.9997. The source of D_2O used in our experiments had a purity of 99.9%, so x_1 = 0.001. Under experimental conditions, ΔG_d = -17 kJ/mol. Based on these estimates, the driving force for diffusional water transport exceeds the driving force for filtration by five orders of magnitude!

5.2.2 Nature of the water permeability barrier

Water transport across the arterial wall is dependent on both the transport driving forces as well as the transport properties of the arterial wall materials. As evidenced by digitonin disruption experiments [11], the endothelial cell and endothelial basement membrane contribute the structures of the arterial water permeability barrier. The endothelial cell is bounded by a lipid membrane, while the basement membrane is composed of a fibrous network of collagen IV and other extracellular matrix proteins. To assess whether these structures are differentially permeable to D_2O than to H_2O, rabbit internal carotid arteries were cannulated, filled with D_2O-PSS and pressurized to ~10 mmHg by fluid column. The artery

was then mechanically isolated from the fluid column by a stopcock and was immersed in a solution of H_2O-PSS (Figure 5.2). The pressure within the artery was

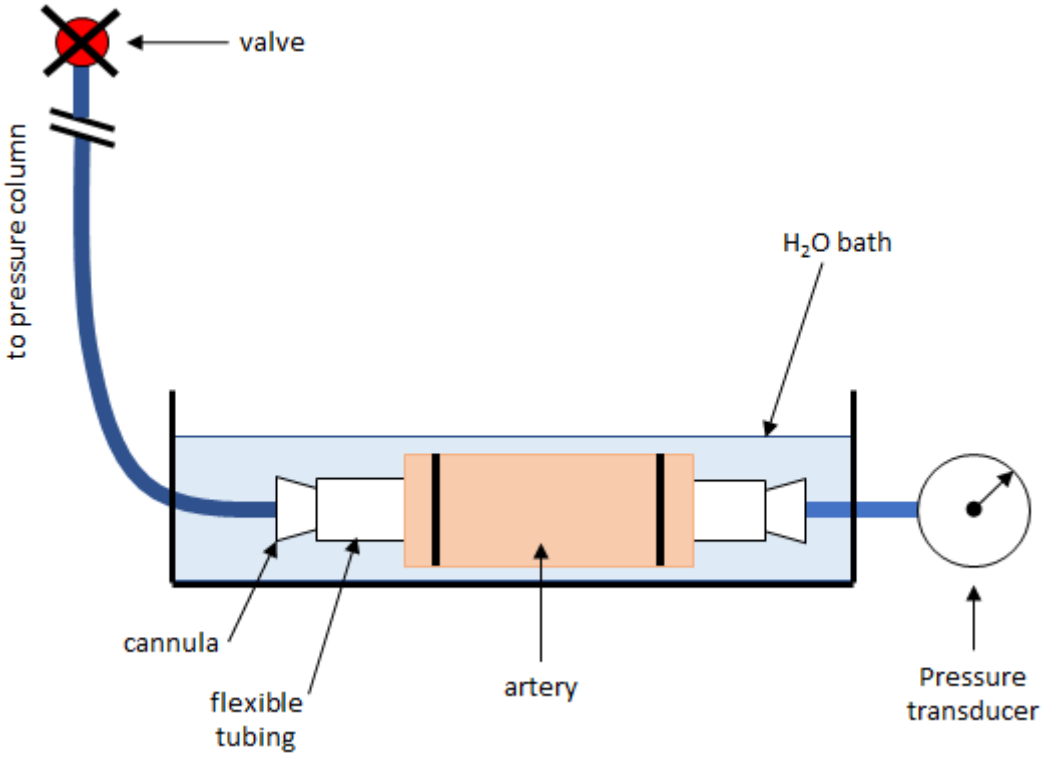

Figure 5.2: Apparatus schematic of rabbit internal carotid osmotic pressure experiment. A rabbit internal carotid artery was cannulated, pressurized with D_2O-PSS, and mechanically isolated from the fluid column via a stopcock prior to immersion in H_2O-PSS. The pressure within the artery lumen was recorded using a pressure transducer to determine the direction of fluid movement across the arterial wall.

recorded to determine the net direction of fluid flow across the arterial wall. The rise in luminal pressure shown in Figure 5.3a and the increase in artery diameter shown in Figure 5.3b demonstrate net volume inflow into the D_2O-filled artery. Similar results were obtained in n = 3 biological replicates. Luminal pressure in the control experiment exhibited a small decay consistent with net volume flow filtrating out of the artery [11].

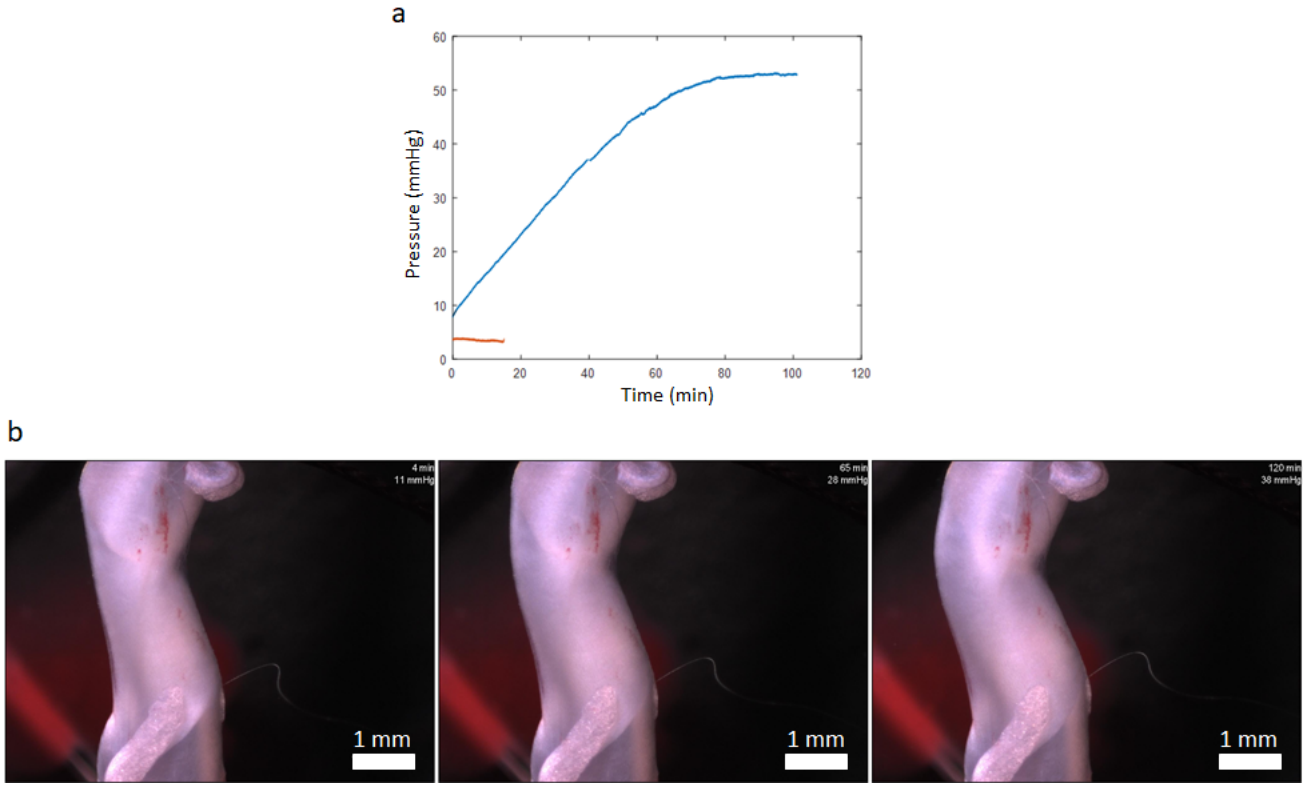

Figure 5.3: Rabbit internal carotid artery after filling with D_2O-PSS and immersion in H_2O-PSS. (a) Luminal pressure trace of the artery after loading with D_2O (blue) or H_2O (orange) and immersion in H_2O. The artery was uncoupled from the fluid column at t = 0 min by closing of a stopcock and the luminal pressure was recorded via a pressure transducer. During D_2O loading, the luminal pressure rose, indicating H_2O inflow exceeded D_2O outflow due to the increased permeability of the artery wall to H_2O than to D_2O. In the H_2O loaded artery, the luminal pressure decayed slowly due to pressure driven leak. (b) Increase in D_2O loaded artery volume after immersion in H_2O. Note that the vessel in (a) and (b) are not the same.

These results indicate that arterial water permeability to D_2O is slightly lower than to H_2O and this difference in permeability induces an osmotically generated pressure gradient. The permeability difference can likely be explained by the 20% difference between the self diffusion coefficients of water and heavy water [100], as a similar discrepancy has been observed between the permeability of AQP1 channels to H_2O and D_2O [65]. The diffusion and convection of water across the arterial wall are closely related [43]. The observed difference in the arterial wall permeability to H_2O and D_2O indicates a strong interaction between the water permeability barrier and the transported solution. This further suggests that the barrier could take the form of an oil (lipid) membrane in which water is poorly soluble, or a porous membrane containing pores with diameters on the same scale as the size of water molecules. In the case of both of an oil membrane or a molecular scale porous membrane, the permeability coefficients for diffusion (P_d) and convection (filtration) (P_f) have similar scale [43], and diffusion is the major water transport mechanism relevant to these studies. According to Finkelstein, the P_d and P_f for an oil membrane are equivalent because the fundamental mechanism of transport across an oil membrane (solubility-diffusion mechanism) is dependent on the solubility of the transported species within the membrane (Equation 5.3) [43].

$$P_d = P_f = \frac{D_{H_2O} K_{H_2O} \overline{V}_{H_2O}}{\delta \overline{V}_{lipid}} \tag{5.3}$$

Where D_{H_2O} is the diffusion coefficient of water within the membrane phase, K_{H_2O} is the partition coefficient of water between the membrane phase and aqueous solution, $\overline{V}_{H_2O}$ is the partial molar volume of water, δ is the membrane thickness and $\overline{V}_{lipid}$ is the partial molar volume of the membrane.

In the case of water transport across a porous membrane containing macroscopic pores ($>$ 150 Å diameter), the ratio of P_d to P_f is given by Equation 5.4 [43].

$$\frac{P_f}{P_d} = \frac{RT}{8\eta D_{H_2O} \overline{V}_{H_2O}} r^2 \tag{5.4}$$

Where R is the universal gas constant, T is the temperature (298 K), D_{H_2O} is the diffusion coefficient of water inside the pore ($2.4 \cdot 10^{-5} cm \cdot s^{-1}$) $\overline{V}_{H_2O}$ is the partial

molar volume of H_2O (18 $cm^3 \cdot mol^{-1}$), η is the dynamic viscosity of H_2O (0.89 cP) and r is the pore radius.

At room temperature, $\frac{RT}{8\eta D_{H_2O}\overline{V}_{H_2O}} = 8 \times 10^{14}$ cm^{-2}, which indicates that unless the pore sizes are very small (pore diameters the size of a few water molecules), water flow driven by small gradients in pressure can overwhelm diffusional transport of water driven by large concentration gradients since it is only at very small pore sizes that P_d approaches P_f. Interestingly, when the pore size decreases to a size in which water molecules can only arrange themselves single-file, the observed ratio between P_d and P_f becomes no longer dependent on pore diameter, but pore length [43]. This is because the translocation of one water molecule across the pore is dependent on the translocation of all the other molecules within the pore (dependent on pore length). Under this condition, the ratio P_f/P_d increases with pore length [43].

5.2.3 H_2O-CARS signal transport vs water transport

The H_2O-CARS generated signal is a measure of the concentration of O-H bonds present within the sample. While one can attribute an O-H bond to a water molecule, the motion of protons within water is not directly coupled to the motion of water. This is because water self-ionizes and forms deprotonated and protonated species. Through this process, protons can be exchanged from water molecule to water molecule, independent of the physical motion of the rest of the water molecule. Essentially the diffusion of protons and deuterons (and therefore O-H and O-D bonds) within the H_2O/D_2O mixture can occur via a separate mechanism compared to the bulk diffusion of the water molecules themselves. Can this effect confound H_2O-CARS observation of water transport?

In bulk water, protons are transferred between water molecules at a high rate via the Grotthuss mechanism due to the ionization of water [101]. The hydrogen bond networks found in bulk water make it possible for protons to jump between water molecules with ease. This facilitates a faster rate of diffusion than what would be expected from observations of other small ions in aqueous solution [102, 101, 103]. The Grotthuss mechanism is illustrated in Figure 5.4.

The Grotthuss mechanism demonstrates the important difference between proton transfer between water molecules and bulk water molecule transport. While proton diffusion is enhanced by the Grotthuss mechanism in bulk water, its effect on overall O-H bond transport is minimal within H_2O/D_2O mixtures simply due to the sheer difference in the concentration (and concentration gradients) between H_2O and D_2O (55 M) vs. protons and deuterons (10^{-7} M). Radioisotope tracer experiments to determine self diffusion coefficient have also demonstrated that the Grotthuss mechanism has negligible contribution to O-H bond motion in liquid water [104].

Water is believed to move through cell membranes via solubility-diffusion across the lipid bilayer and via aquaporin channels [36, 105]. The Grotthuss mechanism requires specific interactions between adjacent water molecules [106] and is not feasible within the lipid bilayer due to lack of hydrogen bonding. Aquaporin channels create a narrow opening that selectively allows water to enter the cell by reducing the hydrogen bond interactions between each water molecule, thereby reducing the likelihood of proton transfer between water molecules. Importantly, the channel walls may interact with the water molecules via polar amino acids to further slow down the transfer of protons. The conduction of protons has been shown to be retarded by membrane proteins acting as non-mobile buffers [107]. These types of interactions would reduce the apparent P_d of protons compared to water. It is therefore reasonable to assume H_2O-CARS observations of water transport represent bulk water molecule transport.

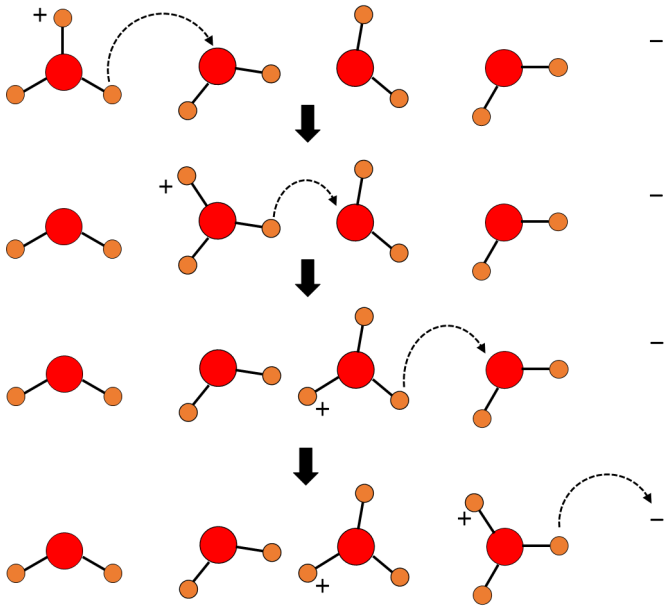

Figure 5.4: Grotthuss mechanism: the free ionization of water allows the rapid transfer of protons between water molecules.

5.3 Acquisition and confirmation of AQP1 knockout mouse model

The AQP1 knockout mouse model used in the work described in this thesis was developed by Dr. Alan Verkman's group at UCSF and used in previous studies of renal water transport in collaboration with Dr. Mark Knepper's group at NHLBI. Embryos were cyropreserved at the Jackson Laboratory for long term storage. A breeding colony was re-derived from these embryos to generate sufficient numbers of mice for our experiments.

5.3.1 Western blot

The AQP1 knockout mice were generated via targeted gene disruption [98], preventing AQP1 expression in all tissues and cell types. A western blot was performed on the mouse renal tissue to confirm that the re-derived mice lacked AQP1

(Figure 5.5). Renal tissue was used because of its relatively high expression of aquaporin proteins, and because the AQP1 null mice were total knockouts. When compared to wild type (CD1) mice, the AQP1 null mice lacked expression of AQP1. Interestingly, renal expression of the vasopressin inducible water channel AQP2 appears to be increased in the knockout, perhaps a compensatory change. This is consistent with observations made by the Verkman group [98].

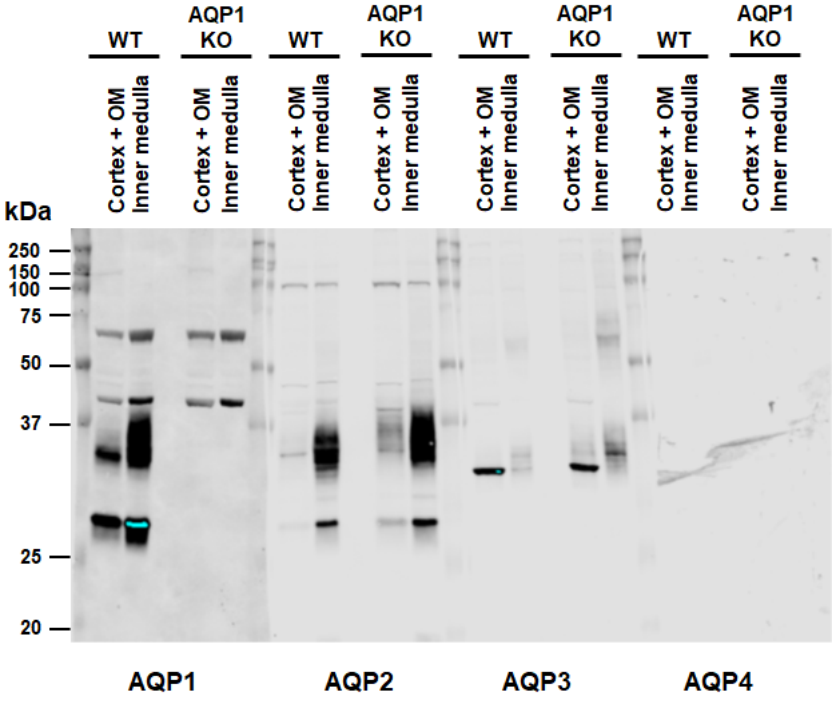

Figure 5.5: Western blot of renal tissue samples from AQP1 null (AQP1 KO) mice and CD1 wild type (WT) mice. AQP1 expression is completely suppressed in the AQP1 null mice in the renal cortex and outer medulla (OM) as well as the inner medulla (IM). AQP2 expression may be increased in the AQP1 null mice relative to the wild type. The sample loading or antibody may have been inappropriate for the AQP4 immunoblot.

5.3.2 mRNA sequencing of vascular tissues

There are 13 known aquaporin proteins in mammalian cells (AQP0-12), but the vascular endothelium is only known to primarily express AQP1. To ensure that

compensatory expression of other aquaporins was not present in the vascular endothelium, mRNA sequencing was performed to assess the gene expression of the various aquaporin proteins in the arterial endothelium of the AQP1 null mice compared to the wild type. Mesenteric arteries were dissected, cannulated on glass pipettes and washed with H_2O-PSS to remove blood cells. mRNA was extracted from the mesenteric arteries (which contain both smooth muscle and endothelial cells), transcribed to cDNA, and amplified. The cDNA libraries were purified for mRNA transcripts via poly(A) selection with magnetic beads (this step removes the abundant ribosomal RNA). The libraries were then sequenced and the reads were processed with FASTQC and aligned using STAR [108]. To assess expression of the different aquaporin genes, the total reads from each gene were compared between the AQP1 null mice and the wild type (CD1) mice (Figure 5.6). Comparisons for AQP0 and AQP10 could not be performed on the UCSC genome browser as these genes have been only very recently identified. *AQP1* gene expression was completely suppressed in the AQP1 null mice while expression was positive in the wild type mice. Expression of other aquaporin genes did not vary greatly between the knockout model and wild type, indicating that the water channel activity in the mouse vascular endothelium is functionally suppressed in the knockout. It is important to note that the mRNA expression does not always result in protein expression. Post-transcriptional events, such as RNA interference can cause a discrepancy between gene expression and protein abundance. For example, AQP2 is a vasopressin inducible aquaporin that is expressed in the renal collecting duct and the seminal vesicles. AQP2 protein expression has never been detected in the mammalian vascular endothelium or smooth muscle, although mRNA expression of the *AQP2* gene is detected in the mesenteric artery transcriptome.

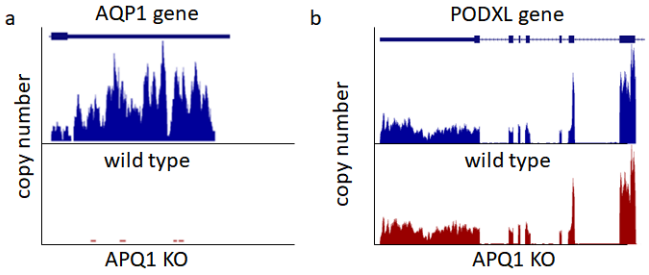

Figure 5.6: mRNA sequencing of mesenteric arteries from AQP1 null and wild type (CD1) mice confirms successful suppression of *AQP1* gene expression. (a) mRNA expression of *AQP1* was completely suppressed in the knockout mice (red) while moderately expressed in the wild type control mice. Expression of the other aquaporin genes was minimally affected by the knockout, indicating no presence of a compensatory increase in expression of the other water channels. (b) Expression of the apical endothelial protein *PODXL* remained unchanged between both the knockout and wild type mice.

5.3.3 Immunohistochemical confirmation of AQP1 knockout in vascular endothelium

Previous studies by the Laboratory of Cardiac Energetics had observed that AQP1 was apically expressed in the rat vascular endothelium [11]. In order to assess the role of AQP1 in the apical/basal location of the water permeability barrier, a mouse AQP1 knockout model was obtained. It was necessary to determine that the mouse vascular endothelium retained the same expression pattern and that the AQP1 null mouse was negative for AQP1 expression. Mouse mesenteric arteries from wild type (CD1) mice and AQP1 null mice were fixed at physiologic pressure and labeled with AQP1 antibodies. The AQP1 labeling protocol was developed in collaboration with the NHLBI Pathology Core. Antigen retrieval was necessary to restore the epitopes required for primary antibody binding after tissue fixation. Fluorescence images were acquired using stimulated emission depletion (STED) to ensure sufficient resolution to differentiate the apical and basolateral membrane of the endothelial cells. The raw AQP1 signal was quantified as follows: For each animal, three line profiles were traced across the endothelial cell nucleus and the signal at the apical and basolateral membranes

were recorded. The signal ratios were then averaged together. Figure 5.7 shows representative images from these studies. As demonstrated in the rat, the wild type mouse vascular endothelium preferentially expressed AQP1 on the apical membrane. The apical membrane to basolateral membrane AQP1 signal ratio measured from three wild type animals was 7.3 ± 1.6 (SEM). This preferential expression was completely eliminated in the AQP1 null mouse, and the minimal presence of stain was likely due to nonspecific labelling.

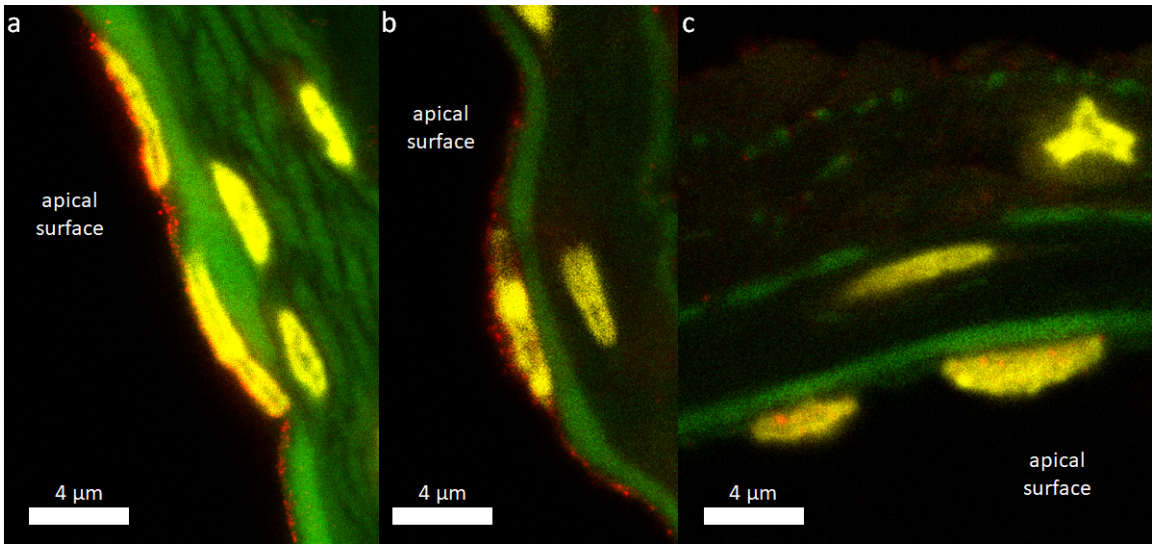

Figure 5.7: Immunohistochemical labelling of AQP1 in vascular tissues imaged with STED (red). Confocal microscopy was used to image cell nuclei (yellow) labelled with Sir-DNA and tissue autofluorescence (green). Apical expression of AQP1 in (a) rat mesenteric artery endothelial cells and in (b) wild type mouse arterial endothelial cells. (c) AQP1 null mice do not express AQP1.

5.4 Locating the arterial hydroseal in AQP1 null mice

To determine whether AQP1 is critical to the observed differential permeability of the apical and basolateral endothelial membranes, water-CARS microscopy was performed on intact pressurized mouse arteries from AQP1 null mice and wild type mice using pressure myography techniques developed in collaboration

with Professor Kim Dora's group in the Department of Pharmacology at Oxford. Third order (second branch) mesenteric arteries were initially used in this study due to their relatively straightforward dissection and isolation procedure and due to their relative lack of branches. Superior cerebellar arteries were later used in this study due to their superior optical properties and due to their role in the blood brain barrier.

5.4.1 Pressure Myography

Mouse mesenteric and superior cerebellar arteries were dissected and cannulated immediately following animal euthanasia. After dissection from the adjacent tissues, the arteries were carefully cannulated onto glass pipettes for pressure myography. Prior to performing the H_2O/D_2O perfusion studies, each artery was pressurized to a mean arterial pressure of 70 mmHg, subjected to a leak test and a vascular function test to ensure normal endothelial and smooth muscle function.

Leak testing consisted of measuring the arterial diameter prior to the perfusion experiment while the artery was connected to the fluid column by mechanically isolating the pressurized vessel from the fluid column and measuring the diameter of the artery after 1 min. If no visible change (under 25x magnification) was detected, the artery was considered to be suitable for experimentation.

Vascular function testing consisted of two parts: vasoconstriction, followed by vasodilation. In the mesenteric artery, the α_1-adrenergic receptor agonist phenylephrine was used to mediate vasoconstriction. Phenylephrine binds to α_1-adrenoreceptors on the vascular smooth muscle cell which are linked to Gq proteins that mediate smooth muscle contraction via IP_3 (Figure 5.8a). Phenylephrine mediated vasoconstriction is abrogated via the vasodilator SLIGRL. SLIGRL is a synthetic peptide that mimics the amino terminus of the PAR_2 receptor and acts as an agonist. Activation of PAR_2 receptors on the endothelial cells leads to the release of intracellular calcium which activates eNOS resulting in nitric oxide production. Nitric oxide then diffuses to the smooth muscle, activating guanylate cyclase which acts to decrease intracellular calcium leading to smooth muscle relaxation (Figure 5.8c). Since the superior cerebellar arteries of

the mouse poorly respond to phenylephrine *in vivo*, the thromboxane A_2 agonist U46619 was used to initiate vasoconstriction. U46619 acts on thromboxane receptors on the smooth muscle, simulating the production of IP_3 which results in the increase of intracellular calcium, promoting smooth muscle contraction (Figure 5.8b).

Figure 5.8: Vascular function tests were performed on all vessels with vasoactive drugs to assess the health of the vessels prior to H_2O/D_2O perfusion studies. (a) Phenylephrine binds α_1-adrenoreceptors on the vascular smooth muscle precipitating vasoconstriction. (b) U46619 binds thromboxane receptors on smooth muscle cells, promoting vasoconstriction. (c) SLIGRL stimulates the endothelial production of nitric oxide (NO) which diffuses into the adjacent vascular smooth muscle, reducing cellular contraction and promoting vasodilation.

The diameter of the cannulated artery was observed in response to measured doses of the vasoconstrictor and vasodilator. The reaction of the vessels to the vasocontrictive agents was an indicator of the health of the smooth muscle cells. The vasodilator, SLIGRL, requires normal functioning of the endothelial cells to properly act on the arteries. Figure 5.9 depicts a typical vascular function test profile of mouse mesenteric artery. When initially troubleshooting the vessel perfusion experiments, vascular function testing proved to be a highly sensitive indicator of solution contamination. Following vascular function testing, the arteries were incubated with Hoechst staining to label the endothelial cell nuclei.

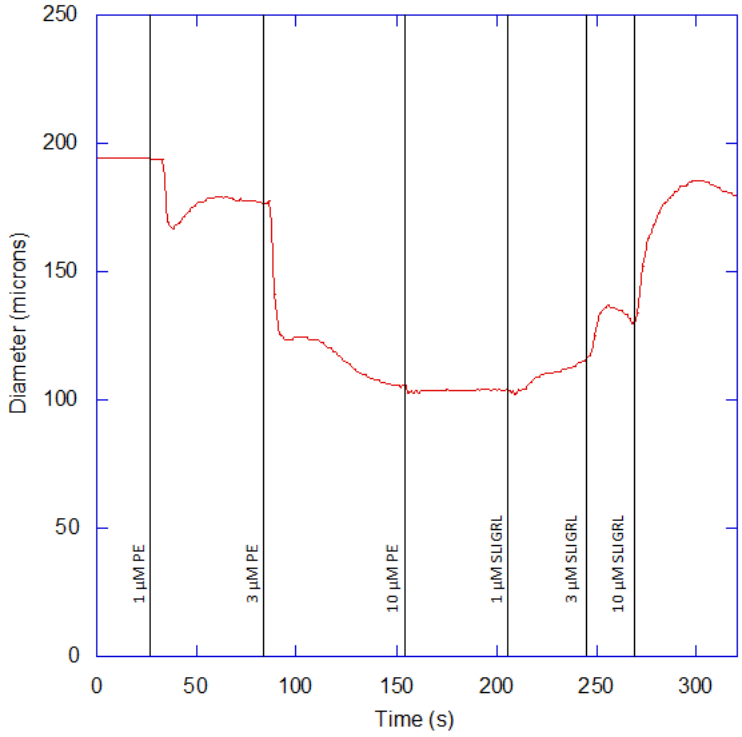

Figure 5.9: Typical vascular function test of a mouse mesenteric artery. The artery vasoconstricts in response to phenylephrine and dilates in response to SLIGRL.

5.4.2 H_2O/D_2O perfusion studies

Water transport across intact pressurized arteries was observed using a CARS microscope tuned at the 3205 cm^{-1}O-H stretch resonance. At this wavenumber, D_2O acts as a negative contrast to H_2O. Cross sectional water images were recorded during perfusion with H_2O-PSS and D_2O-PSS. Water transport across the arterial hydroseal was observed by imaging the transport of D_2O contrast as it leaked across the arterial wall from the lumen. The artery lumen and superfusion bath were considered infinite pools of O-D and O-H bonds, respectively, as they were continuously replaced by fresh solutions, allowing for the recording of H_2O concentration profiles at steady state. In this configuration, it is theoretically possible to estimate the relative permeability of wall components from the profile data. In this study, we aimed to understand the role of AQP1 in determining the relatively high water permeability of the endothelial apical membrane compared to the basolateral membrane. Typically these membranes are ∼0.25 μm apart, but they are more separated where the nucleus is present (∼3 μm). H_2O-CARS profiles were acquired across endothelial nuclei as the apical and basolateral membranes were most separated at these locations. Prior to D_2O-PSS perfusion, an "H_2O" reference image was acquired under H_2O-PSS perfusion. D_2O-PSS perfusion was then initiated until the luminal concentration of D_2O reached equilibrium and a "D_2O" image was acquired. The "H_2O" reference image determines the optical artifacts produced by the artery. The normalized CARS signal, I_{CARS}, was determined by dividing the "D_2O" image by the "H_2O" image. By comparing the concentration profile of H_2O across the arterial wall in relation to the structures of the wall itself (endothelial cell nuclei), the location of the hydroseal could be estimated. Figure 5.10 illustrates the apparatus used to perfuse/superfuse artery samples.

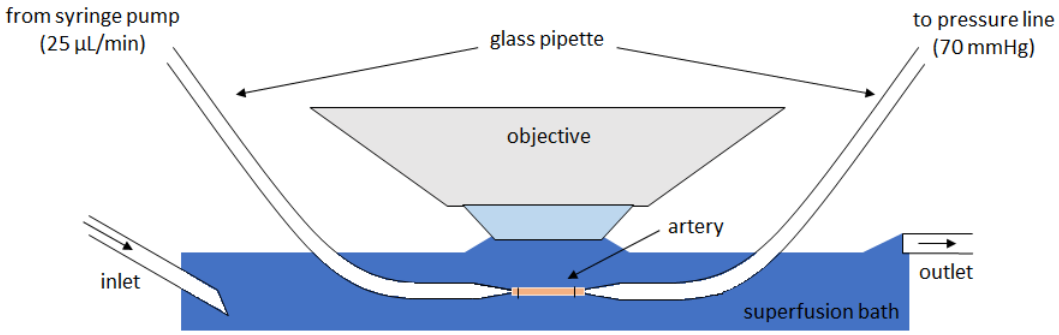

Figure 5.10: H_2O/D_2O artery perfusion apparatus. Arteries were dissected from the mouse mesentery or brain and cannulated on glass pipettes suspended in a superfusion chamber (bath). The bath fluid (H_2O-PSS) was continuously exchanged during perfusion experiments. The artery was pressurized via a fluid column and perfused using a syringe pump with H_2O-PSS and then D_2O-PSS. CARS and fluorescence images were acquired during each perfusion step. The imaging objective used the superfusion fluid as an immersion medium.

5.4.2.1 Mesenteric artery H_2O/D_2O perfusion studies

Initial H_2O/D_2O perfusion studies performed by Laboratory of Cardiac Energetics were conducted in the rat mesenteric artery [11] due to their relative accessibility and favorable size. However due to the availability of an AQP1 null mouse model, mouse mesenteric arteries were initially used. Although the mouse mesenteric arteries are considerably smaller than rat mesenteric arteries, the optical aberrations induced by the curvature of the artery wall and the smooth muscle layer were significant, requiring correction using the "H_2O" image. When perfused with D_2O-PSS, the cells from the mouse mesenteric arteries deformed strangely and appeared to develop vacuolar inclusions in their nuclear membrane (Figure 5.11). This phenomenon appeared to occur regardless of whether the mouse was wild type or AQP1 null with equal severity in both groups. Both smooth muscle cells and endothelial cells were affected, and it is currently unclear as to what causes the cells to respond this way to D_2O. This finding is in contrast to what has been observed in rat mesenteric arteries, where this type of deformation was not observed. In the future, we aim to image these membrane vacuoles using focused ion beam scanning electron microscopy (FIB-SEM), but

this could not yet be completed due to time constraints. Unfortunately, these deformations were too extreme to effectively register the "H_2O" and "D_2O" images making concentration profile analysis unfeasible with these samples.

Figure 5.11: Mouse mesenteric arteries underwent profound deformations following exposure to D_2O. (a) Hoechst labelled endothelial nucleus perfused with H_2O-PSS and (b) D_2O-PSS. Note the large vacuolar formations within the endothelial nucleus and increased intensity of the Hoechst fluorescence. H_2O-CARS image of the mouse mesenteric artery perfused with (c) H_2O-PSS and (d) D_2O-PSS. Note the optical artifacts produced by the sample.

5.4.2.2 Cerebral artery H_2O/D_2O perfusion studies

In addition to mesenteric arteries (selected for their ease of access and lack of branches), the permeability properties of cerebral vessels (vessels within the subarachnoid space) were of interest. Vessels of the CNS more tightly regulate the exchange of substances between the blood and the surrounding CNS tissue to protect the highly chemosensitive neural tissue from changes in the extracellular fluid chemical composition. While the blood brain barrier (BBB) is typically associated with cerebral capillary circulation, the arteries and veins of the CNS also possess a functional BBB of their own [34]. The superior cerebellar artery was selected for our studies due to their accessibility, reduced branching compared to other cerebral vessels and their size. The cerebellar arteries ($\sim$80 μm) are much smaller than the mesenteric arteries ($\sim$150 μm), and have a reduced wall thickness (smooth muscle layer is about 1 cell thick), and therefore have favourable optical properties. In fact, the raw H_2O-CARS images were relatively free from optical artifacts. Interestingly, the morphology of endothelial cells of the cerebral arteries differed noticeably from the endothelium of the mesenteric arteries. Cerebral endothelium contained flatter, more elongated cells compared to the mesenteric endothelium as evident from the nuclear cross sections. Additionally, mouse cerebral arteries were not affected by exposure to D_2O in the same way that the cells of the mesenteric artery were. There was minimal deformation between the "H_2O" and "D_2O" images, making image registration feasible. However, due to the relatively artifact free H_2O-CARS images obtained in the cerebral arteries and due to the minor deformations present between the "H_2O" and "D_2O" images, it was unclear whether normalizing the images would improve image profile analysis or introduce additional artifacts. As a conservative approach, profiles of the raw H_2O-CARS signal were obtained from the "D_2O" images. The location of the rise in the H_2O-CARS signal was compared to the location of the nucleus fluorescence signal. In both the wild type and AQP1 null mice, the water signal is at baseline near the apical endothelial membrane and within the nucleus, suggesting that the apical endothelial membrane is highly permeable to water in both groups (Figure 5.12). The separation between the apical nuclear signal rise and the peak of H_2O-CARS signal rise for the CD1 (wild type) mice was 2.69 ±

0.69 (SEM) μm where positive values indicate distances further from the lumen. For the AQP1 null mice, the separation was determined to be 2.49 ± 0.66 (SEM) μm indicating no significant difference between the permeability distributions of the two groups. These results demonstrate that, just as in the rat, there is an observed differential permeability between the apical region and the basolateral region of the endothelial cell in the mice. The absence of AQP1 in the arterial endothelium does not appear to decrease the permeability of the endothelial apical membrane relative to its basolateral membrane.

The fact that the AQP1 null mice have few phenotypic differences when compared to wild type animals (other than a severe urinary concentrating defect), suggests that AQP1 may not play an obligatory role in the functioning of the vascular system. The permeability distribution measurements collected via H_2O-CARS were unable to detect a relative difference in apical membrane permeability between the wild type and the AQP1 knockout. These data are consistent with AQP1 not being obligatory for the high water permeability of the apical membrane. Other water permeation pathways in the apical membrane apparently dominate this effect. This observation is consistent with the lack of a vascular phenotype in the AQP1 knockout mouse under normal conditions.

With any negative result, like that observed for water permeation in the endothelial apical membrane in the AQP1 knockout mouse, one needs to consider that the methods used were not adequate to resolve the question. The dramatic improvement in the image quality produced using the smaller mouse cerebral arteries when compared with rat mesenteric arteries [11] revealed nearly identical results with regard to the localization of the water permeability barrier to the endothelial basolateral membrane. That result coupled with the observability of the barrier's destruction using detergents [11] suggests that the CARS approach is not limited by PSF disruption. The performing of imaging at a non-perpendicular plane (to avoid excessive PSF destruction) may possibly confound the CARS measurement. Since imaging across the endothelial cells was performed at an oblique plane, the measured profiles could be blurred by the passage of the imaging PSF at an angle relative to the radial direction. Additionally, optical distortions (signal reductions) were greatest at material interfaces where, in theory, changes in

the concentration profile would occur. These issues are fundamental limitations of the experimental setup.

The mechanism explaining the difference in water permeability between the endothelial apical and basolateral regions is unknown. It has been assumed that the endothelial cell membranes present the greatest barrier to water transport, but it is difficult to optically resolve the basement membrane from the endothelial basolateral membrane. It is possible that this structure may play a role in determining the permeability of the basolateral region of the endothelial cell. Prior experiments performed by our group demonstrated that disruption of the arterial endothelium with a detergent (digitonin) increases the water permeability of the artery and increases D_2O penetrance into the artery wall [11]. However, under closer examination, digitonin stripped the artery of both the endothelial cells and the basement membrane, making assessment of the role of the basement membrane impossible. While the basement membrane is itself not likely a water permeability barrier, its association with the basolateral endothelial membrane may confer the basolateral membrane enhanced barrier properties. In future work, experiments selectively permeabilizing the endothelial cell membranes (without disruption of the basement membrane) may better determine the composition of the arterial water permeability barrier. One possible method could be to use pore forming antibiotics such as gramicidin or amphotericin B to insert water channels into the endothelial plasma membrane. Additionally, such an experiment may provide information about the role of paracellular water transport in determining arterial permeability. The location of the water permeability barrier would not change if an artery was treated with gramicidin if the primary mode of water filtration from the artery was paracellular.

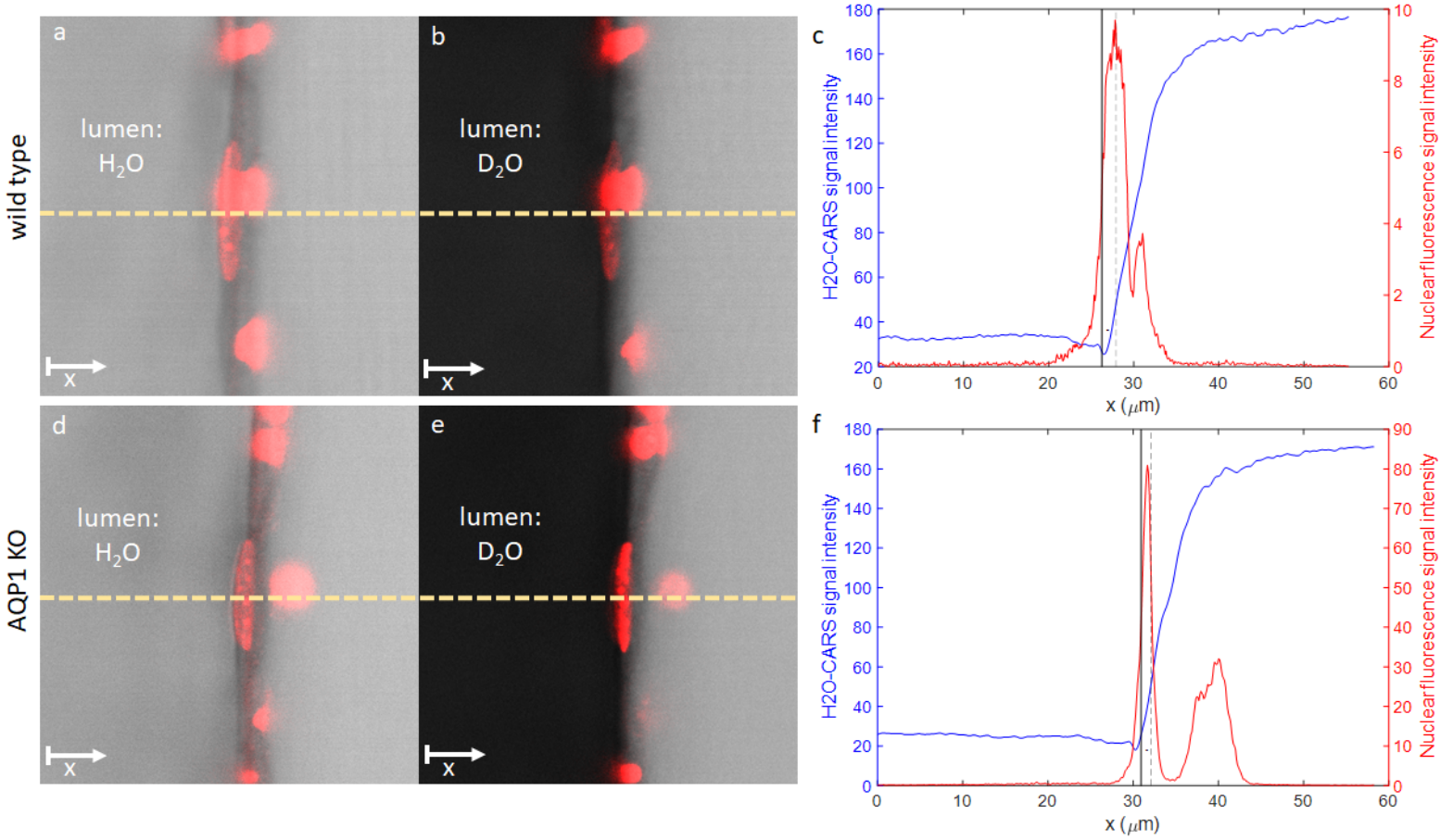

Figure 5.12: H_2O-CARS water transport imaging of the superior cerebellar artery suggests that location of water permeability barrier did not differ between the wild type mouse or the AQP1 null mice. H_2O-CARS images of a wild type superior cerebellar artery under (a) H_2O-PSS perfusion and (b) D_2O-PSS perfusion. H_2O-CARS images of a AQP1 null superior cerebellar artery under (d) H_2O-PSS perfusion and (e) D_2O-PSS perfusion. In both image sets, D_2O (black) easily equilibrates across the apical endothelial membrane and H_2O (white) concentration appears to rise at the basolateral membrane. Intensity profiles of the H_2O-CARS and nuclear signal (along the dashed yellow line) in the (c) wild type and (f) AQP1 null mice. The half maximum of the nuclear signal is marked by the solid black vertical line while the peak of the x-derivative of the H_2O-CARS intensity profile is marked by the dashed black vertical line. Results demonstrate no significant difference in the location of the water permeability barrier in wild type vs AQP1 null mice.

Chapter 6

Conclusions and future directions

6.1 Conclusions

The water permeability of biological tissues is an important property that is implicated in many disease processes. Previous studies of tissue permeability have been limited by imaging resolution or the invasiveness of the experimental technique. This thesis describes methods to observe the water transport in the microvasculature at higher than previously achieved resolution using CARS microscopy and *in vitro* and *ex vitro* experimental preparations.

In chapter 4, H_2O-CARS microscopy was used to measure the water transport properties of PEGDA hydrogels. First, CARS imaging was performed on hydrogel plugs to measure the unsteady transport of water through hydrogels of different polymer densities. The exchange of H_2O and D_2O across the hydrogel plugs was observed via H_2O-CARS imaging at a fixed point within the hydrogel plug. A finite element model of the experiment was constructed using COMSOL Multiphysics to parametrically fit the experimental data to a mathematical model and to determine the effective diffusion coefficient of each gel formulation. Then, a microfluidic device containing a multilayered PEGDA hydrogel slab was constructed to validate the use of CARS microscopy to determine the relative water permeabilities of adjacent hydrogel layers by imaging the steady-state transport of water. By imaging the concentration profile of H_2O across the hybrid hydrogel slab, it was possible to estimate the relative permeabilities of each layer by comparing the slopes of the profile within the adjacent layers.

In chapter 5, several parameters affecting the fabrication of PDMS based microvessel microfluidic culture systems were investigated. I observed that uncrosslinked PDMS oligomers present within the solid PDMS components of the device could leach out into the microfluidic culture environment and have toxic effects on the culture of HUVECs within the microfluidic channel. Removal of the PDMS oligomers by washing the PDMS device components in ethanol improved cell viability and morphology within the devices. Additionally, I determined that the use of silicone adhesives did not negatively impact the culture of endothelial cells within the PDMS devices, as long as the adhesive was given the appropriate amount of time to cure. The effect of cell seeding density on cellular morphology and vessel confluence was also investigated. A qualitative means of ensuring sufficient seeding density withing the microvessel channel is described. Finally, the polarization of HUVECs cultured within the microfluidic device was evaluated via the expression of the sialomucin protein PODXL. HUVECs within the microfluidic devices exhibited weak PODXL staining distributed around the cytoplasm, possibly within vesicles, which contrasts with other reports of PODXL expression in cultured HUVECs. It is possible more time is required for the HUVECs microvessels to reach mature PODXL expression levels and distribution.

In chapter 6, an AQP1 knockout mouse model was used to investigate the role of AQP1 on the location of the water permeability barrier within the vascular wall. The AQP1 knockout was confirmed via western blot and mRNA sequencing, and the apical endothelial expression of AQP1 within the mouse arterial endothelium was confirmed with immunohistochemistry. H_2O/D_2O perfusion of mouse cerebral arteries revealed no significant difference between the location of the water permeability barrier in the AQP1 and control animals, indicating that AQP1 is not solely responsible for the increased water permeability of the endothelial apical membrane. The mouse cerebral artery was found to be a superior model to observe water transport across the vascular wall, and generated images of far greater quality due to reduced tissue generated optical distortion.

6.2 Future directions

6.2.1 Fabrication of PEGDA microfluidics with smaller feature size

The feature size of the PEGDA microfluidics used in this thesis were limited by the resolution and precision of the UV photomasks used and the UV light source available. It was difficult to reliably produce channels of sizes much smaller than ~1 mm. Higher resolution techniques to pattern PEGDA using UV irradiation have since been developed and could be applied for this application [62]. These high resolution printing techniques in combination with the sequential crosslinking technique developed in this thesis could be used to validate water-CARS based water permeability measurement at higher resolutions for more use in high precision applications.

6.2.2 CARS imaging of the vascular permeability barrier of microvessels cultured within microfluidics

The ultimate application of the microvessel microfluidic systems being developed by the Biointerface group is to better understand the physiology of the microvasculature during cancer metastasis. A critical feature of this process is the alteration of vascular permeability at the sites of cancer extravasation/contravention. Water CARS imaging could be utilized to study the changes in the nature of the vascular water permeability barrier under both cell invasion conditions and control conditions. Additionally, CARS imaging can be performed on substances other than water by appropriately tuning the pump and Stokes lasers. In this way, the permeability of the cultured vessels to other compounds could be observed.

6.2.3 Understanding the permeability difference of the apical and basolateral endothelial membrane

The physical mechanism that explains the difference in water permeability between the endothelial apical and basolateral regions is unknown. While it is

difficult to optically resolve the basement membrane from the endothelial basolateral membrane, it has been assumed that the endothelial basolateral membranes present the greatest barrier to water transport. While the basement membrane is itself not likely a water permeability barrier, its association with the basolateral endothelial membrane may confer the basolateral membrane enhanced barrier properties. Previous experiments utilizing the detergent digitonin to disrupt the arterial endothelium demonstrated increases in the water permeability of the artery and increased D_2O penetrance into the artery wall [11]. Digitonin, however, stripped away both the endothelial cells and the basement membrane, making assessment of the role of the basement membrane impossible. Experiments selectively permeabilizing the endothelial cell membranes (without disruption of the basement membrane) may better determine the composition of the arterial water permeability barrier. The pore forming antibiotics, gramicidin and amphotericin B, could be used to insert water permeable pores into the endothelial cell membranes. If the basolateral membrane is sufficiently permeabilized by the antibiotics, the location of the permeability barrier as observed by CARS would shift in the apical direction. Such an experiment may also provide information about the role of paracellular water transport in determining arterial permeability. If the primary mode of water filtration from the artery was paracellular, the location of the water permeability barrier would not change if an artery was treated with gramicidin.

Appendix A

Additional Materials and Methods

A.1 Multimodal imaging of the H_2O/D_2O content of PEGDA hydrogels and arterial wall

Multimodal imaging of the H_2O/D_2O gradient was performed using a Leica TCS SP8 (Leica Microsystems, Wetzlar, Germany) laser scanning upright microscope and an optical setup configured for fsCARS (femtosecond CARS) and fluorescence imaging. CARS microscopy is an imaging technique that fundamentally observes the vibrations of molecular bonds at micron level resolution. In CARS microscopy, molecular bonds of interest are stimulated by the pump, Stokes, and probe beams at their resonant frequency to generate the CARS signal. The optical setup used in this work was adapted from a similar configuration used by the Laboratory of Cardiac Energetics [11]. The coherent pump, probe, and Stokes beams necessary for CARS microscopy were generated by a dual beam laser. In this work, the degenerate pump-probe beam was tuned to 780 nm, and the Stokes beam was tuned to 1040 nm so that the Raman shift = 3205 cm^{-1}as located at the O-H bond stretch vibration frequency band. This wavenumber was selected because it provides the largest CARS signal contrast between H_2O and D_2O. A 25x water immersion, 1.0 numerical aperture (NA) objective (PL IRAPO 25x/1.0 motCorr, Leica Microsystems, Wetzlar, Germany) was used for imaging done during the work discussed in this thesis. This objective corrects chromatic aberration between 700 nm and 1,300 nm which permits the pump and Stokes beams to be

focused to the same point. A dichroic mirror (FF735-Di01, Semrock, Rochester, NY, USA) was used to separate the excitation light from the emitted light from the sample. The emitted light was directed to two pairs of (four total) hybrid detectors (HyD). A second dichroic mirror (S26-DiO1, Semrock, Rochester, NY, USA) was used to split the emitted light further to each pair of HyDs. The light directed to the first pair then was passed through two IR blocking filters (FF01-720/SP and FF01-790/SP, Semrock, Rochester, NY, USA) and then further split by another dichroic (FF605-Di02, Semrock, Rochester, NY, USA). This dichroic separates the H_2O CARS signal at 624 nm from the remaining light (which was used to detect the bead fluorescence). These light paths are passed through bandpass filters (FF01-620/14 and FF01-571/72, Semrock, Rochester, NY, USA) before being sent to their corresponding HyDs. The light directed to the second pair of HyDs is further split by another dichroic (FF484-DiO1, Semrock, Rochester, NY, USA). The shorter wavelength component is passed through a bandpass filter (FF01-492/SP, Semrock, Rochester, NY, USA) before reaching a HyD (which was used to detect nuclear stain fluorescence). The longer wavelength component was passed through a bandpass filter (FF01-520/15, Semrock, Rochester, NY, USA) before reaching a HyD. Figure A.1 illustrates the light path configuration used for imaging. The motorized collar on the objective was used to correct for spherical aberration and was adjusted to maximize water CARS signal. The delay between the pump-probe beam and Stokes beam pulses was adjusted with a delay stage to maximize the CARS signal generated.

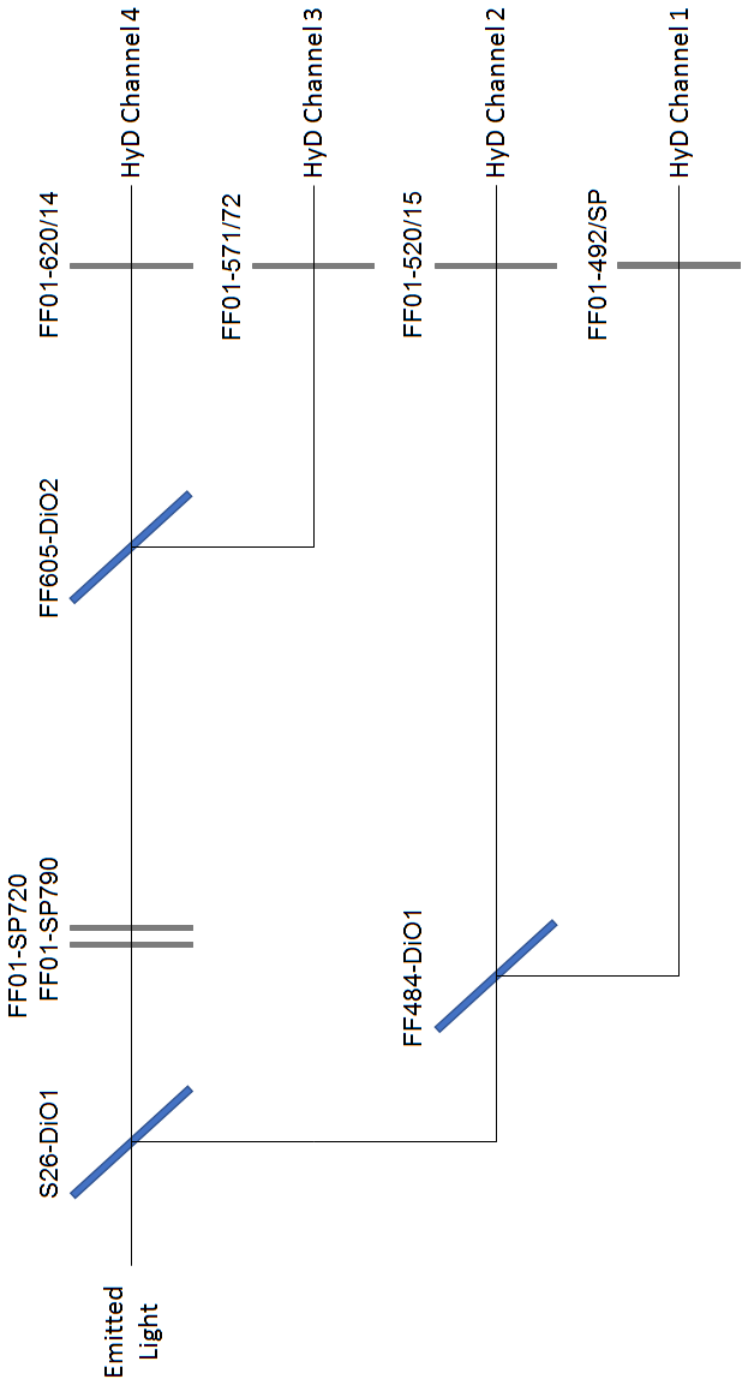

Figure A.1: Light path from sample to detectors used during multimodal imaging of water transport. Channel 1 was used to collect nuclear stain fluorescence signal in experiments where endothelial cells were visualized. Channel 2 was used to observed collagen second harmonic generation signal in experiments not described in this thesis. Channel 3 was used to capture bead fluoresence in the PEGDA hydrogel experiments. Channel 4 was used to collect CARS signal for water imaging experiments.

A.2 H_2O mole fraction quantification

H_2O-CARS imaging was performed to determine the H_2O concentration within PEGDA hydrogels and isolated perfused arteries. Specifically, the CARS microscope was tuned to resonate the O-H bonds present in the water in the sample. The raw CARS signal intensity as a function of postion, $I(r)$, is quadratically related to the probe concentration [109] and is varied by optical artifacts induced by the sample, $A(r)$. For H_2O/D_2O solutions (mixtures containing O-H and O-D bonds), the CARS signal intensity is described by Equation A.1.

$$I(r) = A(r)\left(a\left(x_{OH}(r)\right)^2 + bx_{OH}(r) + c\right) \tag{A.1}$$

Where $x_{OH}(r)$ is the O-H bond mole fraction of the mixture within the probing volume at pixel location r in the acquired image. The optical artifact term, $A(r)$, is mapped by acquiring an image, $I_{H_2O}(r)$, when the sample is immersed in H_2O only ($x_{OH}(r) = 1$). The contribution of the artifact term can be removed by normalizing $I(r)$ with respect $I_{H_2O}(r)$ as shown by Equation A.2.

$$I_{CARS}(r) = \frac{I(r)}{I_{H_2O}(r)} = \frac{\left(a\left(x_{OH}(r)\right)^2 + bx_{OH}(r) + c\right)}{(a+b+c)} \tag{A.2}$$

Determination of $I_{CARS}(r)$ requires that the experimental image, $I(r)$, must be registered with the H_2O reference image, $I_{H2O}(r)$ using fluorescence images of the arterial structures. Equation A.2 can be used to determine $x_{OH}(r)$, and therefore the H_2O mole fraction image. A calibration experiment was performed to determine the coefficients a, b, and c [11]. The coefficients were determined by performing a quadratic fit of the CARS signal observed in reference solutions containing various H_2O mole fractions (x_{OH}) as shown by Figure A.2. Due to small differences in the refractive indices of H_2O and D_2O (0.004 at 780 nm and 0.003 at 1,040 nm) [110], it is important that the immersion medium is kept from mixing with the calibration solutions due to our use of a long working-distance objective, as these differences result in significant spherical aberrations over long working distances [111]. These aberrations act to degrade the pump and Stokes beam PSFs and generate a signficant shift in focal point between the pump and Stokes beams. As a result, the CARS signal is degraded independently of the

probe concentration within the probing (focal) volume [11]. A coverslip was used to separate the immersion medium from the calibration solution. Similarly, the coverslip on the top of the PEGDA microfluidic devices prevented mixing of the immersion medium (H_2O) with the device perfusion solutions. In the artery perfusion experiments, the superfusion bath (made of H_2O-physiological salt solution) acted as the immersion fluid and was assumed pure, as it was constantly replaced by fresh H_2O-physiological salt solution during experiments. When determining the H_2O mole fraction profile across hydrogel microfluidic and artery samples, it was assumed that the optical properties of the hydrogels and tissues do not change when the samples are immersed in D_2O.

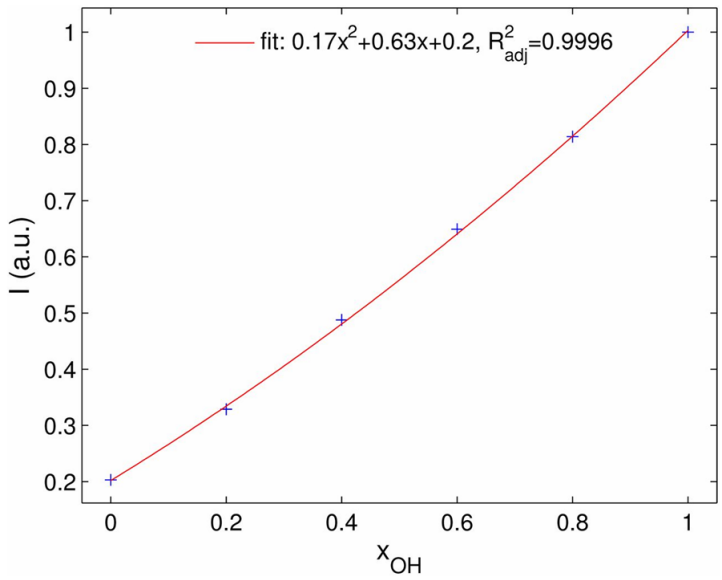

Figure A.2: Calibration of H_2O-CARS signal intensity at 3205 cm^{-1} vs H_2O mole fraction (x_{OH}) in various mixtures of H_2O/D_2O [11]

A.3 Microvessel microfluidics for the study of vascular barriers

A.3.1 Immunostaining and microscopy

Endothelial tubes cultured in the microfluidic devices were fixed with 4% paraformaldehyde (PFA, Sigma-Aldrich, St. Louis, MO, USA) for 10 mins at room temperature. The samples were subsequently washed with phophate buffered saline (PBS, Thermo Fisher Scientific, Waltham, MA, USA) to remove excess PFA and stored in PBS at 4 ℃ for immunostaining later. Immunostaining was performed to investigate the protein expression pattern of membrane proteins typically found in endothelial cells *in vivo*. The cells were permeabilized with 0.2% Triton X-100 (Sigma Aldrich, St. Louis, MO, USA) in PBS for 10 mins at room temperature. Non-specific binding of the primary antibodies were inhibited using a blocking buffer consisting of 4% bovine serum albumin (BSA, Sigma Aldrich, St. Louis, MO, USA) in PBS for 1 hr at room temperature. The cells were then incubated with the primary antibodies (Table A.1) in a solution containing 1% BSA and 5% donkey serum (Sigma Aldrich, St. Louis, MO, USA) for 1 hr at room temperature. The device channels were then washed gently with PBS to remove the unbound primary antibodies and the cells were then incubated with the desired fluorescent secondary antibodies (Table A.2) in a solution containing 5% donkey serum for 1 hr at room temperature. Cell nuclei were labelled with Hoechst 33258 (Sigma Aldrich, St. Louis, MO, USA) at 1:10^4dilution in 1% BSA in PBS for 1 hr. The labelled devices were kept from light prior to imaging (to avoid bleaching) and were stored in PBS at 4 ℃. Fluorescence imaging was performed within 48 hours of staining.

The immunostained cultured endothelial cells were imaged using a Leica TCS SP8 confocal microscope equipped with a white light laser using a 20x (NA: 0.7) and water immersion 63x (NA: 1.2) objectives (Leica Microsystems, Wetzlar, Germany) at room temperature. Images were exported as .lif files analyzed with FIJI software. Samples labelled with AlexaFluor 546 were imaged using a 520 nm excitation with a 562-590 nm detection range. Samples labelled with AlexaFluor 488 were imaged using a 488 nm excitation with a 490-540 nm detection range.

AlexaFluor 633 was imaged using a 630 nm excitation with a 650-740 nm detection range. Images for multi-labelled samples were acquired sequentially.

Target	Species	Isotype	Fluorophore	Dilution	Supplier
PODXL	Goat	Polyclonal IgG	none	1:200	R & D Systems, Minneapolis, MN, USA
AQP1	Rabbit	Polyclonal IgG	none	1:200	Abcam, Cambridge, UK
ATP1A1	Mouse	Monoclonal IgG	AlexaFluor 488	1:100	Thermo Fisher Scientific, Waltham, MA, USA

Table A.1: Primary antibodies used for protein visualization in the microvessel microfluidics

A.4 CARS imaging of the arterial water permeability barrier

A.4.1 Mouse strains

Tissues from adult male mice (8-12 weeks) were used in the experiments discussed in this thesis. CD1 (Charles River Laboratories, Wilmington, MA, USA) mice were used as control group animals (wild-type gene expression), while transgenic knockout mice deficient in the AQP1 protein were used as experimental group animals. The AQP1 null mice were generated by target gene disruption [98] and embryos were frozen for long term storage (The Jackson Laboratory, Bar Harbor, ME, USA). A homozygous breeding colony was rederived from the embryos using

Target	Species	Fluorophore	Dilution	Supplier
Goat IgG	Donkey	AlexaFluor 633	1:1,000	Thermo Fisher Scientific, Waltham, MA, USA
Rabbit IgG	Donkey	AlexaFluor 546	1:1,000	Thermo Fisher Scientific, Waltham, MA, USA

Table A.2: Secondary antibodies used for protein visualization in the microvessel microfluidics

CD1 surrogates (The Jackson Laboratory, Bar Harbor, ME, USA). In the conduct of this study, all animals were treated according to an approved animal protocol under the Animal Care and Use Committee at the National Heart Lung and Blood Institute, National Institutes of Health.

A.4.2 Confirmation of knockout

While the AQP1 null mice used in this thesis were reported as global knockouts [98], it was not known if there were compensatory changes in gene expression in the vascular tissues. A western blot and mRNA sequencing were performed to observe changes in aquaporin gene expression.

A.4.2.1 Western blot

A western blot was performed on renal tissue samples from APQ1 null mice and CD1 (wild type) mice to evaluate the expression of aquaporin proteins in the AQP1 null mouse. Samples from both animal groups were collected and prepared in an identical fashion as described below.

Protein extraction

Adult male mice (8-12 weeks) were euthanized via cervical dislocation. The peritoneal cavity was accessed via a midline abdominal incision. The mesentery was displaced to access the retroperitoneal space and the kidneys were removed and placed into ice cold physiological salt solution (PSS). The kidneys were halved along the midline sagittal place to view the renal cortex and medulla. The inner medulla was removed with fine forceps and placed into a 1 mL eppendorf tube (Eppendorf, Hamburg, Germany) containing 100 µL ice-cold 1x Laemmli buffer for solubilization. The renal cortex and outer medulla were minced and placed into a separate 1 mL eppendorf tubes containing 1 mL ice-cold 1x Laemmli buffer (Sigma-Aldrich, St. Louis, MO, USA) and homogenized with a polytron tissue homogenizer (Polytron, Montreal, Canada). Both tissue samples were then passed through a QIAshredder (QIAGEN, Hilden, Germany) to further break down tissue fragments and lyse the renal cells. Protein was measured using a bicinchoninic acid assay (BCA assay) using a Pierce BCA Protein Assay Kit (Thermo Fisher Scientific, Waltham, MA, USA).

Protein separation

Sample protein (30 µg for renal cortex, 12 µg for inner medulla) was loaded onto each lane of Criterion-TGX Precast Gels (Bio-Rad, Hercules, CA, USA) and separated using a Criterion Cell system (Bio-Rad, Hercules, CA, USA). The gel was run for 200 V for 45 min using running buffer containing 1x Tris-Glycine-SDS buffer (Bio-Rad, Hercules, CA, USA). The separated protein bands were transferred onto a nitrocellulose membrane (Life Technologies, Carlsbad, CA, USA) using a Criterion Blotter system (Bio Rad, Hercules, CA, USA) using a transfer buffer described by Fairbanks et al [112]. The electrophoretic transfer was performed at 70 V for 1 hr.

Protein detection

The blots were blocked with an Odyssey blocking buffer (LI-COR Biosciences, Lincoln, NE, USA) for 1 hr at room temperature. After blocking, the membranes were incubated with blocking buffer containing 0.1% Tween-20 (Sigma-Adrich, St.

Louis, MO, USA) and one of the primary antibodies listed in Table A.3 overnight at 4 ℃. The primary antibodies were generated by the laboratory of Dr. Mark Knepper in the NHLBI. The membranes were then washed three times for 5 minutes in PBS containing 0.1% Tween-20. The membranes were subsequently incubated with blocking buffer containing 0.1% Tween-20 and 1:5000 dilution of donkey-anti-rabbit IgG secondary antibodies conjugated to AlexaFluor 680 (711-635-152, Jackson Immuno Research, West Grove, PA, USA) for 1 hr. The blots were washed another three times for 5 minutes in PBS containing 0.1% Tween-20. The membranes were then rinsed with PBS to remove any residual Tween-20 and the membrane was scanned using an Odyssey Infrared Imaging System (LI-COR Biosciences, Lincoln, NE, USA).

Target	Species	Isotype	ID	Dilution	Stock Concentration
AQP1	rabbit	IgG	AQP1-LL266 [113]	1:5000	3 μg/μL
AQP2	rabbit	IgG	AQP2-K5007 [114]	1:5000	3 μg/μL
AQP3	rabbit	IgG	AQP3-LL178 [115]	1:500	0.5 μg/μL
AQP4	rabbit	IgG	AQP4-LL182 [116]	1:500	0.5 μg/μL

Table A.3: Primary antibodies used in aquaporin western blot. The primary antibodies were generated by and supplied from the laboratory of Dr. Mark Knepper.

A.4.2.2 mRNA sequencing of mouse vascular tissue

The mRNA of mesenteric artery tissue samples from wild type (CD1) and AQP1 null mice was sequenced to assess possible changes in transcription of aquaporin genes in the AQP1 null mice. Mice were euthanized via CO_2 asphyxiation and the mesentery was accessed via a midline abdominal incision. Bilateral pneumothorax was performed as a second assurance of death. The section of mesentery was resected and pinned out in PSS. Third order branches of the superior mesenteric artery were cleaned of fat and mounted on glass micropipettes and flushed with PSS to remove residual blood remaining in the artery. For each animal group (CD1 and AQP1 null), 3 animal replicates were used. From each animal, 3-4 arteries were dissected out from the mesentery for RNA extraction. RNA was

extracted from the mouse mesenteric arteries using TRIzol Reagent (Invitrogen, Carlsbad, CA, USA). The 3-4 dissected arteries (from the same animal) were immediately placed in 1 mL TRIzol reagent in an eppendorf tube at room temperature. The arteries were then vortexed with the Trizol reagent to mechanically disrupt the cell membranes. The TRIzol tubes containing the microdissected vessels were then stored at -80 ℃ prior to library preparation.

RNA extraction, library preparation, and RNA sequencing

The RNA extraction protocol used in this work was developed by Dr. Lihe Chen [117] of NHLBI. The RNA was extracted using the Direct-zol RNA MicroPrep kit (Zymo Research, Irvine, CA, USA) following the manufacturer's protocol and RNA integrity was assessed using an Agilent 2100 bioanalyzer with the RNA 6000 Pico Kit (gilent Technologies, Santa Clara, CA, USA). cDNA was generated by SMARTer V4 Ultra Low RNA kit (Clontech Laboratories, Mountain View, CA, USA) according to the manufacturer's protocol. 1.0 ng cDNA was fragmented and barcoded using Nextera XT DNA Sample Preparation Kit (Illumina, San Diego, CA, USA). Libraries were generated by PCR amplification, purified by AmPure XP magnetic beads, and quantified by Qubit 2.0 Fluorometer. Library size distribution was determined by Agilent 2100 bioanalyzer using the High-Sensitivity DNA kit (Agilent Technologies, Santa Clara, CA, USA). Libraries were pooled and sequenced (paired-end 50bp) on an Illumina Hiseq 3000 platfrom to an average depth of 60 million reads per sample.

Data processing and transcript abundance quantification

The data processing methodology used in this thesis was developed by Dr. Lihe Chen [117]. In summary, raw sequencing reads were analyzed by FASTQC (https://www.bioinformatics.babraham.ac.uk/projects/fastqc/) and aligned by STAR [108] to the mouse Ensembl genome (Ensembl, GRCm38.p5) with Ensembl annotation (Mus_musculus.GRCm38.83.gtf). Unique reads from genomic alignment was processed for alignment visualization on the University of California, Santa Cruz Genome Browser. Transcript abundances were quantified

using RSEM [118] in the units of transcripts per million (TPM). Unless otherwise specified, the calculations were done on the NIH Biowulf High-Performance Computing platform.

A.4.3 Physiological salt solution

A MOPS buffered solution, referred to as physiological salt solution (PSS), was used to support the dissection tissues *ex vivo*. Two formulations of PSS were used in this work, one prepared using H_2O as the solvent (H_2O-PSS), and one prepared using D_2O (D_2O-PSS). H_2O-PSS was pH adjusted to 7.40 $\pm$ 0.02 at 37 ℃. D_2O-PSS was pH adjusted to 6.99 $\pm$ 0.02 at 37 ℃ [119]. Table A.4 details the composition of the PSS. MOPS was selected as a buffering agent partly for historical and practical reasons. A bicarbonate based buffering system was not very feasible as it was unfeasible to bubble the superfusate while imaging the artery. Our collaborators in Professor Kim Dora's group (Department of Pharmacology, Oxford) historically avoided HEPES as a buffering agent due to reports of possible interference at endothelial gap junctions. However, these observed effects can take more than 8 hrs to manifest and may not occur in any significant amount in the perfusion experiments described in this thesis. Given that all the publications involving Ca^{2+} imaging from the Oxford group have always used MOPS buffer, we saw no reason not to use it. Note that the pH of all solutions was checked and adjusted to 7.40 $\pm$ 0.02 prior to use.

A.4.4 H_2O vs D_2O diffusion in rabbit internal carotid artery

Male New Zealand White rabbits (1.53–1.54 kg) were euthanized by intravenous injection of 2 mEq/kg potassium chloride while under general anesthesia with isoflurane. Rabbits were injected with 1,000 units of heparin intravenously prior to euthanasia. Rabbit internal carotid artery segments were dissected, mounted to a cannula as described by Tedgui et al [120], and immersed in H_2O-PSS bath solution. A pressure column and a pressure transducer (72-4496; Harvard Apparatus, Cambridge, MA, USA) were connected at opposite ends of the artery. The artery and the pressure column were loaded with H_2O-PSS (control) and

Reagent	Concentration (mM)
NaCl	145.0
KCl	4.7
$CaCl_2$	2.0
$MgSO_4$	1.17
MOPS	2.0
Na_2HPO_4	1.2
glucose	5.0
pyruvate	2.0
EDTA	0.02
NaOH	2.75

Table A.4: Physiological salt solution composition

then with D_2O-PSS. For each experiment the artery was disconnected from the pressure column at t = 0 by closing of a three-way valve.

A.4.5 Artery dissection and *ex vivo* mounting

Adult male mice (8-12 weeks) were euthanized by CO_2 asphyxiation via a rodent euthanasia chamber. Death was ensured via bilateral pnuemothorax. In this work, two types of arteries were used: mesenteric arteries, and posterior cerebellar arteries. To collect mesenteric arteries, the peritoneal cavity was accessed via a midline abdominal incision. The mesentery was excised and placed into ice-cold H_2O-PSS. A section of the mesenteric arcade was spread out and pinned. Straight sections of third order arteries were cleaned from the surrounding fat and excised. To collect posterior cerebellar arteries, the mouse head was removed at the base of the skull. The cranium was cut and peeled away from the brain and then the brain was carefully removed. The brain was immediately placed into ice-cold H_2O-PSS. The brain was pinned out ventral side up and the posterior artery was cleaned and isolated by microdissection. Arteries were cannulated with heat-polished glass micropipettes (outer diameter ∼120 μm, Corning inc., Corning, NY, USA) and placed in a 2 mL superfusion chamber (Warner Instruments, Hamden, CT, USA). The chamber was mounted in a temperature-regulating heated platform (Warner

Instruments, Hamden, CT, USA). Using H_2O-PSS as the superfusion fluid, the artery was warmed to 37 ℃ and then pressurized to 70 mmHg (physiological mean arterial pressure) using a hydrostatic water column (pressure tower). The distended artery was then straightened.

A.4.6 Vascular function testing

Only mesenteric arteries that exhibited appropriate contraction to the α_1-adrenergic receptor agonist phenylephrine (PE, 1 μM, Sigma Aldrich, St. Louis, MO, USA) and fully dilated to the PAR-2 receptor agonist SLIGRL (10 μM, Sigma Aldrich, St. Louis, MO, USA) were used for experiments in this thesis. Only posterior cerebellar arteries that exhibited appropriate contraction to the thromboxane A_2 agonist U46619 (300 nM, Sigma Aldrich, St. Louis, MO, USA) and fully dilated to SLIGRL (10 μM) were used for experiments. Drugs were added to the superfusion chamber after stopping the superfusion flow. Drugs were washed out from the bath by resuming superfusion flow (2 mL/min) for 20 mins.

A.4.7 Artery perfusion for H_2O/D_2O CARS imaging

After pharmacologic confirmation of vessel function, the artery was stained with Hoechst 33258 (1 μg/mL, Sigma-Aldrich, St. Louis, MO, USA) for ∼10 mins. The Hoechst stain was added to the superfusion chamber (after stopping the superfusion flow), and subsequently washed out of the bath by resuming the superfusion flow for 20 mins. In previous studies, Syto40 (Thermo Fisher Scientific, Waltham, MA, USA) was used as a live cell nuclear stain for rat mesenteric arteries [11]. In mouse arteries (particularly the posterior cerebellar arteries), Syto40 performed inconsistently, and dye uptake time was very long (sometimes $>$ 1 hr). Hoeschst was used as a preferred stain due to its rapid uptake and stronger labelling. Nuclear signal was detected at 400-484 nm. The artery was then perfused with H_2O-PSS at 25 μL/min using a gas-tight syringe (Hamilton Co., Franklin, MA, USA) and syringe pump (BASi, West Lafayette, IN, USA), and superfused with 2 mL/min H_2O-PSS. Arterial endothelial cells were viewed in "cross section" at an imaging plane defined as the plane between the top of the artery and the

midplane of the artery. This imaging plane was selected as a compromise to ensure sufficient CARS signal while retaining sufficient resolution across the arterial wall as shown by Figure A.3. An "H_2O" reference image stack was then captured and the perfusion buffer was switched to D_2O-PSS. The concentration of D_2O in the artery lumen was allowed to stabilize and a "D_2O" image stack was captured at the same field of view. Ten 3D image stacks were collected for both the "H_2O" and "D_2O" image stacks. Images were acquired at 22 frames/s using a line-scan rate of 16 kHz, a xy pixel size of 95 nm, a z pizel size of 400 nm and a field of view of 60 μm (xy) and 25 μm (z) (Frame size: 1,024x1,024 pixels).

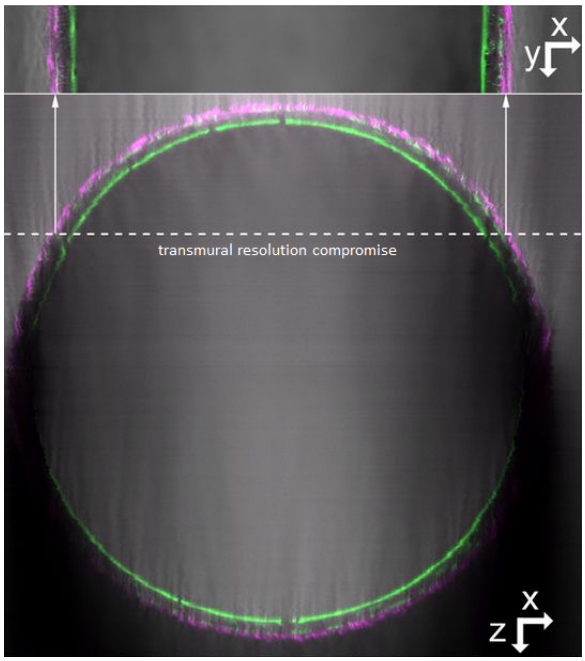

Figure A.3: Water-CARS images of axial (bottom) and longitudinal (top) cross sections of rat mesenteric artery. Elastin (green), collagen (pink), and raw water-CARS signal at 3,205 cm^{-1}(gray), are shown (adapted from [11]). Note that the water-CARS signal is degraded around the artery wall around and below the artery midplane. H_2O concentration profiles were measured along a plane located between the top and midplane of the artery to ensure adequate signal to noise ratio (SNR), and to provide sufficient optical resolution across the endothelial cells.

A.4.8 Image Analysis

The image analysis tools used in this work were adapted from those developed in MATLAB by Dr. Bertrand Lucotte at NHLBI [11]. The image analysis procedure is described briefly here: "H_2O" and "D_2O" image stacks were sequentially collected during the H_2O/D_2O perfusion experiments. First the "H_2O" and "D_2O" image stacks were registered separately (using the nucleus imaging channel) using a phase correlation registration algorithm. An average image was computed from each of the registered "H_2O" and "D_2O" image groups and then the average images were registered together. The mouse mesenteric and posterior cerebellar arteries contain relatively small amounts of collagen and elastin (materials previously used by the Laboratory of Cardiac Energetics as structural markers in the artery wall), so the endothelial cell nucleus was used as a structural marker for image registration. A Tukey window was used to register the endothelial cell nuclei by isolating the endothelial cell signal from that of the rest of the image. Initially, normalized images were computed to measure I_{CARS} and water concentration profiles in the mouse mesenteric arteries. In the case of the mouse cerebral artery samples, raw H_2O-CARS signal intensity profiles were recorded instead, due to the relatively low amount of aberrations produced by these samples and the concern that the image normalization may instead introduce additional artifacts into the profile analysis.

Line profiles were collected at three different vertical planes in proximity to the center of the endothelial cell nuclei and at three different locations across the nuclei for each plane. The line profiles were averaged over fifteen consecutive, coplanar, horizontal lines (Figure A.4). It is important that the line profiles are computed near the center region of the endothelial cell nuclei. Because the optical resolution in the vertical (z) direction is much poorer than in the horizontal direction (xy), the location of the nuclear signal peak can shift compared to the transmural signal if the line profiles are collected far way from the midplane of the nucleus. The half-maximum points of the nuclear signal intensity profile were used to delineate the location of the apical endothelial cell membrane (AECM) and the basolateral endothelial cell membrane (BECM). These points were chosen because the exact thickness of each nucleus is unknown and the signal slope at the

half-maximum points provide the minimum localization error. For each profile, the separation between the increase in H_2O signal and the AECM was estimated as the distance between the peak of the first derivative of the H_2O-CARS signal intensity profile and the half-maximum point of the nuclear signal intensity profile. The numerical H_2O-CARS signal derivative was smoothed with a moving average Gaussian filter with standard deviation of 0.17 μm. Three biological replicates (n = 3) were used for both the wild type (CD1) and AQP1 null groups.

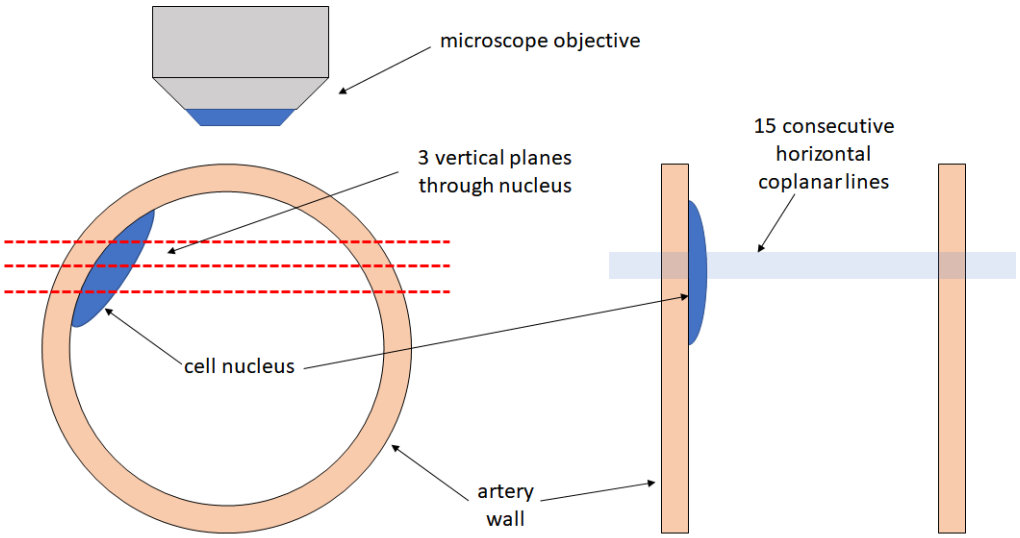

Figure A.4: Line profile collection method. H_2O-CARS signal intensity profiles line profiles were collected at three different vertical planes in proximity to the center of the endothelial cell nuclei and at three different locations across the nuclei for each plane. The line profiles were averaged over fifteen consecutive, coplanar, horizontal lines

A.4.9 AQP1 immunohistochemistry and imaging

Immunohistochemical staining was performed on cerebral and mesenteric arteries to observe the distribution of AQP1 in the endothelial cell membrane. Intact, pressurized arteries were fixed, sectioned, and stained for imaging on a confocal/STED microscope. To ensure repeatability in the staining method, the protocol was used for n = 3 replicates for both artery types.

A.4.9.1 Artery fixation

Arteries were dissected, carefully cannulated on to glass micropipettes, and heated to 37 ℃. The arteries were then gradually pressurized to 70 mmHg using H_2O-PSS as the pressure column buffer. The arteries were fixed while pressurized at ∼37 ℃ in 2% paraformaldehyde for 10 min, followed by 95% ethanol for 10 min, and then 100% ethanol for 5 min and two 10 min periods each. The artery was then removed from the pipettes, dipped in 100% ethanol, and then stored in fresh 100% ethanol (ensuring complete dehydration of the sample). The arteries were stored overnight at 4 ℃ for paraffin embedding the following day.

A.4.9.2 Immunohistochemistry

The arteries were removed from ethanol and dipped in 100% xylene for 10 min at 37 ℃ (to remove lipids) before paraffin embedding for 15 min at 65 ℃ and then for a second time for 20 min at 65 ℃ in a fresh solution of paraffin. The arteries were then sectioned and the sections were dewaxed at 65 ℃. Antigen retrieval was performed for 10 min in a citrate buffer solution at pH 6.0. The sections were placed in a blocking buffer containing 10% donkey serum (Sigma-Aldrich, St. Louis. MO, USA) for 20 min at room temperature prior to immunostaining. Primary rabbit polyclonal IgG antibodies (20333-1-AP, Protein Tech, Rosemont, IL, USA) were incubated overnight at 0.33 g/mL and 4 ℃ and then washed for 10 min. The sections were then incubated with secondary antibodies (donkey anti-rabbit IgG conjugated with Alexa Fluor 594; 711-586-152; Jackson Immuno Research, West Grove, PA, USA) for 90 min at room temperature at 1:200 dilution. Cell nuclei were labeled with SiR-DNA (Cytoskeleton Inc., Denver, CO, USA) at 1:500 dilution for 15 min at room temperature. The sections were mounted on glass slides with Prolong Gold for 24 hrs and imaged with a 1.5 coverslip. Control experiments were also performed in which the primary antibody was omitted or substituted by nonimmune rabbit IgG. This protocol was developed in prior work in rat arterial sections [11]. Sample embedding and immunohistochemical staining was performed at the NHLBI pathology core facility by Dr. Zu Xi Yu.

A.4.9.3 Imaging of AQP1 in arterial sections

STED imaging was performed to observe the AQP1 localization in the arterial endothelial cells at very high resolution. The imaging protocol was originally developed for rat arterial sections [11]. Time-gated STED images were captured using a SP8 STED 3X (Leica Microsystems, Wetzlar, Germany) equipped with a white light laser and a pulsed 775 nm STED depletion laser and with a 100x, 1.4 NA oil immersion objective (HCX PL APO STED white, Leica Microsystems, Wetzlar, Germany). Confocal and STED images were sequentially captured on arterial sections labeled for AQP1 with AlexaFluor 594 using 560 nm excitation and a detection range of 570-630 nm with gated hybrid detectors and a 775 nm STED depletion laser. The scan speed was 600 lines/s using 6 line averages, the pixel size was 28 nm, and the image size was 1024x1024 pixels. Confocal images of autofluorescent signal in arterial sections were captured using 488 nm excitation and a 490-540 nm detection range. Confocal images of the cell nuclei labelled with SiR-DNA were captured with 647 nm excitation and a 650-740 nm detection range and using z-stacks with 0.160 μm depth intervals. The images were deconvolved (classic maximum-likelihood estimation algorithm) with Huygens Professional version 15.10.1 (Scientific Volume Imaging, Hilversum, Netherlands) and viewed and reconstructed using Imaris software version 7.7.2 (Bitplane, Belfast, UK). Image deconvolution was performed at the NHLBI microscopy core facility by Dr. Daniela Malide.

References

[1] T. Ocaufa, "Normal Epidermis and Dermis with Intradermal Nevus 10x [Image]," 2015. [Online]. Available: https://commons.wikimedia.org/wiki/File:Normal_Epidermis_and_Dermis_with_Intradermal_Nevus_10x.JPG ix, 5

[2] Wbensmith, "Microvilli-Duodenum [Image]," 2007. [Online]. Available: https://commons.wikimedia.org/wiki/File:Microvilli-Duodenum.JPG ix, 5

[3] E. Uthman, "Renal_corpuscle [Image]," Licensed under the Creative Commons Attribution-Share Alike 2.0 Generic. Full terms at https://creativecommons.org/licenses/by-sa/2.0/deed.en, 2009. [Online]. Available: https://commons.wikimedia.org/wiki/File:Renal_corpuscle.jpg ix, 5

[4] M. Bonert, "Chorionic villi - intermed mag [Image]," Licensed under the Creative Commons Attribution-Share Alike 3.0 Unported. Full terms at https://creativecommons.org/licenses/by-sa/3.0/deed.en. [Online]. Available: https://commons.wikimedia.org/wiki/File:Chorionic_villi_-_intermed_mag.jpg ix, 5

[5] Genetics Home Reference, "Gallery of Illustrations in the Public Domain: NIH," Bethesda (MD), 2018. [Online]. Available: https://ghr.nlm.nih.gov/gallery ix, x, 6, 7, 8

[6] Vossman, "Aquaporin Sideview," Licensed under the Creative Commons Attribution-Share Alike 3.0 Unported. Full terms at https://creativecommons.org/licenses/by-sa/3.0/deed.en, 2009. [Online].

Available: https://commons.wikimedia.org/wiki/File:Aquaporin-Sideview.png x, 16

[7] S. Lee, X. Tong, and F. Yang, "Effects of the poly(ethylene glycol) hydrogel crosslinking mechanism on protein release." *Biomaterials science*, vol. 4, no. 3, pp. 405–11, mar 2016. [Online]. Available: http://www.ncbi.nlm.nih.gov/pubmed/26539660http://www.pubmedcentral.nih.gov/articlerender.fcgi?artid=PMC5127629 x, 26, 38

[8] Y. Wu, S. Joseph, and N. R. Aluru, "Effect of Cross-Linking on the Diffusion of Water, Ions, and Small Molecules in Hydrogels," *The Journal of Physical Chemistry B*, vol. 113, no. 11, pp. 3512–3520, mar 2009. [Online]. Available: http://pubs.acs.org/doi/abs/10.1021/jp808145x x, 25, 26

[9] S. Wang, W. Liang, Z. Dong, V. G. B. Lee, and W. J. Li, "Fabrication of Micrometer- and Nanometer-Scale Polymer Structures by Visible Light Induced Dielectrophoresis (DEP) Force," *Micromachines*, vol. 2, no. 4, pp. 431–442, dec 2011. [Online]. Available: http://www.mdpi.com/2072-666X/2/4/431 xi, 27

[10] Y. Liu, E. Gill, and Y. Y. Shery Huang, "Microfluidic on-chip biomimicry for 3D cell culture: a fit-for-purpose investigation from the end user standpoint," *Future Science OA*, p. FSO173, mar 2017. [Online]. Available: http://www.future-science.com/doi/10.4155/fsoa-2016-0084 xi, 27

[11] B. M. Lucotte, C. Powell, J. R. Knutson, C. A. Combs, D. Malide, Z.-X. Yu, M. Knepper, K. D. Patel, A. Pielach, E. Johnson, L. Borysova, K. A. Dora, and R. S. Balaban, "Direct visualization of the arterial wall water permeability barrier using CARS microscopy." *Proceedings of the National Academy of Sciences of the United States of America*, vol. 114, no. 18, pp. 4805–4810, may 2017. [Online]. Available: http://www.ncbi.nlm.nih.gov/pubmed/28373558http://www.pubmedcentral.nih.gov/articlerender.fcgi?artid=PMC5422765 xxiv, 1, 15,

20, 23, 51, 65, 66, 92, 95, 96, 104, 111, 115, 116, 121, 122, 125, 126, 135, 136, 137, 139, 140

[12] Centers for Disease Control, "Stroke Fact Sheet, Data and Statistics, DHDSP, CDC," 2016. [Online]. Available: http://www.cdc.gov/dhdsp/data_statistics/fact_sheets/fs_stroke.htm 1

[13] D. Adukauskiene, A. Bivainyte, and E. Radaviciute, "Cerebral edema and its treatment," *Medicina (Kaunas, Lithuania)*, vol. 43, no. 2, pp. 170–6, 2007. [Online]. Available: http://www.ncbi.nlm.nih.gov/pubmed/17329953 1

[14] M. Amiry-Moghaddam and O. P. Ottersen, "The molecular basis of water transport in the brain," *Nature Reviews Neuroscience*, vol. 4, no. 12, pp. 991–1001, dec 2003. [Online]. Available: http://www.nature.com/doifinder/10.1038/nrn1252 1

[15] J. E. Olson, M. Banks, R. V. W. Dimlich, and J. Evers, "Blood-Brain Barrier Water Permeability and Brain Osmolyte Content during Edema Development," *Academic Emergency Medicine*, vol. 4, no. 7, pp. 662–673, jul 1997. [Online]. Available: http://doi.wiley.com/10.1111/j.1553-2712.1997.tb03757.x 1, 11

[16] O. B. Paulson, M. M. Hertz, T. G. Bolwig, and N. A. Lassen, "Filtration and diffusion of water across the blood-brain barrier in man," *Microvascular Research*, vol. 13, no. 1, pp. 113–123, 1977. 1, 11

[17] G. A. Rosenberg, "Ischemic brain edema," *Progress in Cardiovascular Diseases*, vol. 42, no. 3, pp. 209–216, 1999. 1, 14

[18] J. Vella, C. Zammit, G. Di Giovanni, R. Muscat, and M. Valentino, "The central role of aquaporins in the pathophysiology of ischemic stroke." *Frontiers in cellular neuroscience*, vol. 9, p. 108, 2015. [Online]. Available: http://www.ncbi.nlm.nih.gov/pubmed/25904843http://www.pubmedcentral.nih.gov/articlerender.fcgi?artid=PMC4389728 1

[19] Z. Zador, S. Stiver, V. Wang, and G. T. Manley, "Role of Aquaporin-4 in Cerebral Edema and Stroke," in *Aquaporins*. Berlin, Heidelberg: Springer Berlin Heidelberg, 2009, pp. 159–170. [Online]. Available: http://link.springer.com/10.1007/978-3-540-79885-9_7 1

[20] G. T. Manley, M. Fujimura, T. Ma, N. Noshita, F. Filiz, A. W. Bollen, P. Chan, and A. Verkman, "Aquaporin-4 deletion in mice reduces brain edema after acute water intoxication and ischemic stroke," *Nature Medicine*, vol. 6, no. 2, pp. 159–163, feb 2000. [Online]. Available: http://www.nature.com/doifinder/10.1038/72256 1

[21] J. A. Nicolazzo, S. A. Charman, and W. N. Charman, "Methods to assess drug permeability across the blood-brain barrier," *Journal of Pharmacy and Pharmacology*, vol. 58, no. 3, pp. 281–293, mar 2006. [Online]. Available: http://doi.wiley.com/10.1211/jpp.58.3.0001 1

[22] L. B. Ray, "Water in the Brain," *Science Signaling*, vol. 2, no. 57, pp. ec55–ec55, feb 2009. [Online]. Available: http://stke.sciencemag.org/cgi/doi/10.1126/scisignal.257ec55 1

[23] D. G. Sherman and J. D. Easton, "Cerebral edema in stroke: a common, often fatal complication," *Postgraduate medicine*, vol. 68, no. 1, pp. 107–13, 116, 119–20, jul 1980. [Online]. Available: http://www.ncbi.nlm.nih.gov/pubmed/6771748 1

[24] H. Vernon, K. Clark, and J. P. Bressler, "In vitro models to study the blood brain barrier." *Methods in molecular biology (Clifton, N.J.)*, vol. 758, pp. 153–68, 2011. [Online]. Available: http://www.ncbi.nlm.nih.gov/pubmed/21815064 1

[25] M. R. Bullock, R. Chesnut, J. Ghajar, D. Gordon, R. Hartl, D. W. Newell, F. Servadei, B. C. Walters, and J. Wilberger, "Surgical Management of Traumatic Parenchymal Lesions," *Neurosurgery*, vol. 58, no. Supplement, pp. S2–25–S2–46, mar 2006. [Online]. Available: http://content.wkhealth.com/linkback/openurl?sid=WKPTLP:landingpage&an=00006123-200603001-00011 1

[26] M. Tennant and J. K. McGeachie, "Blood Vessel Structure and Function: A Brief Update on Recent Advances," *ANZ Journal of Surgery*, vol. 60, no. 10, pp. 747–753, oct 1990. [Online]. Available: http://doi.wiley.com/10.1111/j.1445-2197.1990.tb07468.x 6

[27] W. D. Tucker and S. S. Bhimji, *Anatomy, Blood Vessels*. StatPearls Publishing, dec 2018. [Online]. Available: http://www.ncbi.nlm.nih.gov/pubmed/29262226 6

[28] S. Jarvis, "Vascular system 1: anatomy and physiology," *Nursing Times*, vol. 114, pp. 40–44, 2018. [Online]. Available: https://www.nursingtimes.net/clinical-archive/cardiovascular/vascular-system-1-anatomy-and-physiology/7023831.article 6

[29] S. Paxton, M. Peckham, K. Adele, S. Paxton, K. Adele, and M. Peckham, "The Leeds Histology Guide," 2003. [Online]. Available: https://www.histology.leeds.ac.uk/circulatory/circ_common_str.php 7

[30] L. Claesson-Welsh, "Blood Vessels and Endothelial Cells," in *Molecular Biology of the Cell*, 4th ed., B. Alberts, A. Johnson, J. Lewis, M. Raff, K. Roberts, and P. Walter, Eds. New York: Garland Science, 2002, pp. 135–143. [Online]. Available: http://www.tandfonline.com/doi/full/10.3109/03009734.2015.1064501 7, 8

[31] ——, "Vascular permeability–the essentials." *Upsala journal of medical sciences*, vol. 120, no. 3, pp. 135–43, 2015. [Online]. Available: http://www.ncbi.nlm.nih.gov/pubmed/26220421http://www.pubmedcentral.nih.gov/articlerender.fcgi?artid=PMC4526869 8, 9, 14

[32] G. Majno, S. M. Shea, and M. Leventhal, "Endothelial contraction induced by histamine-type mediators: an electron microscopic study." *The Journal of cell biology*, vol. 42, no. 3, pp. 647–72, sep 1969. [Online]. Available: http://www.ncbi.nlm.nih.gov/pubmed/5801425http://www.pubmedcentral.nih.gov/articlerender.fcgi?artid=PMC2107712 9

[33] S. Kohn, J. A. Nagy, H. F. Dvorak, and A. M. Dvorak, "Pathways of macromolecular tracer transport across venules and small veins. Structural basis for the hyperpermeability of tumor blood vessels." *Laboratory investigation; a journal of technical methods and pathology*, vol. 67, no. 5, pp. 596–607, nov 1992. [Online]. Available: http://www.ncbi.nlm.nih.gov/pubmed/1279271 9

[34] M. J. Cipolla, "Barriers of the CNS," in *The Cerebral Circulation*. Morgan & Claypool Life Sciences, 2009. [Online]. Available: http://www.ncbi.nlm.nih.gov/pubmed/21452434 9, 10, 11, 14, 65, 67, 114

[35] T. S. Reese and M. J. Karnovsky, "Fine structural localization of a blood-brain barrier to exogenous peroxidase." *The Journal of cell biology*, vol. 34, no. 1, pp. 207–17, jul 1967. [Online]. Available: http://www.ncbi.nlm.nih.gov/pubmed/6033532http://www.pubmedcentral.nih.gov/articlerender.fcgi?artid=PMC2107213 11

[36] P. Agre, "The aquaporin water channels." *Proceedings of the American Thoracic Society*, vol. 3, no. 1, pp. 5–13, 2006. [Online]. Available: http://www.ncbi.nlm.nih.gov/pubmed/16493146http://www.pubmedcentral.nih.gov/articlerender.fcgi?artid=PMC2658677 12, 100

[37] S. Y. Yuan and R. R. Rigor, "Regulation of Endothelial Barrier Function," *Colloquium Series on Integrated Systems Physiology: From Molecule to Function*, vol. 3, no. 1, pp. 1–146, feb 2011. [Online]. Available: http://www.morganclaypool.com/doi/abs/10.4199/C00025ED1V01Y201101ISP013 13, 16, 64, 65

[38] R. Ramasamy, S. F. Yan, and A. M. Schmidt, "Receptor for AGE (RAGE): signaling mechanisms in the pathogenesis of diabetes and its complications." *Annals of the New York Academy of Sciences*, vol. 1243, pp. 88–102, dec 2011. [Online]. Available: http://www.ncbi.nlm.nih.gov/pubmed/22211895http://www.pubmedcentral.nih.gov/articlerender.fcgi?artid=PMC4501013 13

[39] S. Azzi, J. K. Hebda, and J. Gavard, "Vascular permeability and drug delivery in cancers." *Frontiers in oncology*, vol. 3, p. 211, 2013. [Online]. Available: http://www.ncbi.nlm.nih.gov/pubmed/23967403http://www.pubmedcentral.nih.gov/articlerender.fcgi?artid=PMC3744053 13

[40] M. J. Cipolla, "Anatomy and Ultrastructure," *The Cerebral Circulation*, 2009. [Online]. Available: http://www.ncbi.nlm.nih.gov/pubmed/21452434 14

[41] L. Reuss, "Water Transport Across Cell Membranes," in *eLS*. Chichester, UK: John Wiley & Sons, Ltd, jan 2012. [Online]. Available: http://doi.wiley.com/10.1002/9780470015902.a0020621.pub2 14, 15

[42] A. Finkelstein, "Water and nonelectrolyte permeability of lipid bilayer membranes." *The Journal of general physiology*, vol. 68, no. 2, pp. 127–35, aug 1976. [Online]. Available: http://www.ncbi.nlm.nih.gov/pubmed/956767http://www.pubmedcentral.nih.gov/articlerender.fcgi?artid=PMC2228420 14

[43] ——, *Water movement through lipid bilayers, pores, and plasma membranes : theory and reality*. New York: Wiley, 1987. [Online]. Available: https://books.google.com/books/about/Water_movement_through_lipid_bilayers_po.html?id=YahqAAAAMAAJ 14, 15, 95, 98, 99

[44] J. R. Pappenheimer and A. Soto-Rivera, "Effective osmotic pressure of the plasma proteins and other quantities associated with the capillary circulation in the hindlimbs of cats and dogs," *American Journal of Physiology-Legacy Content*, vol. 152, no. 3, pp. 471–491, feb 1948. [Online]. Available: http://www.physiology.org/doi/10.1152/ajplegacy.1948.152.3.471 17

[45] J. R. Pappenheimer, E. M. Renkin, and L. M. Borrero, "Filtration, Diffusion and Molecular Sieving Through Peripheral Capillary Membranes," *American Journal of Physiology-Legacy Content*, vol. 167, no. 1, pp.

13–46, sep 1951. [Online]. Available: http://www.physiology.org/doi/10.1152/ajplegacy.1951.167.1.13 17

[46] X. Lu, V. H. Huxley, and G. S. Kassab, "Endothelial barrier dysfunction in diabetic conduit arteries: a novel method to quantify filtration." *American journal of physiology. Heart and circulatory physiology*, vol. 304, no. 3, pp. H398–405, feb 2013. [Online]. Available: http://www.ncbi.nlm.nih.gov/pubmed/23220330http://www.pubmedcentral.nih.gov/articlerender.fcgi?artid=PMC4459924 17

[47] Y. Yuan, W. M. Chilian, H. J. Granger, and D. C. Zawieja, "Permeability to albumin in isolated coronary venules." *The American journal of physiology*, vol. 265, no. 2 Pt 2, pp. H543–52, aug 1993. [Online]. Available: http://www.ncbi.nlm.nih.gov/pubmed/8368358 17

[48] C. B. Vargas, F. F. Vargas, J. G. Pribyl, and P. L. Blackshear, "Hydraulic conductivity of the endothelial and outer layers of the rabbit aorta." *The American journal of physiology*, vol. 236, no. 1, pp. H53–60, jan 1979. [Online]. Available: http://www.ncbi.nlm.nih.gov/pubmed/434174 17

[49] D. Le Bihan, "Diffusion MRI: what water tells us about the brain." *EMBO molecular medicine*, vol. 6, no. 5, pp. 569–73, may 2014. [Online]. Available: http://www.ncbi.nlm.nih.gov/pubmed/24705876http://www.pubmedcentral.nih.gov/articlerender.fcgi?artid=PMC4023879 17

[50] S. Degenhartt, "An Introduction to CARS Microscopy," 2011. 18, 19, 20

[51] Y.-C. Yu, Y. Sohma, S. Takimoto, T. Miyauchi, M. Yasui, M. Baker, J. X. Cheng, C. L. Evans, X. S. Xie, C. W. Freudiger, M. Okuno, H. Kano, P. Leproux, V. Couderc, H. O. Hamaguchi, H. A. Rinia, K. N. Burger, M. Bonn, M. Muller, T. T. Le, S. Yue, J. X. Cheng, E. Potma, W. P. de Boeij, P. J. van Haastert, D. A. Wiersma, G. M. Preston, T. P. Carroll, W. B. Guggino, P. Agre, P. Agre, A. S. Verkman, M. A. Matthay, Y. Song, A. S. Verkman, K. Ibata, S. Takimoto, T. Morisaku, A. Miyawaki, M. Yasui, S. H. Madin, N. B. Darby, B. A. Stoos, A. Naray-Fejes-Toth, O. A. Carretero, S. Ito, G. Fejes-Toth, O. Kovbasnjuk, J. P. Leader, A. M.

Weinstein, K. R. Spring, M. Goel, W. G. Sinkins, C. D. Zuo, U. Hopfer, W. P. Schilling, T. Ma, A. S. Verkman, A. Frigeri, M. A. Gropper, C. W. Turck, A. S. Verkman, Y. Yukutake, M. Yasui, N. L. Nakhoul, K. S. Hering-Smith, C. T. Gambala, L. L. Hamm, S. Sandrasagra, J. E. Cuffe, E. L. Regardsoe, C. Korbmacher, V. Koefoed-Johnsen, H. H. Ussing, L. G. Palmer, O. S. Andersen, J. M. Rutkowski, M. A. Swartz, D. Akimov, A. Hoffmann, F. Tafazoli, C. Q. Zeng, M. K. Estes, K. E. Magnusson, and L. Svensson, "Direct visualization and quantitative analysis of water diffusion in complex biological tissues using CARS microscopy," *Scientific Reports*, vol. 3, pp. 261–266, sep 2013. [Online]. Available: http://www.nature.com/articles/srep02745 18, 20

[52] P. C. Cross, J. Burnham, and P. A. Leighton, "The Raman Spectrum and the Structure of Water," *Journal of the American Chemical Society*, vol. 59, no. 6, pp. 1134–1147, jun 1937. [Online]. Available: http://pubs.acs.org/doi/abs/10.1021/ja01285a052 20

[53] K. Ibata, S. Takimoto, T. Morisaku, A. Miyawaki, and M. Yasui, "Analysis of aquaporin-mediated diffusional water permeability by coherent anti-stokes Raman scattering microscopy." *Biophysical journal*, vol. 101, no. 9, pp. 2277–83, nov 2011. [Online]. Available: http://www.ncbi.nlm.nih.gov/pubmed/22067168 20

[54] A. Chaurra, B. M. Gutzman, E. Taylor, P. C. Ackroyd, and K. A. Christensen, "Lucifer Yellow as a live cell fluorescent probe for imaging water transport in subcellular organelles." *Applied spectroscopy*, vol. 65, no. 1, pp. 20–5, jan 2011. [Online]. Available: http://www.ncbi.nlm.nih.gov/pubmed/21211149 21

[55] E. O. Potma, W. P. de Boeij, P. J. M. van Haastert, and D. A. Wiersma, "Real-time visualization of intracellular hydrodynamics in single living cells," *Proceedings of the National Academy of Sciences*, vol. 98, no. 4, pp. 1577–1582, feb 2001. [Online]. Available: http://www.pnas.org/cgi/doi/10.1073/pnas.98.4.1577http://www.ncbi.nlm.nih.gov/pubmed/11171993http:

//www.pubmedcentral.nih.gov/articlerender.fcgi?artid=PMC29299http://www.pnas.org/cgi/doi/10.1073/pnas.031575698 21, 23

[56] A. Furstenberg and E. Vauthey, "Excited-state dynamics of the fluorescent probe Lucifer Yellow in liquid solutions and in heterogeneous media," *Photochemical & Photobiological Sciences*, no. 4, pp. 260–267, 2005. 21

[57] R. G. Ye and A. S. Verkman, "Simultaneous optical measurement of osmotic and diffusional water permeability in cells and liposomes." *Biochemistry*, vol. 28, no. 2, pp. 824–9, jan 1989. [Online]. Available: http://www.ncbi.nlm.nih.gov/pubmed/2540807 21

[58] H. G. Folkesson, M. A. Matthay, A. Frigeri, and A. S. Verkman, "Transepithelial water permeability in microperfused distal airways. Evidence for channel-mediated water transport." *The Journal of clinical investigation*, vol. 97, no. 3, pp. 664–71, feb 1996. [Online]. Available: http://www.ncbi.nlm.nih.gov/pubmed/8609221http://www.pubmedcentral.nih.gov/articlerender.fcgi?artid=PMC507102 21

[59] E. O. Potma and X. S. Xie, "CARS Microscopy for Biology and Medicine," *Optics and Photonics News*, vol. 15, no. 11, p. 40, nov 2004. [Online]. Available: https://www.osapublishing.org/abstract.cfm?URI=opn-15-11-40 23

[60] F. Fornasiero, F. Krull, J. M. Prausnitz, and C. J. Radke, "Steady-state diffusion of water through soft-contact-lens materials," *Biomaterials*, vol. 26, no. 28, pp. 5704–5716, oct 2005. [Online]. Available: https://www.sciencedirect.com/science/article/pii/S0142961205001948 24

[61] J. Maitra and V. Kumar Shukla, "Cross-linking in Hydrogels-A Review," *American Journal of Polymer Science*, vol. 2014, no. 2, pp. 25–31, 2014. [Online]. Available: http://journal.sapub.org/ajps 25

[62] J. Decock, M. Schlenk, and J.-B. Salmon, "In situ photopatterning of pressure-resistant hydrogel membranes with controlled permeabilities in PEGDA microfluidic channels," *Lab on a Chip*,

vol. 18, no. 7, pp. 1075–1083, mar 2018. [Online]. Available: http://xlink.rsc.org/?DOI=C7LC01342F 38, 120

[63] M. P. Cuchiara, A. C. Allen, T. M. Chen, J. S. Miller, and J. L. West, "Multilayer microfluidic PEGDA hydrogels," *Biomaterials*, vol. 31, no. 21, pp. 5491–5497, jul 2010. [Online]. Available: https://www.sciencedirect.com/science/article/pii/S014296121000387X 38

[64] H. L. Weissberg, "Effective Diffusion Coefficient in Porous Media," *Journal of Applied Physics*, vol. 34, no. 9, pp. 2636–2639, sep 1963. [Online]. Available: http://aip.scitation.org/doi/10.1063/1.1729783 43

[65] A. B. Mamonov, R. D. Coalson, M. L. Zeidel, and J. C. Mathai, "Water and deuterium oxide permeability through aquaporin 1: MD predictions and experimental verification." *The Journal of general physiology*, vol. 130, no. 1, pp. 111–6, jul 2007. [Online]. Available: http://www.ncbi.nlm.nih.gov/pubmed/17591989http://www.pubmedcentral.nih.gov/articlerender.fcgi?artid=PMC2154366 43, 44, 98

[66] M. E. Baur, C. W. Garland, and W. H. Stockmayer, "Diffusion coefficients of H2O-D2O Mixtures," *Journal of the American Chemical Society*, vol. 81, no. 12, pp. 3147–3148, jun 1959. [Online]. Available: http://pubs.acs.org/doi/abs/10.1021/ja01521a058 43, 44, 59

[67] G. Bottomley and R. Scott, "Excess volumes for H2O + D2O liquid mixtures," *Australian Journal of Chemistry*, vol. 29, no. 2, p. 427, 1976. [Online]. Available: http://www.publish.csiro.au/?paper=CH9760427 44

[68] S. Y. Yuan and R. R. Rigor, *Regulation of Endothelial Barrier Function*. Morgan & Claypool Life Sciences, 2010. [Online]. Available: http://www.ncbi.nlm.nih.gov/pubmed/21634066 64

[69] M. Félétou, *The Endothelium*. Morgan & Claypool Life Sciences, 2011. [Online]. Available: http://www.ncbi.nlm.nih.gov/pubmed/21850763 64, 65

[70] T. A. Duncombe, A. M. Tentori, and A. E. Herr, "Microfluidics: reframing biological enquiry," *Nature Reviews Molecular Cell Biology*, vol. 16, no. 9, pp. 554–567, sep 2015. [Online]. Available: http://www.nature.com/articles/nrm4041 66

[71] M. I. Bogorad, J. DeStefano, J. Karlsson, A. D. Wong, S. Gerecht, P. C. Searson, B. Engelhardt, P. Grammas, M. Nedergaard, J. Nutt, W. Pardridge, G. A. Rosenberg, Q. Smith, L. R. Drewes, P. Bowness, K. M. Boycott, C. Buser-Doepner, C. L. Carpenter, A. J. Carr, K. Clark, A. M. Das, D. Dhanak, P. Dirks, J. Ellis, V. R. Fantin, C. Flores, E. A. Fon, D. E. Frail, O. Gileadi, R. C. O'Hagan, T. Howe, J. T. R. Isaac, N. Jabado, P.-J. Jakobsson, L. Klareskog, S. Knapp, W. H. Lee, E. Lima-Fernandes, I. E. Lundberg, J. Marshall, K. B. Massirer, A. E. MacKenzie, T. Maruyama, A. Mueller-Fahrnow, S. Muthuswamy, J. Nanchahal, C. O'Brien, U. Oppermann, N. Ostermann, K. Petrecca, B. G. Pollock, V. Poupon, R. K. Prinjha, S. H. Rosenberg, G. Rouleau, M. Skingle, A. S. Slutsky, G. A. M. Smith, D. Verhelle, H. Widmer, and L. T. Young, "Review: in vitro microvessel models," *Lab Chip*, vol. 15, no. 22, pp. 4242–4255, 2015. [Online]. Available: http://xlink.rsc.org/?DOI=C5LC00832H 67, 68, 90

[72] V. van Duinen, S. J. Trietsch, J. Joore, P. Vulto, and T. Hankemeier, "Microfluidic 3D cell culture: from tools to tissue models," *Current Opinion in Biotechnology*, vol. 35, pp. 118–126, dec 2015. [Online]. Available: https://www.sciencedirect.com/science/article/pii/S0958166915000713 68, 71

[73] S. Chien, "Mechanotransduction and endothelial cell homeostasis: the wisdom of the cell," *American Journal of Physiology-Heart and Circulatory Physiology*, vol. 292, no. 3, pp. H1209–H1224, mar 2007. [Online]. Available: http://www.physiology.org/doi/10.1152/ajpheart.01047.2006 68

[74] Q. Smith and S. Gerecht, "Going with the flow: microfluidic platforms in vascular tissue engineering," *Current Opinion in Chemical*

Engineering, vol. 3, pp. 42–50, feb 2014. [Online]. Available: https://www.sciencedirect.com/science/article/pii/S2211339813001123 68, 69

[75] T. Annussek, T. Szuwart, J. Kleinheinz, C. Koiky, and K. Wermker, "In vitro inhibition of HUVECs by low dose methotrexate - insights into oral adverse events." *Head & face medicine*, vol. 10, p. 19, may 2014. [Online]. Available: http://www.ncbi.nlm.nih.gov/pubmed/24884884http://www.pubmedcentral.nih.gov/articlerender.fcgi?artid=PMC4033494 69

[76] J. C. Pelton, C. E. Wright, M. Leitges, and V. L. Bautch, "Multiple endothelial cells constitute the tip of developing blood vessels and polarize to promote lumen formation." *Development*, vol. 141, no. 21, pp. 4121–6, nov 2014. [Online]. Available: http://www.ncbi.nlm.nih.gov/pubmed/25336741http://www.pubmedcentral.nih.gov/articlerender.fcgi?artid=PMC4302885 69, 70

[77] I. K. Zervantonakis, S. K. Hughes-Alford, J. L. Charest, J. S. Condeelis, F. B. Gertler, and R. D. Kamm, "Three-dimensional microfluidic model for tumor cell intravasation and endothelial barrier function." *Proceedings of the National Academy of Sciences of the United States of America*, vol. 109, no. 34, pp. 13 515–20, aug 2012. [Online]. Available: http://www.ncbi.nlm.nih.gov/pubmed/22869695http://www.pubmedcentral.nih.gov/articlerender.fcgi?artid=PMC3427099 69

[78] J. N. Lee, X. Jiang, D. Ryan, and G. M. Whitesides, "Compatibility of mammalian cells on surfaces of poly(dimethylsiloxane)." *Langmuir : the ACS journal of surfaces and colloids*, vol. 20, no. 26, pp. 11 684–91, dec 2004. [Online]. Available: http://www.ncbi.nlm.nih.gov/pubmed/15595798 69

[79] A. Piruska, I. Nikcevic, S. H. Lee, C. Ahn, W. R. Heineman, P. A. Limbach, and C. J. Seliskar, "The autofluorescence of plastic materials and chips measured under laser irradiation," *Lab on a Chip*, vol. 5,

no. 12, p. 1348, dec 2005. [Online]. Available: http://www.ncbi.nlm.nih.gov/pubmed/16286964http://xlink.rsc.org/?DOI=b508288a 69

[80] T. Fujii, "PDMS-based microfluidic devices for biomedical applications," *Microelectronic Engineering*, vol. 61-62, pp. 907–914, jul 2002. [Online]. Available: https://www.sciencedirect.com/science/article/pii/S016793170200494X 69

[81] Y. S. Heo, L. M. Cabrera, J. W. Song, N. Futai, Y.-C. Tung, G. D. Smith, and S. Takayama, "Characterization and resolution of evaporation-mediated osmolality shifts that constrain microfluidic cell culture in poly(dimethylsiloxane) devices." *Analytical chemistry*, vol. 79, no. 3, pp. 1126–34, feb 2007. [Online]. Available: http://www.ncbi.nlm.nih.gov/pubmed/17263345http://www.pubmedcentral.nih.gov/articlerender.fcgi?artid=PMC2605290 69

[82] C. O. Lizama and A. C. Zovein, "Polarizing pathways: balancing endothelial polarity, permeability, and lumen formation." *Experimental cell research*, vol. 319, no. 9, pp. 1247–54, may 2013. [Online]. Available: http://www.ncbi.nlm.nih.gov/pubmed/23567183http://www.pubmedcentral.nih.gov/articlerender.fcgi?artid=PMC3686563 70

[83] S. H. Tan, N.-T. Nguyen, Y. C. Chua, and T. G. Kang, "Oxygen plasma treatment for reducing hydrophobicity of a sealed polydimethylsiloxane microchannel." *Biomicrofluidics*, vol. 4, no. 3, p. 32204, sep 2010. [Online]. Available: http://www.ncbi.nlm.nih.gov/pubmed/21045926http://www.pubmedcentral.nih.gov/articlerender.fcgi?artid=PMC2967237 70

[84] B. Poller, H. Gutmann, S. Krähenbühl, B. Weksler, I. Romero, P.-O. Couraud, G. Tuffin, J. Drewe, and J. Huwyler, "The human brain endothelial cell line hCMEC/D3 as a human blood-brain barrier model for drug transport studies." *Journal of neurochemistry*, vol. 107, no. 5, pp. 1358–68, dec 2008. [Online]. Available: http://www.ncbi.nlm.nih.gov/pubmed/19013850 72

[85] N.-D. Dinh, Y.-Y. Chiang, H. Hardelauf, S. Waide, D. Janasek, and J. West, "Preparation of Neuronal Co-cultures with Single Cell Precision," *Journal of Visualized Experiments*, no. 87, pp. e51 389–e51 389, may 2014. [Online]. Available: http://www.jove.com/video/51389/preparation-of-neuronal-co-cultures-with-single-cell-precision 74

[86] K. J. Regehr, M. Domenech, J. T. Koepsel, K. C. Carver, S. J. Ellison-Zelski, W. L. Murphy, L. A. Schuler, E. T. Alarid, and D. J. Beebe, "Biological implications of polydimethylsiloxane-based microfluidic cell culture." *Lab on a Chip*, vol. 9, no. 15, pp. 2132–9, aug 2009. [Online]. Available: http://www.ncbi.nlm.nih.gov/pubmed/19606288http://www.pubmedcentral.nih.gov/articlerender.fcgi?artid=PMC2792742 79, 80

[87] L. J. Millet, M. E. Stewart, J. V. Sweedler, R. G. Nuzzo, and M. U. Gillette, "Microfluidic devices for culturing primary mammalian neurons at low densities," *Lab on a Chip*, vol. 7, no. 8, p. 987, jul 2007. [Online]. Available: http://xlink.rsc.org/?DOI=b705266a 80

[88] Dow Corning Corporation, "Dow Corning ® Silicone Sealants and Foams for Industrial Assembly and Maintenance Selection Guide." [Online]. Available: https://www.mavom.nl/fileadmin/user_upload/Dow-Corning-Silicone-sealants-foams-IAM.pdf 81

[89] B. Riegler, R. Thomaier, and H. Sarria, "Fast-Cure Silicone Adhesives for Medical Devices," *Medical Device and Diagnostic Industry*, 2004. [Online]. Available: https://www.mddionline.com/fast-cure-silicone-adhesives-medical-devices 82

[90] E. W. K. Young and D. J. Beebe, "Fundamentals of microfluidic cell culture in controlled microenvironments." *Chemical Society Reviews*, vol. 39, no. 3, pp. 1036–48, mar 2010. [Online]. Available: http://www.ncbi.nlm.nih.gov/pubmed/20179823http://www.pubmedcentral.nih.gov/articlerender.fcgi?artid=PMC2967183 86

[91] Thermofisher Scientific, "Cell Culture Basics Handbook," 2015. [Online]. Available: https://www.thermofisher.com/content/dam/LifeTech/global/promotions/global/images/aai-2015/aai-pdfs/GibcoCellCultureBasicsHandbook.pdf 87

[92] L. Wolpert, "Cell polarity." *Philosophical transactions of the Royal Society of London. Series B, Biological sciences*, vol. 368, no. 1629, p. 20130419, 2013. [Online]. Available: http://www.ncbi.nlm.nih.gov/pubmed/24062591http://www.pubmedcentral.nih.gov/articlerender.fcgi?artid=PMC3785971 88

[93] M. G. Lampugnani, F. Orsenigo, N. Rudini, L. Maddaluno, G. Boulday, F. Chapon, and E. Dejana, "CCM1 regulates vascular-lumen organization by inducing endothelial polarity," *Journal of Cell Science*, vol. 123, no. 7, 2010. [Online]. Available: http://jcs.biologists.org/content/123/7/1073.long{#}sec-6 88, 89

[94] J. E. Testa, A. Chrastina, Y. Li, P. Oh, and J. E. Schnitzer, "Ubiquitous yet distinct expression of podocalyxin on vascular surfaces in normal and tumor tissues in the rat." *Journal of vascular research*, vol. 46, no. 4, pp. 311–24, 2009. [Online]. Available: http://www.ncbi.nlm.nih.gov/pubmed/19142011http://www.pubmedcentral.nih.gov/articlerender.fcgi?artid=PMC2798848 89

[95] Y.-M. Kook, H. Kim, S. Kim, C. Y. Heo, M. H. Park, K. Lee, and W.-G. Koh, "Promotion of Vascular Morphogenesis of Endothelial Cells Co-Cultured with Human Adipose-Derived Mesenchymal Stem Cells Using Polycaprolactone/Gelatin Nanofibrous Scaffolds." *Nanomaterials (Basel, Switzerland)*, vol. 8, no. 2, feb 2018. [Online]. Available: http://www.ncbi.nlm.nih.gov/pubmed/29463042http://www.pubmedcentral.nih.gov/articlerender.fcgi?artid=PMC5853748 89

[96] T. Nguyen, J. Toussaint, Y. Xue, C. Raval, L. Cancel, S. Russell, Y. Shou, O. Sedes, Y. Sun, R. Yakobov, J. M. Tarbell, K.-m. Jan, and D. S. Rumschitzki, "Aquaporin-1 facilitates pressure-driven water flow across the aortic endothelium." *American journal of physiology. Heart*

and circulatory physiology, vol. 308, no. 9, pp. H1051–64, may 2015. [Online]. Available: http://www.ncbi.nlm.nih.gov/pubmed/25659484http://www.pubmedcentral.nih.gov/articlerender.fcgi?artid=PMC4551120 92

[97] P. Wintmo, S. H. Johansen, P. B. L. Hansen, J. S. Lindholt, S. Urbonavicius, L. M. Rasmussen, P. Bie, B. L. Jensen, and J. Stubbe, "The water channel AQP1 is expressed in human atherosclerotic vascular lesions and AQP1 deficiency augments angiotensin II-induced atherosclerosis in mice," *Acta Physiologica*, vol. 220, no. 4, pp. 446–460, jan 2017. [Online]. Available: http://www.ncbi.nlm.nih.gov/pubmed/28129470http://doi.wiley.com/10.1111/apha.12853 93

[98] T. Ma, B. Yang, A. Gillespie, E. J. Carlson, C. J. Epstein, and A. S. Verkman, "Severely impaired urinary concentrating ability in transgenic mice lacking aquaporin-1 water channels." *The Journal of biological chemistry*, vol. 273, no. 8, pp. 4296–9, feb 1998. [Online]. Available: http://www.ncbi.nlm.nih.gov/pubmed/9468475 93, 101, 102, 128, 129

[99] Y. Horibe and M. Kobayakawa, "Deuterium abundance of natural waters," *Geochimica et Cosmochimica Acta*, vol. 20, no. 3-4, pp. 273–283, nov 1960. [Online]. Available: https://www.sciencedirect.com/science/article/pii/0016703760900788 95

[100] J. S. Murday and R. M. Cotts, "Self-Diffusion in Liquids: H2O, D2O, and Na," *The Journal of Chemical Physics*, vol. 53, no. 12, pp. 4724–4725, dec 1970. [Online]. Available: http://aip.scitation.org/doi/10.1063/1.1674011 98

[101] N. Agmon, "The Grotthuss mechanism," *Chemical Physics Letters*, vol. 244, no. 5, pp. 456–462, 1995. 99

[102] E. L. Cussler, *Diffusion*, 3rd ed. Cambridge University Press, 2009. 99

[103] A. Hassanali, F. Giberti, J. Cuny, T. D. Kühne, M. Parrinello, and M. L. Klein, "Proton transfer through the water gossamer," *Proceedings of the National Academy of Sciences*, vol. 110, no. 34, pp. 13 723–13 728, aug

2013. [Online]. Available: http://www.pnas.org/lookup/doi/10.1073/pnas.1306642110 99

[104] J. H. Wang, C. V. Robinson, and I. S. Edelman, "Self-diffusion and Structure of Liquid Water. III. Measurement of the Self-diffusion of Liquid Water with H ² , H ³ and O ¹⁸ as Tracers ¹," *Journal of the American Chemical Society*, vol. 75, no. 2, pp. 466–470, jan 1953. [Online]. Available: http://pubs.acs.org/doi/abs/10.1021/ja01098a061 100

[105] A. Madeira, T. F. Moura, and G. Soveral, "Detecting Aquaporin Function and Regulation." *Frontiers in chemistry*, vol. 4, p. 3, 2016. [Online]. Available: http://www.ncbi.nlm.nih.gov/pubmed/26870725http://www.pubmedcentral.nih.gov/articlerender.fcgi?artid=PMC4734071 100

[106] B. Kirchner, "Eigen or Zundel Ion: News from Calculated and Experimental Photoelectron Spectroscopy," *ChemPhysChem*, vol. 8, no. 1, pp. 41–43, jan 2007. [Online]. Available: http://doi.wiley.com/10.1002/cphc.200600476 100

[107] W. Junge and S. Mclaughlin, "The role of fixed and mobile buffers in the kinetics of proton movement," *Biochimica et Biophysica Acta*, vol. 890, pp. 1–5, 1987. 100

[108] A. Dobin, C. A. Davis, F. Schlesinger, J. Drenkow, C. Zaleski, S. Jha, P. Batut, M. Chaisson, and T. R. Gingeras, "STAR: ultrafast universal RNA-seq aligner." *Bioinformatics (Oxford, England)*, vol. 29, no. 1, pp. 15–21, jan 2013. [Online]. Available: http://www.ncbi.nlm.nih.gov/pubmed/23104886http://www.pubmedcentral.nih.gov/articlerender.fcgi?artid=PMC3530905 103, 132

[109] A. Volkmer, "Vibrational imaging and microspectroscopies based on coherent anti-Stokes Raman scattering," *Journal of Physics D: Applied Physics*, vol. 38, no. 5, pp. R59–R81, mar 2005. [Online]. Available: http://iopscience.iop.org/article/10.1088/0022-3727/38/5/

R01/pdfhttp://stacks.iop.org/0022-3727/38/i=5/a=R01?key=crossref.46b0de6310782f37f2c28a85f8cae1d4 125

[110] S. Kedenburg, M. Vieweg, T. Gissibl, and H. Giessen, "Linear refractive index and absorption measurements of nonlinear optical liquids in the visible and near-infrared spectral region," *Optical Materials Express*, vol. 2, no. 11, p. 1588, nov 2012. [Online]. Available: https://www.osapublishing.org/abstract.cfm?URI=ome-2-11-1588 125

[111] M. J. Booth and T. Wilson, "Strategies for the compensation of specimen-induced spherical aberration in confocal microscopy of skin," *Journal of Microscopy*, vol. 200, no. 1, pp. 68–74, oct 2000. [Online]. Available: http://doi.wiley.com/10.1046/j.1365-2818.2000.00735.x 125

[112] G. Fairbanks, T. L. Steck, and D. F. Wallach, "Electrophoretic analysis of the major polypeptides of the human erythrocyte membrane." *Biochemistry*, vol. 10, no. 13, pp. 2606–17, jun 1971. [Online]. Available: http://www.ncbi.nlm.nih.gov/pubmed/4326772 130

[113] J. Terris, C. A. Ecelbarger, S. Nielsen, and M. A. Knepper, "Long-term regulation of four renal aquaporins in rats." *The American journal of physiology*, vol. 271, no. 2 Pt 2, pp. F414–22, aug 1996. [Online]. Available: http://www.physiology.org/doi/10.1152/ajprenal.1996.271.2.F414http://www.ncbi.nlm.nih.gov/pubmed/8770174 131

[114] J. D. Hoffert, R. A. Fenton, H. B. Moeller, B. Simons, D. Tchapyjnikov, B. W. McDill, M.-J. Yu, T. Pisitkun, F. Chen, and M. A. Knepper, "Vasopressin-stimulated increase in phosphorylation at Ser269 potentiates plasma membrane retention of aquaporin-2." *The Journal of biological chemistry*, vol. 283, no. 36, pp. 24 617–27, sep 2008. [Online]. Available: http://www.ncbi.nlm.nih.gov/pubmed/18606813http://www.pubmedcentral.nih.gov/articlerender.fcgi?artid=PMC2528999 131

[115] C. A. Ecelbarger, J. Terris, G. Frindt, M. Echevarria, D. Marples, S. Nielsen, and M. A. Knepper, "Aquaporin-3 water channel localization and regulation in rat kidney." *The American journal of*

physiology, vol. 269, no. 5 Pt 2, pp. F663–72, nov 1995. [Online]. Available: http://www.physiology.org/doi/10.1152/ajprenal.1995.269.5.F663http://www.ncbi.nlm.nih.gov/pubmed/7503232 131

[116] J. Terris, C. A. Ecelbarger, D. Marples, M. A. Knepper, and S. Nielsen, "Distribution of aquaporin-4 water channel expression within rat kidney." *The American journal of physiology*, vol. 269, no. 6 Pt 2, pp. F775–85, dec 1995. [Online]. Available: http://www.physiology.org/doi/10.1152/ajprenal.1995.269.6.F775http://www.ncbi.nlm.nih.gov/pubmed/8594871 131

[117] L. Chen, J. W. Lee, C.-L. Chou, A. V. Nair, M. A. Battistone, T. G. Păunescu, M. Merkulova, S. Breton, J. W. Verlander, S. M. Wall, D. Brown, M. B. Burg, and M. A. Knepper, "Transcriptomes of major renal collecting duct cell types in mouse identified by single-cell RNA-seq." *Proceedings of the National Academy of Sciences of the United States of America*, vol. 114, no. 46, pp. E9989–E9998, nov 2017. [Online]. Available: http://www.ncbi.nlm.nih.gov/pubmed/29089413http://www.pubmedcentral.nih.gov/articlerender.fcgi?artid=PMC5699061 132

[118] B. Li and C. N. Dewey, "RSEM: accurate transcript quantification from RNA-Seq data with or without a reference genome," *BMC Bioinformatics*, vol. 12, no. 1, p. 323, aug 2011. [Online]. Available: http://bmcbioinformatics.biomedcentral.com/articles/10.1186/1471-2105-12-323 133

[119] P. K. Glasoe and F. A. Long, "Use of Glass Electrodes to Measure Acidities in Deuterium Oxide," *The Journal of Physical Chemistry*, vol. 64, no. 1, pp. 188–190, jan 1960. [Online]. Available: http://pubs.acs.org/doi/abs/10.1021/j100830a521 133

[120] A. Tedgui and M. J. Lever, "Filtration through damaged and undamaged rabbit thoracic aorta." *The American journal of physiology*, vol. 247, no. 5 Pt 2, pp. H784–91, nov 1984. [Online]. Available: http://www.ncbi.nlm.nih.gov/pubmed/6496759 133